Fabrication and characterization of CPP-GMR and spin-transfer torque induced magnetic switching

Dissertation

zur Erlangung des
naturwissenschaftlichen Doktorgrades
der Julius-Maximilians-Universität Würzburg

vorgelegt von
Marjan Samiepour
aus Neyshaboor, Iran

Würzburg 2014

Eingereicht am: ...

bei der Fakultät für Physik und Astronomie

1. Gutachter: PD Dr. Charles Gould

2. Gutachter: Prof. Dr. Peter Jakob

3. Gutachter: .....

der Dissertation

Vorsitzende(r).....

1. Prüfer: PD Dr. Charles Gould

2. Prüfer: Prof. Dr. Peter Jakob

3. Prüfer: Prof. Dr. Ronny Thomale

im Promotionkolloquiums

Tag des Promotionskolloquiums: ...

Doktorurkunde ausgehändigt am: ...

Contents

Zusammenfassung

Obwohl das einzigartige ferromagnetische Verhalten seit Tausenden Jahren bekannt ist, traten Erklärungen zu diesem interessanten Phänomen erst im 20. Jahrhundert auf. Erst im Jahr 1920, mit der Entdeckung des Elekronenspin, gab es eine Vorstellung davon, wie die Ferromagnetika ihre einzigartigen magnetischen Eigenschaften erhalten. Die Elektronen sind sowohl Träger einer intrinsischen Ladung als auch eines intrinsichen Drehimpulses. Die Nutzung dieser Eigenschaften in Bauteilen wurde 1998 erreicht, als Fert und Grünberg unabhängig voneinander die Entdeckung machten, dass der Widerstand eines Dreischichtsystems bestehend aus FM/NM/FM abhängig vom Winkel der Magnetisierung in den zwei ferromagnetischen Schichten ist. Dieses Phänomen, welches als Riesenmagnetwiderstand (GMR, Giant Magnetoresistance) bekannt ist, führte dazu, dass sich der Spintransport zu einem Mainstream entwickelte. Diese neuartige Entdeckung brachte ein ganz neues Forschungsgebiet hervor, das als sogenannte Spintronik oder auch spinbasierte Elektronik bekannt ist, welche den intrinsischen Spin der Elektronen nutzt.

Wie erwartet lieferte die Spintronik eine neue Generation von magnetischen Bauelementen, welche in Festplatten und magnetoresistiven RAM-Speichern (MRAM, magnetic random access memory) zu finden sind. Die großen Vorteile der spintronischen Bauelemente sind die Nichtvolalität, die höheren Geschwindigkeiten, die verbesserte Datendichte und der geringerer Energieverbrauch. GMR-Bauteile werden bereits in der Industrie als magnetische Speicher und Leseköpfe verwendet.

Die Qualität der GMR-Bauteile kann durch die Entwicklung von neuen magnetischen Materialien aber auch durch Verkleinerung, also Nutzung der Nanoskala verbessert werden. Zu den gewünschten charakteristischen Eigenschaften dieser neuen Materialien zählen eine höhere Spinpolarisation, höher erreichbare Curie-Temperaturen und eine verbesserte Spinfiltration. Halbmetalle, wie z.B., Heusler-Legierungen, Perovskite oder auch doppeloxide sind hierfür gute Kandidaten, weil von ihnen eine hohe Polarisierbarkeit erwartet wird. Die Bauteile, die in dieser Arbeit diskutiert werden, bestehen aus einer NiMnSb-Heusler-Legierung und Permalloy als ferromagnetische Schichten getrennt durch Cu als nichtmagnetische Schicht.

Die Dissertation beinhaltet hauptsächlich zwei Aspekte nämlich die Herstellung und Charakterisierung von Nanosäulen. Die benutzte Schichtung zur Herstellung ist Ru/Py/Cu /NiMnSb, welche mittels MBE (molecular beam epitaxy) auf einem InP-Substrat mit

einem (In,Ga)As-Puffer gewachsen ist. Eine neue Herstellungsmethode, welche Metallmasken gegenüber der früher in unserer Arbeitsgruppe gängigen Methode (Verwendung von Resistmasken) nutzt, um eine erhöhte Probenfunktionalität zu erreichen, wird im Detail diskutiert. Ebenso werden die Vorteile dieser neuen Methode und das Detail der alten Methode vollständig in Kapitel 3 erläutert.

Im Fokus des zweiten Teils (Kapitel 4 und 5) stehen elektrische Messungen und Charakterisierung der Nanosäulen im Hinblick auf den GMR und den Spintransfer-Moment-Messungen (SST). In Kapitel 4 werden die Ergebnisse der Strommessungen, die senkrecht zur GMR-Ebene (CPP-GMR) bei verschiedenen Temperaturen und eines in der Ebene angelegten Magnetfeldes durchgeführt wurden vorgestellt zudem wird die Abhängigkeit des CPP-GMR von Bias-Strömen und von der Formanisotropy der Bauteile untersucht. Ergebnisse dieser Messungen zeigen, dass die Bauteile eine groe Formanisotropy aufweisen.

In den darauffolgenden Kapiteln werden Spintransfer-Moment Messungen, die durch magnetisches Schalten in den Bauteilen hervorgerufen wurden besprochen. Kritische Stromdichten liegen in der Größenordnung 10^6 A/cm^2, welche eine Größenordnung kleiner ist als der aktuelle Industriestandard. Unsere Ergebnisse zeigen eine starke Abhängigkeit der zwei magnetischen Konfigurationsmöglichkeiten der Nanosäulen (parallel und anti-parallel) von dem in-plane Magnetfeld. Schließlich wurden vier magnetische Feldbereiche, basierend auf der Stabilität der magnetischen Konfiguration (P stabil, AP stabil, P und AP stabil, P und AP instabil) identifiziert.

Summary

Even though the unique magnetic behavior for ferromagnets has been known for thousands of years, explaining this interesting phenomenon only occurred in the 20^{th} century. It was in 1920, with the discovery of electron spin, that a clear explanation of how ferromagnets achieve their unique magnetic properties came to light. The electron carries an intrinsic electric charge and intrinsic angular momentum. Use of this property in a device was achieved in 1998 when Fert and Grünberg independently found that the resistance of FM/NM/FM trilayer depended on the angle between the magnetization of the two layers. This phenomena which is called giant magnetoresistance (GMR) brought spin transfer into mainstream. This new discovery created a brand new research field called "spintronics" or "spin based electronics" which exploits the intrinsic spin of electron.

As expected spintronics delivered a new generation of magnetic devices which are currently used in magnetic disk drives and magnetic random access memories (MRAM). The potential advantages of spintronics devices are non-volatility, higher speed, increased data density and low power consumption. GMR devices are already used in industry as magnetic memories and read heads.

The quality of GMR devices can be increased by developing new magnetic materials and also by going down to nanoscale. The desired characteristic properties of these new materials are higher spin polarization, higher curie temperature and better spin filtering. Half-metals are a good candidate for these devices since they are expected to have high polarization. Some examples of half-metals are Half-Heusler alloy, full Heusler alloy and Perovskite or double Perovskite oxides. The devices discussed in this thesis have NiMnSb half-Heusler alloy and permalloy as the ferromagnetic layers separated by Cu as the nonmagnetic layer.

This dissertation includes mainly two parts, fabrication and characterization of nanopillars. The layer stack used for the fabrication is Ru/Py/Cu/NiMnSb which is grown on an InP substrate with an (In,Ga)As buffer by molecule beam epitaxy (MBE). A new method of fabrication using metal mask which has a higher yield of working samples over the previous method (using the resist mask) used in our group is discussed in detail. Also, the advantages of this new method and draw backs of the old method are explained thoroughly (in chapter 3).

The second part (chapters 4 and 5) is focused on electrical measurements and characterization of the nanopillar, specially with regard to GMR and spin-transfer torque (STT)

measurements. In chapter 4, the results of current perpendicular the plane giant magnetoresistance (CPP-GMR) measurements at various temperatures and in-plane magnetic fields are presented. The dependence of CPP-GMR on bias current and shape anisotropy of the device are investigated. Results of these measurements show that the device has strong shape anisotropy.

The following chapter deals with spin-transfer torque induced magnetic switching measurements done on the device. Critical current densities are on the order of 10^6 A/cm^2, which is one order of magnitude smaller than the current industry standards. Our results show that the two possible magnetic configurations of the nanopillar (parallel and anti-parallel) have a strong dependence on the applied in-plane magnetic field. Finally, four magnetic field regimes based on the stability of the magnetic configuration (P stable, AP stable, both P and AP stable, both P and AP unstable) are identified.

Chapter 1

Motivation

1.1 Introduction

From 2012 until 2020, the world's digital information will double in every two years [John 13]. In 2007, the amount of digital information reached 2.8×10^{20} Bytes and in 2011 the digital information created and replicated surpassed 1.8 zettabytes. Corresponding to the growth of digital information, the power consumption for the data storage has become a very important issue. For example, electricity used in global data centers in 2010 alone is accounted for between 1.1% and 1.5% of total electricity use [Koom 08]. Recently, using the new technologies in data storage devices have generated the most intense interest, because of the importance of these new devices in decrease of the power consumption for data storage. Furthermore, the new generation of magnetic memories are operating with higher speed which nowadays is a social demand.

Nonvolatile memories that can store data even when not powered are currently used for portable electronics such as magnetic memories and flash memories. Although huge amount of digital information can be stored in hard disk drive (HDD), by growing the recording density of HDD, the energy consumption for data storage will increase exponentially. Therefore, the development of magnetic recording technology in order to make the new data storage with lower energy consumption is a significant demand.

The field of spintronics has acquired significant interest in the research community over time since it is capable of delivering new devices with higher magnetic recording density and low power consumption. New technologies like spin-transfer torque magnetic random access memory (STT-MRAM) and voltage controlled oscillators (VCO) have emerged from spintronics. The new HDDs on the market have already incorporated novel phenomena such as current perpendicular to plane giant magnetoresistance (CPP-GMR) and spin-transfer torque to perform better than their previous generation. Currently the study of the MR output and current density are essential for improving the magnetic devices. This doctoral thesis describes our study of half-Heusler based CPP-GMR and spin-transfer-torque-induced-switching devices.

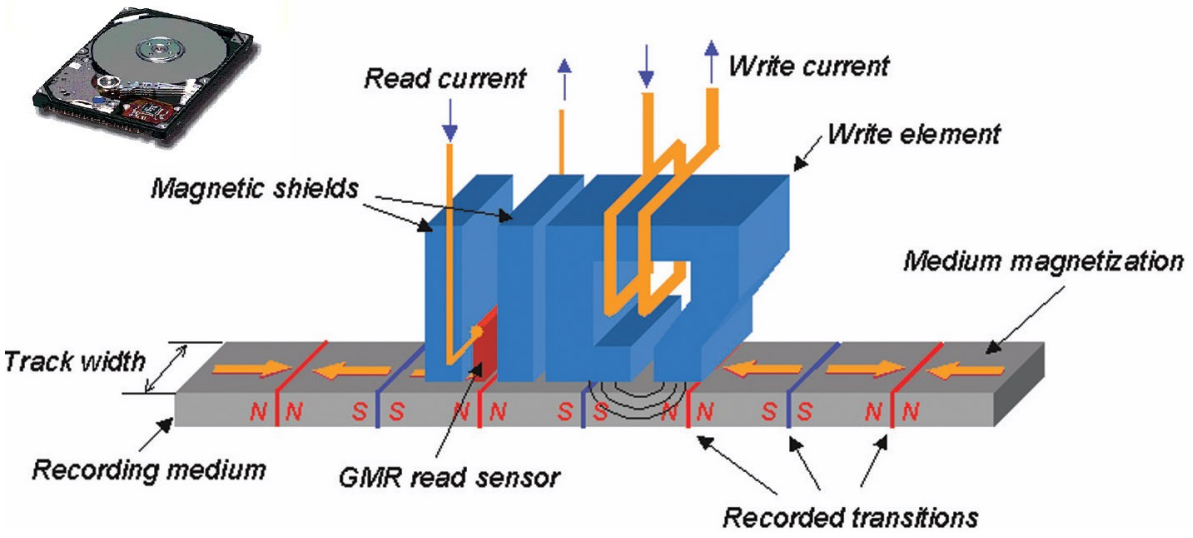

Figure 1.1: Schematic diagram of Read/Write magnetic recording device present in hard disks. Reprinted from [Zhu 03]

1.2 Applications

1.2.1 Magnetic hard dick drive (HHD)

The independent discovery of GMR by Albert Fert and Peter Grünberg (Nobel prize in physics 2007) is described as one of first real application of nanotechnology. The most important technological application of GMR is in data storage industry. The first hard disk drive based on GMR technology was introduced to the market by IBM in 1997. GMR devices not only dramatically increased the density of stored information on disk drives, but also allowed the creation of smaller drives which could store reasonable amounts of information and consume less power [Dien 91].

A traditional GMR sensor in a magnetic hard disk drive (HHDs) is composed of an inductive write element and a giant magnetoresistive read element [Dien 91, Some 76]. As figure 1.1 shows, binary data are stored in a recording medium which is a thin magnetic layer containing large number of small cells whose local magnetic moment can be controlled separately. This binary data (‘1’ and ‘0’) are represented on the magnetic layer by the direction of the local magnetic moment. A ‘1’ bit is stored, when the direction of the local magnetic moment is reversed along the circumferentially arranged data track. And a ‘0’ bit is presented by no change in the local magnetization orientation of the recording medium. The reason why stored data maintain the orientation of the local magnetic moment is because of the magnetic hysteresis of the recording media. The disk rotates while the read head and write element are embedded at the end of a slider. The write element produces a magnetic field in the head gap with an inductive magnetic transducer. In the

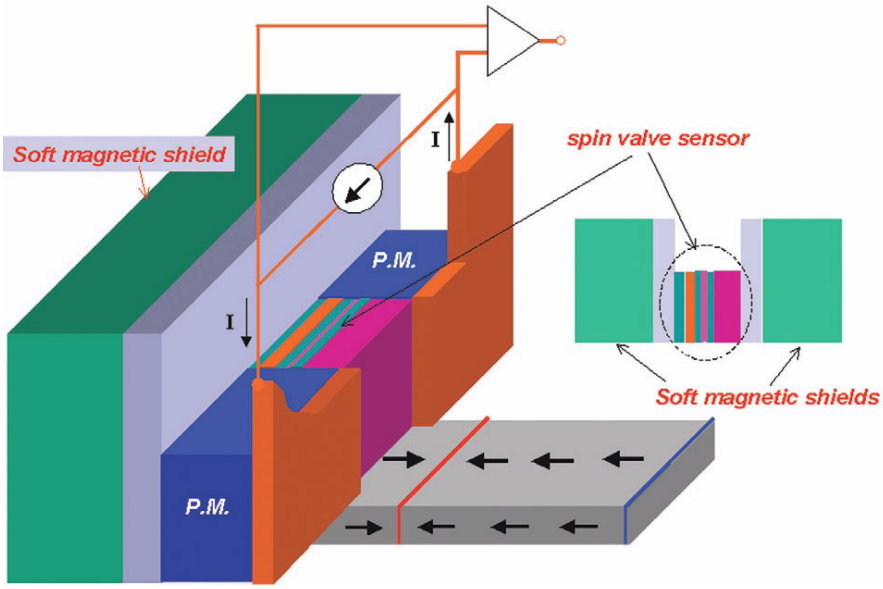

Figure 1.2: Schematic picture of a spin valve head structure which is used in HDDs. A spin valve read sensor stack is placed in between a pair of permanent magnets that provide a horizontal magnetic field in the cross-track direction. Two soft magnetic shields are placed in the down track direction, enabling adequate spatial resolution for high linear recording density. Reprinted from [Zhu 03].

writing process the amplitude of the writing current is kept constant but the direction is reversed every time a bit is stored. A simple exchange bias spin valve GMR read sensor is shown in figure 1.2. The pinned layer in GMR is perpendicular to slider surface. The magnetization of the other ferromagnetic layer is free to respond to the magnetic field flux from recorded transitions in the medium. The resistivity of the GMR read sensor changes as the magnetization angle (θ) between the free and pinned layer changes [Zhu 03].

$$\rho = \rho_0 + \Delta\rho.\frac{1}{2}\cos\theta = \rho_0(1 + \frac{\Delta\rho}{\rho_0}.\frac{1}{2}\cos\theta) \tag{1.1}$$

Where $\Delta\rho/\rho_0$ is the GMR ratio. Higher GMR ratio increases the density of information stored in disk drives. Using materials with high polarization factor at room temperature increases the GMR ratio. Half-Heusler alloys are good candidates for this purpose (chapter 2.6).

1.2.2 STT-MRAM and MRAM

A new generation of the magnetic memories are the spin-transfer torque magnetic random access memories (STT-MRAM). A similar method which is used for reading in HDD is also used in STT-MRAM [Apal 13, Tehr 03]. In 2006, Freescale used MRAM in critical aircraft

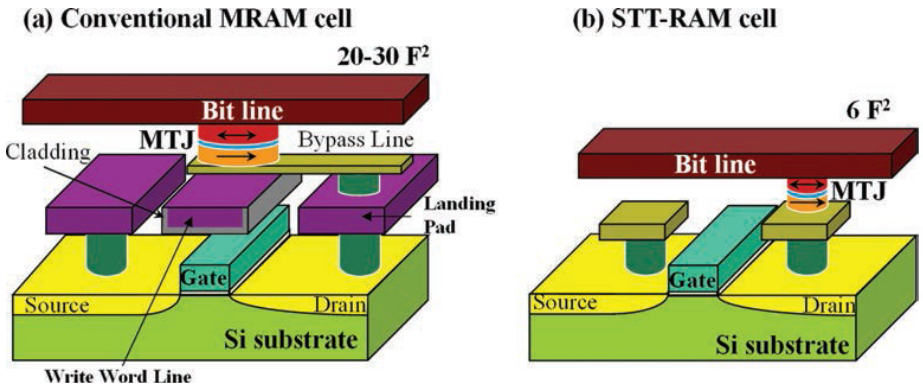

Figure 1.3: Schematic structure of conventional field-switched MRAM cell (a) as compared to spin-transfer torque MRAM cell(STT-MRAM)(b). Reprinted from [Apal 13]

and automotive applications. As figure 1.3 shows, there are some differences between STT-MRAM and MRAM. The first difference is in the recording data. In MRAM, the external magnetic field which is used to switch between two memory states is generated by a current flow through the word and bit lines (figure 1.3). Even though MRAM has many advantages like non-volatility, relatively fast and high density, it is expected to have some serious limitation in the future. One of them is the scale of MRAM. When the size of the MRAM cell decreases the magnetic field required for switching increases, which in turn increases the required current. Therefore the power consumption increases by decreasing the scale of the MRAM cell. On the other side, in STT-MRAM switching current reduces by increasing the scale of devices. Figure 1.4 shows write current versus magnetic cell width for MRAM and STT-MRAM.

The other important limitation of MRAM is called 'half-select' (or write disturb). As figure 1.5 shows the switching of the cell occurs when current is passed through the bit line (above the storage cell) and word line (below cell). Due to the difficulty in confining the localized magnetic field, neighboring bits can be accidentally switched. Furthermore, this crosstalk problem becomes worse when the bit density increases by bringing the bits closer [Rose 08].

Finally, the design of the STT-MRAM cells (figure 1.3) are simpler than the MRAM cells. The smallest size of a STT-MRAM cell is 6 F^2 (minimum 1 F gate width transistor can drive 6 F^2 cell beyond 45 nm) for in-plane design and 4 F^2 for perpendicular design and smaller than 4 F^2 for multiple-level cell (MLC) design, for which there are two or more storage elements per single nanopillar [Apal 13]. So most probably the STT-MRAM technology will be the future memory, a dens (around 10 F^2), fast (below 10 ns read and write speeds) memory with low power consumption.

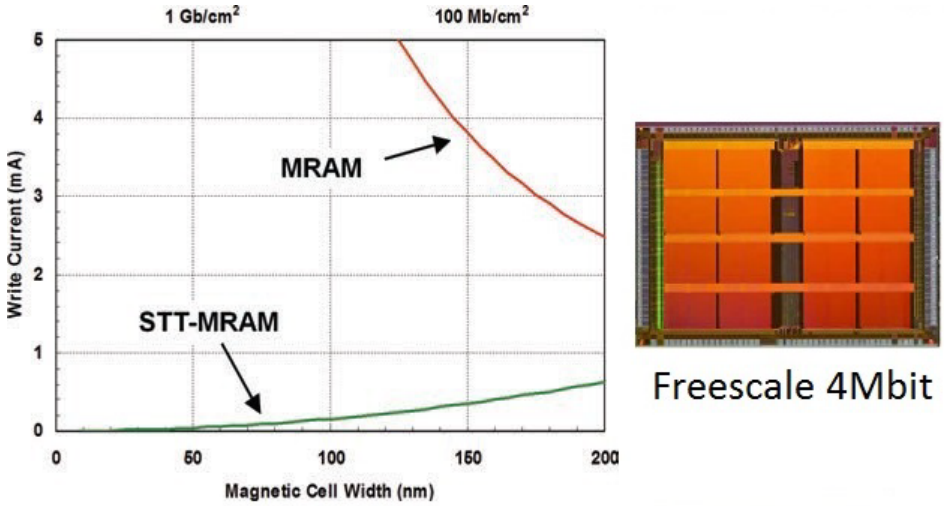

Figure 1.4: The write current as a function of magnetic cell width for field and current switching under the assumption of constant thermal stability factor equal to 55. Reprinted from [Apal 13].

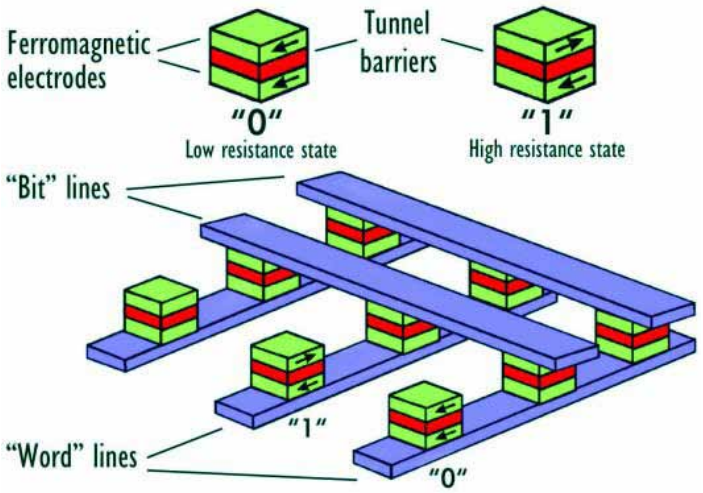

Figure 1.5: Schematic picture of MRAM. In magnetic tunnel junctions (MTJs) the binary information 0 and 1 is recorded on the two opposite orientations of the magnetization. The current pulses pass through 'word' lines and only at the crossing point of these lines the magnetic field is high enough to orient the magnetization of the free layer. For reading, the resistance of the MTJ is measured. If the bits are brought too close the magnetic field overlaps with neighbor cells and can cause potential false writes. Reprinted from [Chap 07].

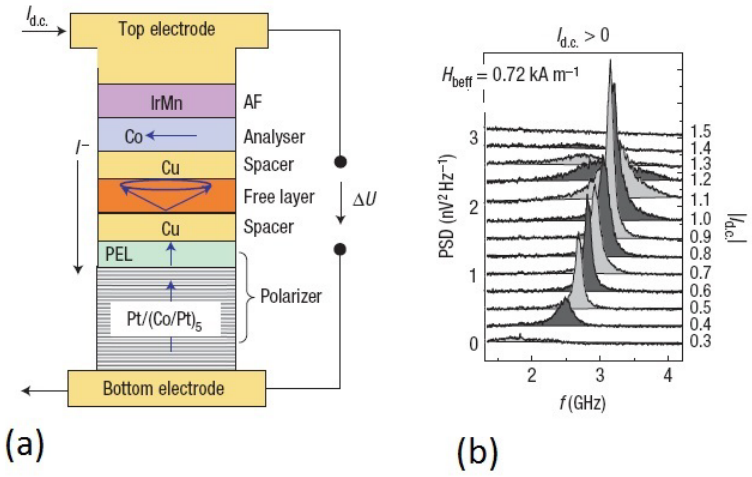

Figure 1.6: (a) Schematic diagram of a magneto-resistive cell consisting of a perpendicular polarizer. The precession of the free-layer magnetization creates an a.c. output voltage △U. (b) Power spectral density (PSD) of the output voltage △U. Reprinted from [Hous 07].

1.2.3 RF components

Another application of the spin-transfer torque is in auto-oscillations of typical RF oscillators such as Voltage Controlled Oscillators (VCO). This auto-oscillation happens when the energy lost in damping is compensated by spin-transfer torque and then, the magnetic moments of the free layer constantly precess (chapter 2). On example of spin torque oscillator is shown in figure 1.6(a). In this device the magnetization of the free layer is in-plane and the polarizer perpendicular-to-plane. STT generates a persistent precession at an angle which is related to the current density flowing through the structure (figure 1.6(b)). This continuous change of the angle between the magnetization of the free and fixed layers generates oscillatory resistance. Therefore, this device converts the spin-polarized dc current to an oscillatory voltage and frequency that can be adjusted by the choice of materials [Peti 07, Hous 07]. Current research is mostly focused on increasing the output power of spin torque oscillations (STOs). So that STO can truly find practical use as a radio-frequency (RF) device. The spin torque oscillators (STOs) have great application in wireless communication and radar communication. Also the RF components have many applications such as the GSM (Global System for Mobile communications).

Chapter 2

Theory of CPP-GMR and STT

2.1 Magnetic anisotropy

Anisotropy is the property of being directionally dependent, as opposed to isotropy, which implies identical properties in all directions. In magnetic materials, the dependence of magnetic properties on a preferred direction is called magnetic anisotropy. There are several different sources of anisotropy such as magnetocrystalline anisotropy and shape anisotropy. The magnetocrystalline anisotropy is an intrinsic property of crystals which is caused by spin-orbit interaction. In this section, domain magnetic configuration in single layer and multi layer and shape anisotropy of a pillar is briefly explained. Shape anisotropy plays an important role in the CPP-GMR and the spin-transfer torque devices.

2.1.1 Domain magnetic configuration in a single layer

A uniaxial anisotropy soft magnetic layer has three different domain configurations which is shown in figure 2.1. The first configuration is single-domain state (figure 2.1(a)) in which atomic moments of the film are aligned parallel because they have minimum exchange energy. Also the domain magnetization is aligned in easy axis to reach the minimum anisotropy energy. For ferromagnetic materials in this state (single-domain state), the demagnetization energy could be very high because of high magnetic charge. Therefore, the total energy of the system in the single-domain state is high [Nala 02].

The second configuration which is shown in figure 2.1(b) is called 'open structure'. In this configuration a single-domain state is broken to two subdomains with antiparallel magnetization alignment but both are aligned to the easy axis. In this case less charge is generated therefore demagnetization energy is reduced. The exchange energy increases and domain wall energy is introduced to the system [Nala 02].

Figure 2.1(c) shows 'closure domain' structure. The more subdomains with 90 degree walls are formed along the edges, and demagnetization energy vanishes because of complete closed flux (flux closure) within magnetic domain. The exchange energy and domain wall energy increases because of more domains. In this state anisotropy energy

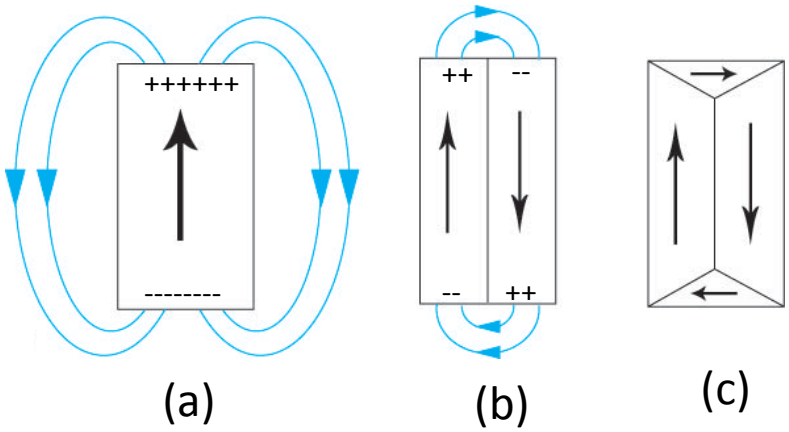

Figure 2.1: The typical magnetic domain configurations of a uniaxial anisotropy film. (a) Single domain state: In this configuration the demagnetization energy could be very high because of high magnetic charge. (b) Open structure in which a single-domain state is broken to two subdomains. (c) Closure domain structure: In this configuration more subdomains are formed along the edges.

is not zero because the domains which are located on edges are aligned perpendicular to easy axis. If the uniaxial anisotropy is not strong enough the edge domains will expand more to form 'diamond' [Nala 02].

2.1.2 Domain magnetic configuration in multilayer

The multilayer films are frequently used in GMR and spin-transfer torque devices. These multilayers are mostly two magnetic layers separated by either an insulation or a non-magnetic spacer. According to Slonczewski [Slon 88] a two layered laminated Permalloy (multilayer film) strip have three domain configurations. Closure domain pattern, easy axis state and hard axis state (figure 2.2). The closure pattern is similar to single-domain state configuration which is shown in figure 2.2(a). In this configuration the subdomains at the edges have different configurations. This is due to strong demagnetization fields or shape anisotropy of multilayer. In this state the demagnetization field overcomes the uniaxial anisotropy field and forces the magnetization of these subdomains to align parallel to the edge (parallel to shape anisotropy field). This shape anisotropy depends on thickness of the layer and size (in this case width) of the sample. By decreasing width of the stripe the shape anisotropy field increases and edge subdomains expand to form the diamond pattern in which vertical 180 degree walls no longer exist [Nala 02].

The second configuration is when two layers are in easy state domain. Figure 2.2(b)

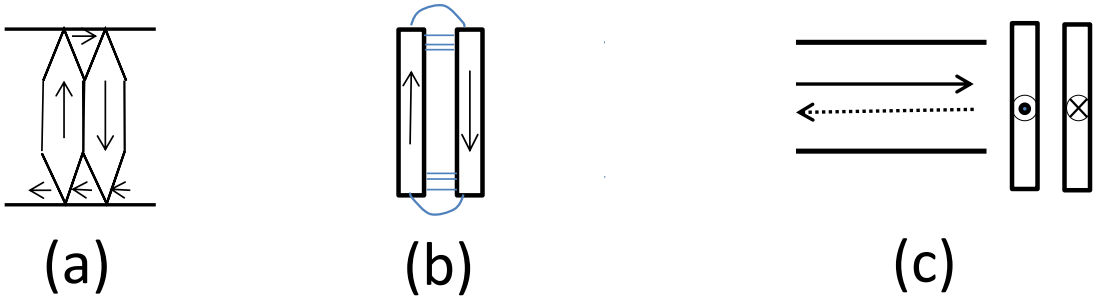

Figure 2.2: Magnetic domain configurations of laminated strip. (a) The closure domain state: In this configuration the subdomains at the edges have different configuration. (b) Easy-axis state: In this configuration the magnetization is aligned antiparallel along the easy axis. (c) Hard-axis state in which the two layers are oriented along their hard axis (adapted from [Slon 88]).

shows this configuration in which each layer is in single-domain state. The magnetization is aligned antiparalel along the easy axis and with two edge walls to form a closed magnetic circuit [Slon 88].

Figure 2.2(c) shows when the two layers are in hard axis state. This configuration happens when the strip width is very small and the energy required to keep moments in the easy axis state becomes very high compared to energy requirement for the hard axis state.

2.1.3 Magnetic shape anisotropy in the elliptical pillar

In ellipse-shaped pillars the magnetic shape anisotropy tends to align magnetization configuration to the long axis (easy axis) of the pillar. The magnetic charges are always positioned at the surface or boundary of the devices. Therefore, the distance of the magnetization to the surface charges is longer on the long axis of the pillar as compared to distance of the magnetization to the surface in short axis. Consequently, the magnetic energy becomes smaller and magnetizations aligned along the easy-axis becomes more stable than in the hard-axis of the pillar. The schematic picture of the energy barrier of the elliptic pillar is shown in the figure 2.3.

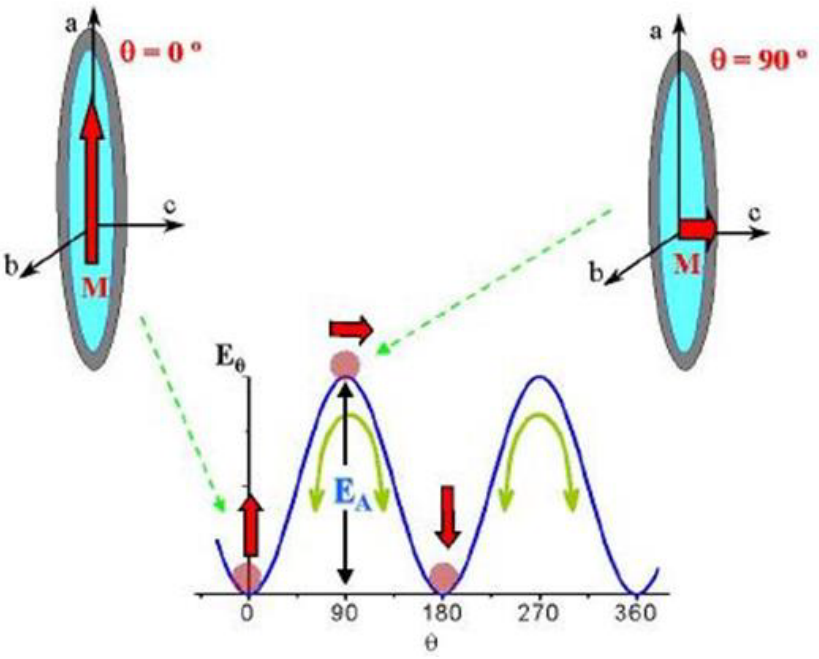

Figure 2.3: The energy barrier (E_θ) of the pillar versus the angle (θ). This energy is maximum (E_A) when magnetization of pillar (M) is aligned to the short axis (θ=90) and this energy is minimum when the M is aligned to the long axis (θ=0). The elliptical shape induces two stable states at +90° and -90° magnetizations. Reprinted from [Arel 08].

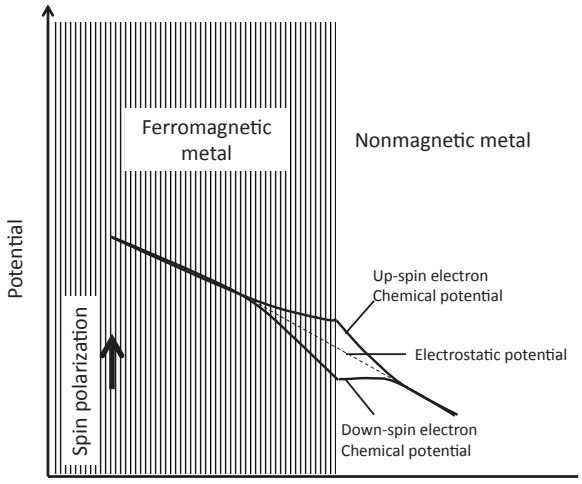

Figure 2.4: Distribution of the electrochemical potential of the up and down spins at a F/N interface. The spin accumulation generated by electrical current passing through an interface of ferromagnetic and nonmagnetic materials. Reprinted from [Satt 10].

2.2 Spin accumulation

One of the simplest systems to explain spin accumulation is an interface of ferromagnetic (F) and nonmagnetic metals (N) through which electron current passes [Satt 10]. The current is spin-polarized in the F layer sufficiently far from the F/N interface in which the spin-polarized means that the current densities of spin-up and spin-down electrons are not the same. On the other side, the current is unpolarized in the N layer. Therefore, there should be an adjustment of the up- and down- spin electrons around the interface. Hence the up-spin electron current (majority) shrinks at the interface and these majority spins accumulate around the interface. On the other hand, the minority spin current (down-spin) expands at the interface (figure 2.4). These spin currents (up and down) dissipate to the nonmagnetic side [Satt 10]. Because of shrinking and expanding of spin currents, the difference between populations of the up-spin and the down-spin electrons increases around the interface. This deviation of spin population from the equilibrium state is called spin accumulation. The spin accumulation modifies the electrochemical potential (ECP) of up- spin and down-spin electrons from their equilibrium states [Tomo 11]. Spin scattering (spin-flip scattering) which is generated by spin-orbit interaction and magnetic impurities and disorder destroys spin accumulation [Brat 06]. Spin accumulation occurs at the characteristic length of the spin diffusion length (the distance that an electron runs before the memory of spin state is lost). The spin diffusion length in ferromagnets are $(\ell_{sd}^{F}) \sim 5$ nm (Permalloy) - 50 nm (Co) and it can be very large in non-magnetic metals like copper ($\sim 1\ \mu$m) [Jede 01, Brat 06].

Another system which is also interesting for this thesis is applying a voltage over two ferromagnetic metal right and left electrodes (figure 2.5) and a thin non magnetic electrode at the center (F/N/F junction). As figure 2.5 shows a schematic of the F/N/F junction, this system has two interfaces. When a bias current is applied from left to right electrodes the electrochemical potential changes at the interfaces (figure 2.5(a)). As figure 2.5(b) shows the majority spin in the left layer is the spin-up electron at Fermi level and in right layer is spin-down electron at Fermi level. If we neglect spin-flip at the F/N interface, the conductance between the electrodes is proportional to density of state of each electrode at Fermi level [Satt 10]. In this configuration (antiparallel) density of spin-up electron current which comes to the nonmagnetic electrode is more than spin-down electron current (figure 2.5(b)) that means the current which comes to the nonmagnetic layer is spin-up polarized but the magnetization of the right ferromagnet is in opposite direction. Therefore the antiparallel configuration shows higher magnetic resistance.

A consequence of the spin accumulation in the F/N/F is giant magnetoresistance (GMR)[Baib 88, Bina 89] and tunnel magnetoresistance (TMR) [Mood 95]. Valet and Fert analyzed the CPP giant magnetoresistance of magnetic multilayers [Vale 93], and showed that spin-polarized currents flowing perpendicularly to the layers induce spin accumulation effects. The next section explains the macroscopic picture of the CPP-GMR in the F/N/F multilayer.

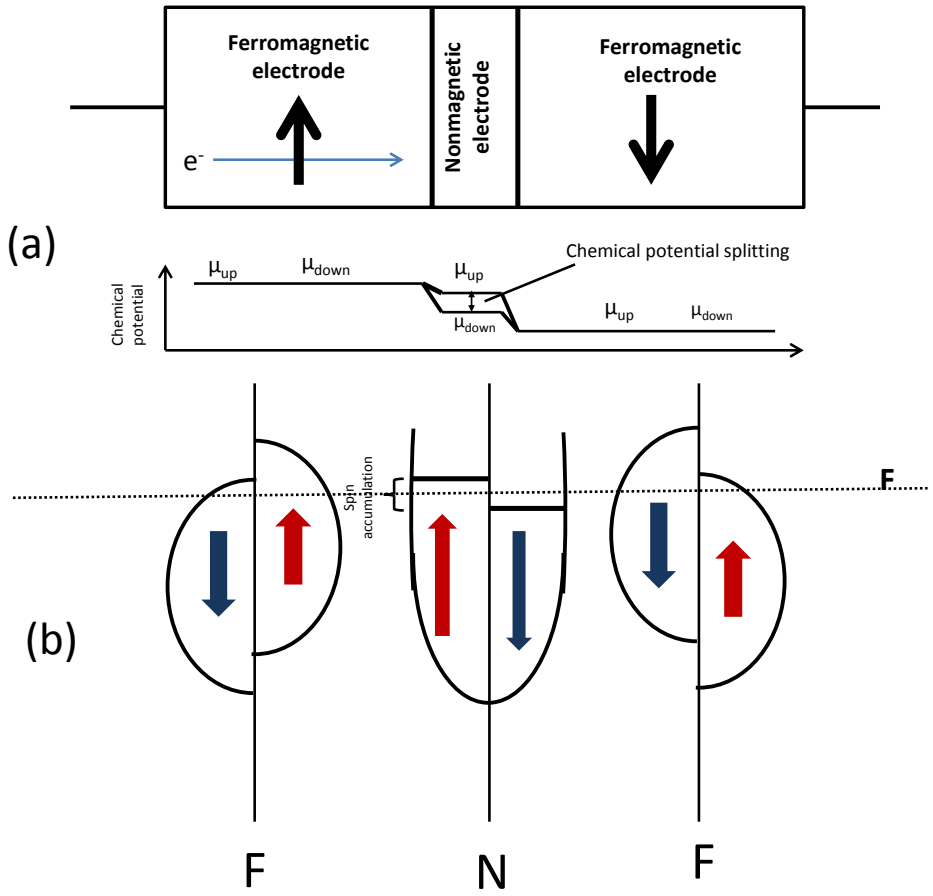

Figure 2.5: (a) A schematic of the F/N/F trilayer structured and chemical potential diagrams [Satt 10]. (b) The schematic picture of the density of state for each layer while the system is in antiparallel magnetic configuration (F : Fermi level) [Fert 02].

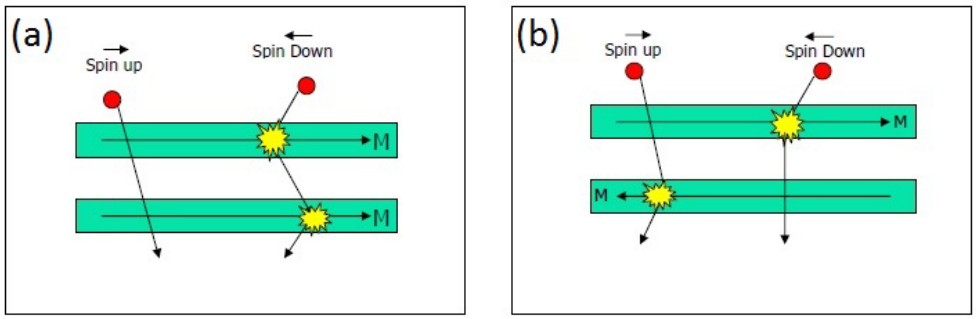

Figure 2.6: Schematic of the CPP-GMR. (a) Parallel alignment corresponds to low resistance. (b)Anti-parallel alignment corresponds to high resistance. Reprinted from [Chal 04].

2.3 CPP-GMR

The CPP-GMR can be briefly explained by a simple resistance model based on the two current model. In this model the total current is sum of the spin-up and spin-down electron currents, which are limited by two channel series resistors that represent interface and bulk scattering. As figure 2.6(a) shows when the magnetization of the two ferromagnetic layers are parallel, the spin-up electron current can pass through both layers smoothly and a low resistance is observed. When the magnetization of the two layers are antiparallel (figure 2.6(b)) both spin-up and spin-down electrons are blocked by one of the ferromagnetic layers and high resistance is observed [Chen 12].

Valet and Fert used the linear Boltzmann equation to analyze the giant magnetoresistance in the current perpendicular to plane [Vale 93]. They used two channel series resistor model taking the spin-diffusion length into account. They also included both volume and interface spin dependent scattering. Their model is very helpful for theoretical calculations of CPP-GMR devices and for understanding the physical process in those magnetic multilayers. However, in their semi-classical model, interface scattering is not discussed, but Quantum mechanical calculation on CPP-GMR have shown that interface scattering is very important and significant in the CPP-GMR devices [Sche 95, Zahn 95].

2.4 Spin-transfer torque induced switching

Pseudo spin-valves (PSV) devices are composed of $FM_1/NM/FM_2$ trilayers in which one of the FM layer is a hard magnetic layer and the other a soft magnetic layer. The equation of the Landau-Liftshitz-Gilbert (LLG) is used to describe the spin-transfer torque. This equation can be described by starting from equation of motion of a magnetization vector in the presence of an applied magnetic field [Burk 01]. Then this analysis is extended to

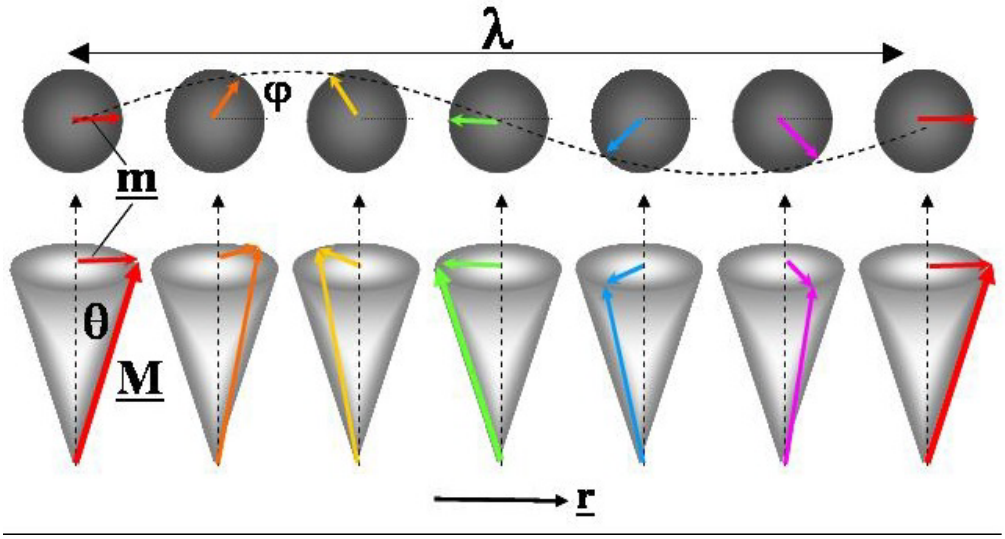

Figure 2.7: A schematic picture of a series of the plane waves of the magnetization in a small precession angle.

the addition of a phenomenological damping term. Finally, a spin-transfer torque (STT) term is added to these two parts and the LLG+STT equation is obtained [Laks 11].

When a magnetic field is applied to a magnetic material, the magnetization starts to precess in a direction that is normal to both magnetization and magnetic field. All changes to the magnetization state occur via the precessional motion. This equation is written under general assumption that the length of the magnetization vector is locally constant. And it is furthermore assumed that temperature is far below the curie temperature and there is no topological anomalies like vortices [Burk 01].

$$\frac{dM}{dt} = -\gamma M \times H_{eff} \qquad (\gamma = \frac{g\mu_B}{\hbar}) \tag{2.1}$$

In equation 2.1, the total magnetization is M = M_0 + m(R,t), M_0 is the vector of the saturation and m(R,t) is the variable magnetization. The amplitude of the m(R,t) is small compared to the saturation magnetization (M_0). When the angle of the precession is smaller, the variable magnetization (m) can be written as a series of plane waves of the magnetization or spinwaves [Burk 01],

$$m(R,t) = \sum m_K(t) \exp(iKR) \tag{2.2}$$

This precession around the equilibrium (small angles) can generate a thermally exited spin waves and ferromagnetic resonance. Figure 2.7 shows a schematic picture of a series of plane waves of magnetization in a small precession angle.

After some finite time, the magnetization aligns with the applied field, therefore a damping term should be added to the precession equation. Gilbert' idea is that the damping should be proportional to dM/dt [Gilb 04]. Therefore, the precessional equation 2.1, modified according to Gilbert's work, is generally referred to as Landau-Lifshitz-Gilbert equation:

$$\frac{dM}{dt} = -\gamma M \times H_{eff} + \frac{\alpha}{M_s} M \times \frac{dM}{dt} \tag{2.3}$$

In this equation α is damping constant which is typically 0.01 for metals. Figure 2.8(a) shows a schematic of precession and damping. The time scale of the precession is in the order or below nanoseconds (ns) and the damping is a few nanoseconds.

In the presence of the spin polarized currents, it is needed to add an additional term to the Landau-Lifshitz-Gilbert equation (equation 2.3).

$$\frac{dM}{dt} = -\gamma M \times H_{eff} + \frac{\alpha}{M_s} M \times \frac{dM}{dt} + \frac{\gamma}{M_s \mu_0} \tau \tag{2.4}$$

In this equation M_s is the saturation magnetization and τ is the vector of Slonczewski' spin-transfer torque [Zhan 02].

$$\tau = a_j M \times (M \times P) + b_j (M \times P) \tag{2.5}$$

P is the polarization vector of the fixed layer magnetization. a_j is the in-plane torque efficiency (τ_{ST} in figure 2.8(a)) and b_j is the perpendicular torque efficiency (τ_H in figure 2.8(a)), both of them are proportional to the current through the free layer I(t) [ZHOU 09] and they are capable to switch the magnetization moments [Zhan 02]. In the MTJ, b_j is substantial while it is negligible in the metallic spin-valves.

The spin-torque depends on the direction of the current. The most interesting effect happens when the spin torque is opposite to the damping direction. Then, the stationary state becomes unstable. Generally, this instability position can be categorized into two types: switching and persistent precession.

2.4.1 Magnetic switching

The magnetic switching in multilayer usually occurs in elliptical shaped pillars with uni-axial anisotropy higher than external magnetic field [Myer 99, Kati 00]. As picture 2.9 shows, the ellipse shaped devices have easy axis along the long axis at zero or small field which corresponds to local energy minimums. In the magnetic switching, the spin-transfer torque switches the magnetization between these two directions.

One example of the magnetic switching is ferromagnet/spacer/ferromagnet pillar. In these devices one of the ferromagnetic layer is thicker or harder, therefore the spin torque

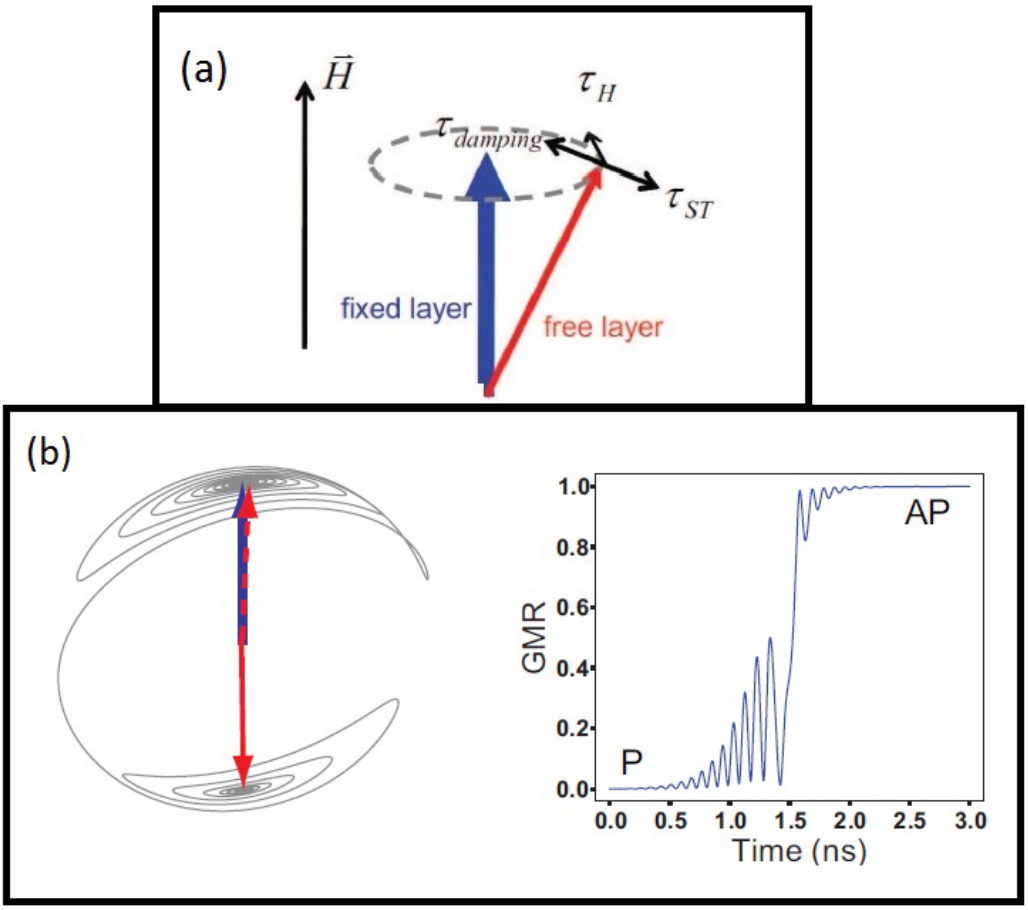

Figure 2.8: Magnetization dynamics in the presence of spin-transfer torque. (a) Directions of the field torque τ_H, the damping torque $\tau_{damping}$, and the spin-transfer torque τ_{ST}. (b) The magnetization trajectory of the spin-transfer induces the magnetization switching (left picture) and the normalized GMR as a function of time (right picture) (pictures are taken from [Chen 12]).

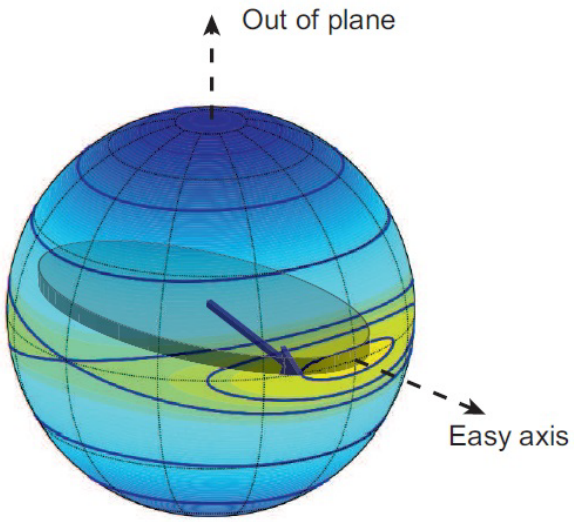

Figure 2.9: The anisotropy energy of a elliptical nanomagnet (picture taken from [Cui 12]).

has less effect on this layer. This fixed layer serves as a polarizer (PL) and generates spin polarized current. The other ferromagnetic layer is usually thinner or softer compared to the PL and this layer is named the free layer (FL). Spin torque can change the magnetization of the FL. Figure 2.10 shows dependence of the spin torque on the direction of the current. The electrons get polarized by flowing from the PL to the FL (figure 2.10(a)), then the exchange interaction between the conduction electron spins and the magnetization of the free layer applies a torque on the local magnetization of the free layer. Therefore, the magnetization of the free layer rotate towards the polarizer layer direction.

When the current direction is from the free layer to polarized layer, the spin-down electrons are reflected from the PL apply a torque on the free layer. These reflected electrons with opposite spins (down-spin) rotates the magnetization of the free layer pointing towards the antiparallel configuration (figure 2.10(b)). In magnetic switching, a spin current from the free layer to polarized (fixed) layer destabilizes the parallel configuration. Therefore the magnetic moment of the free layer precess around the easy axis, and by increasing the current the amplitude of this precession increases and it switches to opposite direction of easy axis which is the other local energy minimum point. In this position the spin torque and the damping are in the same direction and the magnetization of the free layer relaxes in the antiparallel mode. Figure 2.8(b) shows a simulated spin-transfer torque induced switching.

The applications of this type of spin-transfer torque induced switching are in writing and reading in magnetic random access memory (MRAM). Researches on this topic is focused on realizing switching process with higher speed and low energy consumption [Chen 12] by decreasing the critical current.

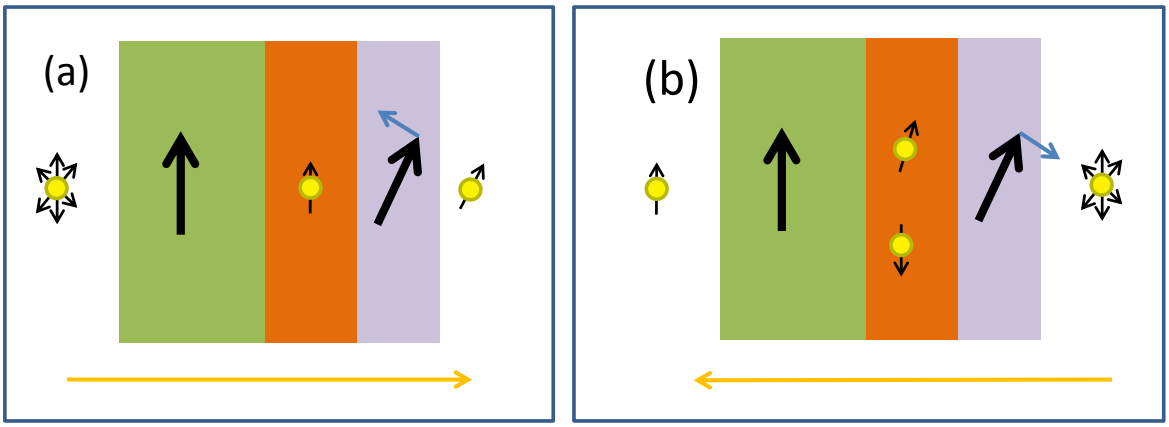

Figure 2.10: The dependence of the spin-transfer torque on the direction of the current. (a) The electron flow is from the fixed layer (NiMnSb layer) to the free layer into parallel alignment. (b) The electron flow is from the free layer (Py layer) to the fix layer into anti-parallel alignment.

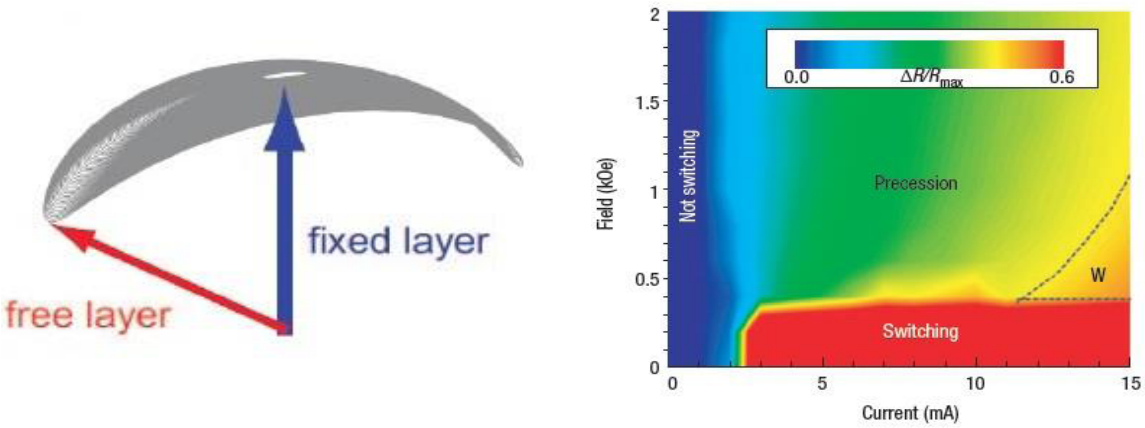

Figure 2.11: (a) The magnetization trajectory of persistent precession driven by spin-transfer torque. (b) Phase diagram of the normalized magnetoresistance ($\triangle$R/R$_{max}$) with changing currents and fields. The W region corresponds to formation and annihilation of dynamic vortices through the interaction of the large current and spin torque. In this system the resistance decreases from the full antiparallel value without exhibiting well defined precession (reprinted from [Lee 04]).

2.5 Persistent precession

The second category of spin torque dynamic is the persistent magnetic precession which usually occurs when a large magnetic field is applied on the sample. Figure 2.11(a) shows the simulated magnetization trajectory of the persistent precession. In this case, the sample has one local energy minimum which is along the magnetic field direction. The spin torque excites the magnetization of the free layer but there is not any other stationary equilibrium state. Therefore the free layer stays in the precession mode and the steady state is a periodic oscillation (auto-oscillation). Indeed, the spin torque cancels the damping on average of one cycle of precession. This persist precession generate a GHZ microwave voltage oscillation which can be tuned by changing the magnetic field or the applied current. Therefore, the spin transfer nano-oscillator (STNO) can be used as nanoscale tuneable microwave oscillator [Cui 12]. The spin transfer driven dynamics can be measured by time-resolved measurements and microwave power emission spectrum [Kriv 05, Kriv 08, Kati 00]. The first experiment on the persistent precession dynamic was observed by Kiselev et al [Kise 03] in the nanopillar geometry and Rippard et. al [Ripp 04] in the point contact geometry. After that, there have been significant researches on the persistence microwave dynamics of magnetization driven by spin-polarized current. Figure 2.11 (b) shows a simulated phase diagram of normalized magnetoresistance ($\triangle R/R_{max}$) with changing currents and fields for a nanopillar. The precession phase is used on spin-oscillators and the switching phase is used on spin torque memory and logic devices (chapter 1).

Furthermore, the output power is an important issue in this persistent precession. The output of the spin valve devices like GMR are small, therefore the researches focused that the microwave oscillation MTJ devices can have higher output [Deac 08, Hous 08]. another method to increase the output is the mutual phase locking between nano-oscillators [Kaka 05, Manc 05]. In this method the microwave oscillators from the contact pairs can add up to give a larger signal.

2.6 Half-metal

The layer stack which is used for this thesis contains two ferromagnetic layers, permalloy and the NiMnSb half-Heusler alloy. This half-metallic Heusler alloy has been explained theoretically by de Groot et al [Groo 83] in 1983. they showed that the band structure of the NiMnSb half Heusler alloy had a metallic band structure for the up spin (majority spin) band, whereas the down spin (minority spin) band had a semiconducting gap at the Fermi energy. Figure 2.12 shows the band structure of NiMnSb in the majority and minority-spin directions. These materials are called half-metals because they have the metallic property for only one spin direction. So far, half-Heusler alloys, full-Heusler alloys, Perovskite or double Perovskite oxides, the binary magnetic oxides (Fe_3O_4, CrO_2, $Co_{1-x}Fe_xS_2$), colossal magnetoresistance materials ($La_{0.7}Sr_{0.3}MnO_3$, Sr_2FeMoO_6), Co_2MnSi etc, are predicted

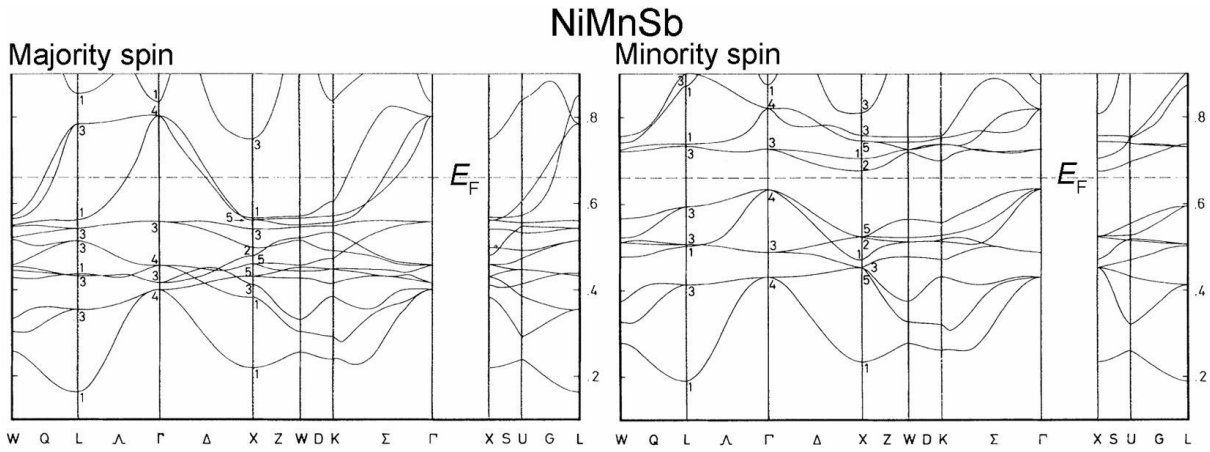

Figure 2.12: Calculated spin-resolved band dispersions of NiMnSb by de Groot (reprinted from [Groo 83])

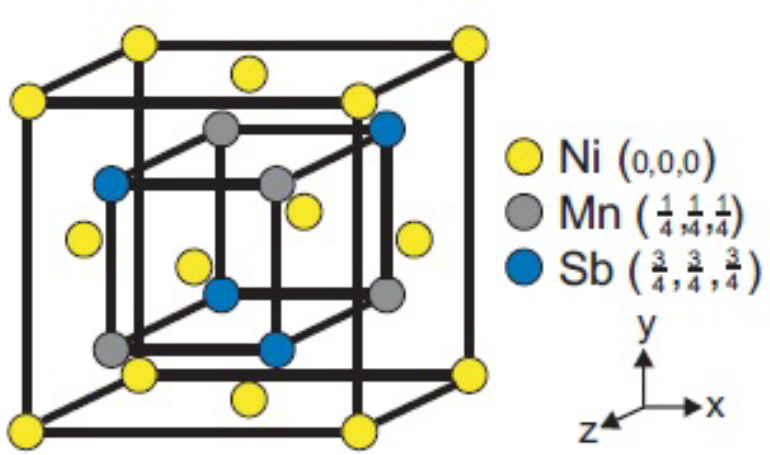

Figure 2.13: The schematic crystal structure of half-Heusler NiMnSb

to be half-metals. The half-Heusler alloys generally have high Curie temperature (730 K for NiMnSb and 980 K for Co_2MnSi) and their conduction electrons at the Fermi level are 100% spin polarized. Although some percentage of the conduction electrons may loose their polarization at each interface [Soul 98, Eid 03], these materials can be used for high spin polarized current sources to realize a very large magnetoresistance, a low current density for induced magnetization reversal and an efficient spin injection into

semiconductors.

The origin of half-metallic gap in Heusler alloys is connected to their crystal structures. The half-Heusler alloys have the composition of XYZ and the $C1_b$ structure, where X and Y are transition metals and Z is a main group element. In the $C1_b$ structure the atomic positions are X (0, 0, 0), Y (1/4, 1/4, 1/4) and Z (3/4, 3/4, 3/4). Figure 2.13 shows the schematic crystal structure of half-Heusler NiMnSb.

In this thesis NiMnSb is used as a polarizer in the multilayer which is grown on an InP substrate with an (In,Ga)As buffer. The (In,Ga)As layer is used to reduce the lattice mismatch between NiMnSb (5.903 Å) and InP (5.868 Å), therefore the crystalline quality of the NiMnSb increases [Loch 12].

Chapter 3

Fabrication of Pseudo spin-valve device

3.1 Introduction

For observations of spin-transfer torque and GMR, devices with small cross-section areas are needed for several reasons. The first reason is that the spin torque devices required fairly high current density. This current density is in the order of 10^6-10^8A/cm^2. Therefore by applying the same current, the smaller devices have the higher current densities compare to the bigger ones. The second reason is the nano-structures have a uniform magnetic domain, which has controllable magnetization, and the spin-transfer torque is more effective at the smaller dimension magnetic devices [Leem 10, Stil 06]. Finally, the small cross-section area increases resistance of the metallic multilayer stack which makes detecting a spin valve signal easier. Therefore the devices with small cross-section areas are essential for investigation of the spin-transfer torque and the GMR effects.

There are several ways to get a small cross-section area for the observation of spin-transfer torque and GMR. Mechanical point contact is one of the simplest. In this method, a sharp needle is slowly pressed into a magnetic multilayer stack. The first observation of spin-transfer torque by this method is reported in [Tsoi 98]. Nowadays, the devices with smaller cross-sections are made by nanolithography. In other words, the method of getting a small cross-section area is fabricating of a nanopillar [Kati 00]. Since the size of devices plays an important role in investigation of spin transfer phenomena, we have developed a new method for fabrication of nanopillar. In the present chapter old fabrication method (by using a resist mask) and new fabrication method (by using a metal mask) are described.

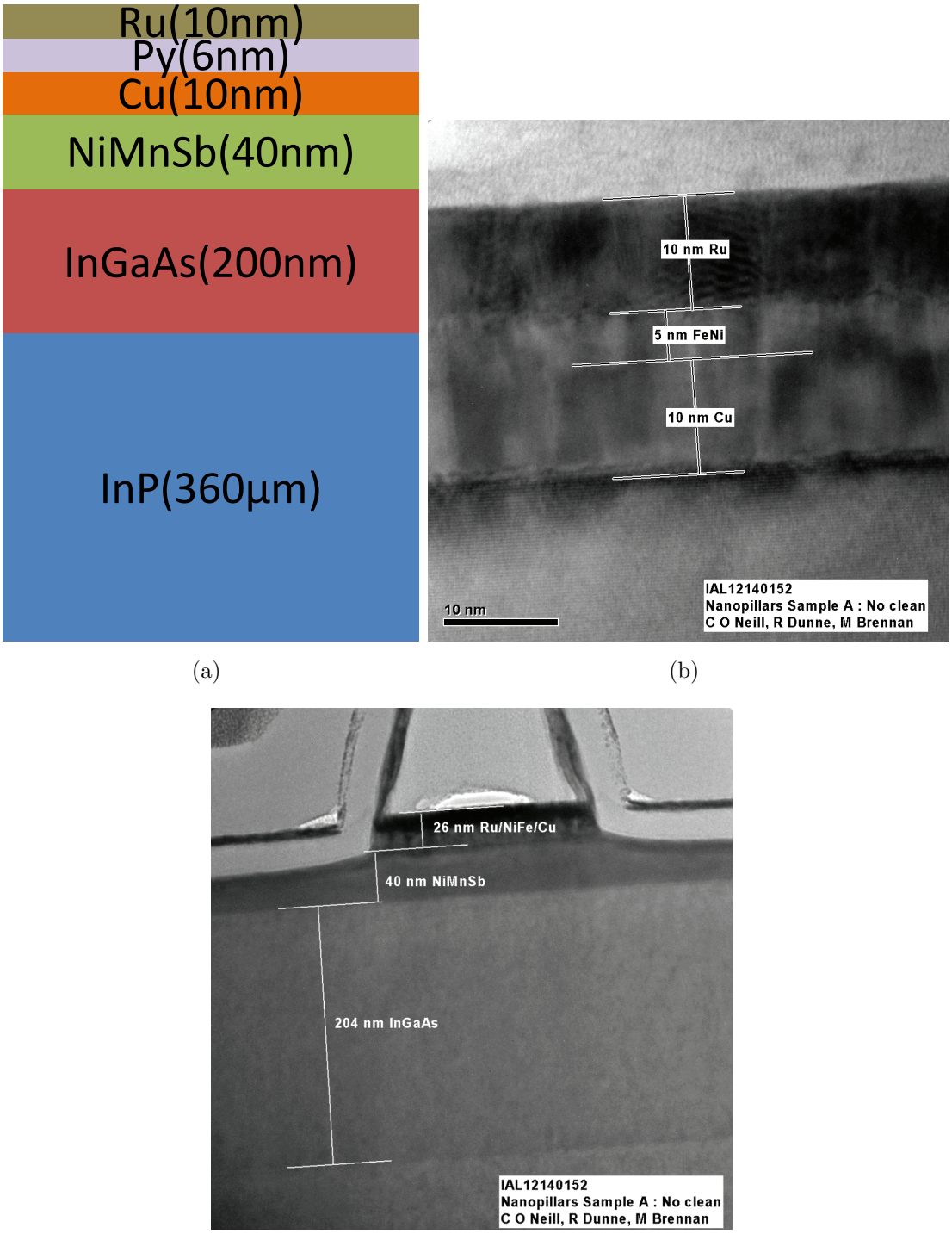

(a) (b)

(c)

Figure 3.1: (a) A schematic layer stack of the device. (b,c) Transmission electron microscopy (TEM) cross-section images of the layer stack. Pictures are taken by Intel, IAL TEM group.

3.2 Layer stack

Layer stack which is used in this thesis contains Ru(10nm)/Py(6nm)/Cu(10nm)/NiMnSb (40nm)/(In,Ga)As(200nm)/InP:S(360μm). NiMnSb is grown on InP(001) by molecular-beam epitaxy (MBE) using a lattice matched (In,Ga)As buffer [Bach 03, Loch 12]. After MBE growth the sample is transferred under ultrahigh vacuum (UHV) conditions to an UHV dc-sputtering system with base pressure below 10^{-7} Pa where a Cu layer and subsequent NiFe alloys (Py) and Ru layers are sputtered. A schematic and transmission electron microscopy pictures of the layer stack is shown in figure 3.1. In the layer stack which is used for the CPP-GMR and the spin torque device the substrate layer (InP:S) is conductive.

3.3 Fabrication of the pillar using a resist mask

Fabrication of a nanopillar is always a challenging process. One of the fabrication methods, using a resist mask, is briefly explained in A. Riegler's thesis [Rieg 11]. Unfortunately, this method had a very low yield of functioning structures. In the following paragraph, we show drawbacks of this method, and then we describe our new method of the nanopillar fabrication.

In fabrication of a pillar with the resist mask, a reversal Novolak-based resist from ALLRESIST GmbH (600 nm thick, figure 3.2(a)) is used. The pillars with various sizes 80 nm×200 nm, 300 nm×150 nm and 500 nm×300 nm are patterned by using an electron beam lithography (EBL) system consisting of a LEO 1525 scanning electron microscope (SEM) and an ELPHY PLUS pattern generator from Raith GmbH. The resist is used in its negative mode, therefore after EBL a post exposure baking (PEB) step (figure 3.2(c)), at 105 ℃ for 10 minutes) is used and the process is followed by flood UV-exposure for 20 seconds (figure 3.2(d)). This exposure is followed by the development in a water-based alkaline developer. After the development, a high column of resist (the resist mask) is formed. Schematic and SEM pictures of the resist mask after development are shown at figures 3.2(e) and 3.3(a), respectively. This mask serves for subsequent etching. Dry etching is used because the method gives us precise control on the etching rate as compared to wet etching. Also, the multilayer stack is usually difficult to etch with one etchant. Moreover, dry etching is the best choice for fabrication of the devices with small dimensions. The sample is etched in a CAIBE (chemically assistant ion beam etching) system by Ar^+ ion beam etching to reach the NiMnSb (Heusler) layer. In order to avoid trenching around the pillar [Some 76], the position of the sample with respect to etching beam incidence is set to 70°. The etched sample is transferred immediately into a PECVD (plasma enhanced chemical vapour deposition) machine (Plasmalab 80 Plus from Oxford Instruments) and an insulating SiN layer with a thickness of 50 nm is deposited (figure 3.2(f)). Afterwards, a lift-off process for removing the resist mask is carried out in NEP (N-ethyl pyrollidone) at 80 ℃. Application of ultrasonic agitation during lift-off assists

the process (figure 3.2(g)), but the resist mask rarely lifts off. More details of fabrication of the pillar with a resist mask are explained in appendix A.

The difficult lift-off process and the resist redeposition during dry etching, often gen-

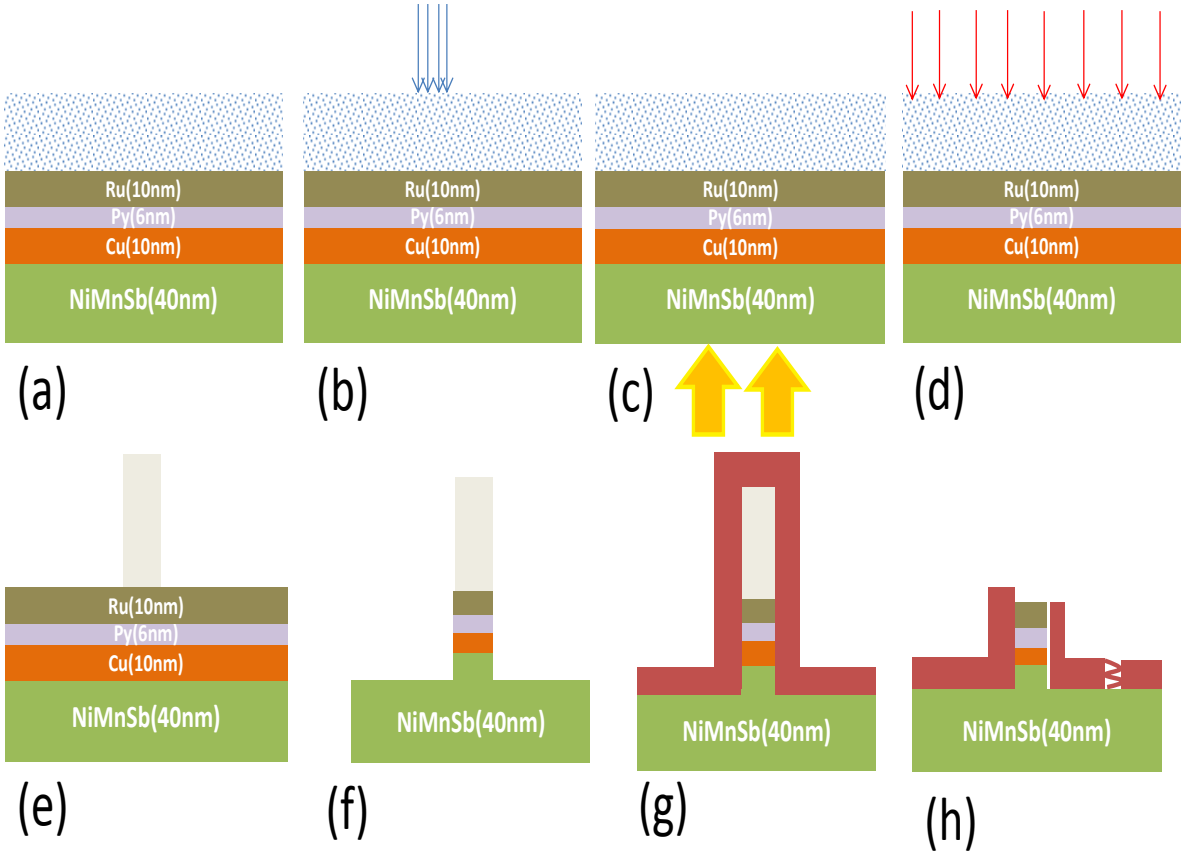

Figure 3.2: Schematic procedure of the pillar fabricated with the resist mask. (a) The resist is spin-coated on the sample. (b) The resist is exposed by EBL. (c) Post-exposure baking after EBL. (d) Flood UV-exposure. (e) After development, the patterned resist is formed for etching. (f) The sample is etched by Ar^+ ion beam etching. (g) An insulating SiN layer with a thickness of 50 nm is deposited on the etched sample. (h) The schematic picture of side walls, leakage through the side of the pillar and cracks in SiN.

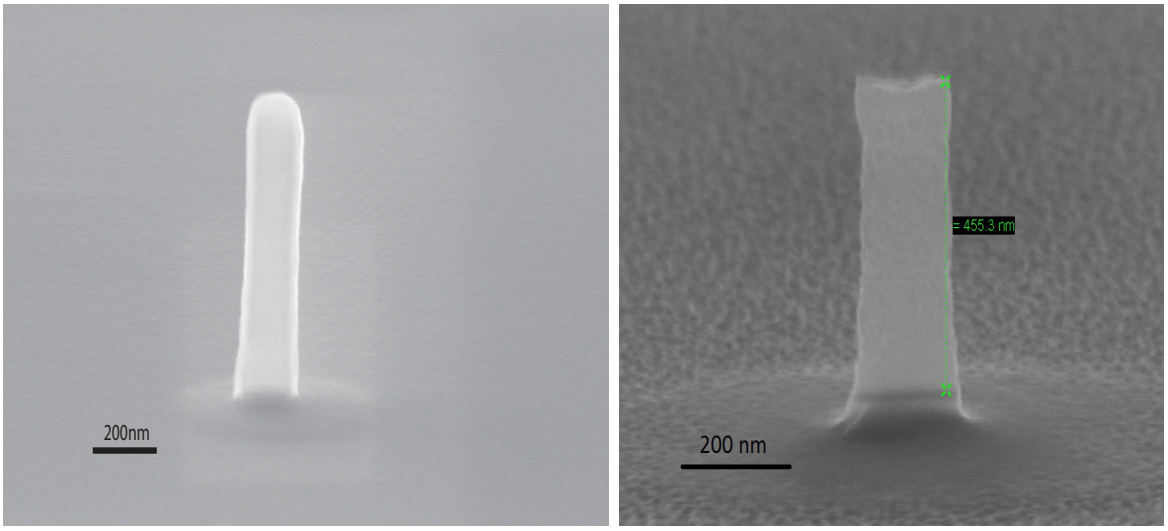

(a)

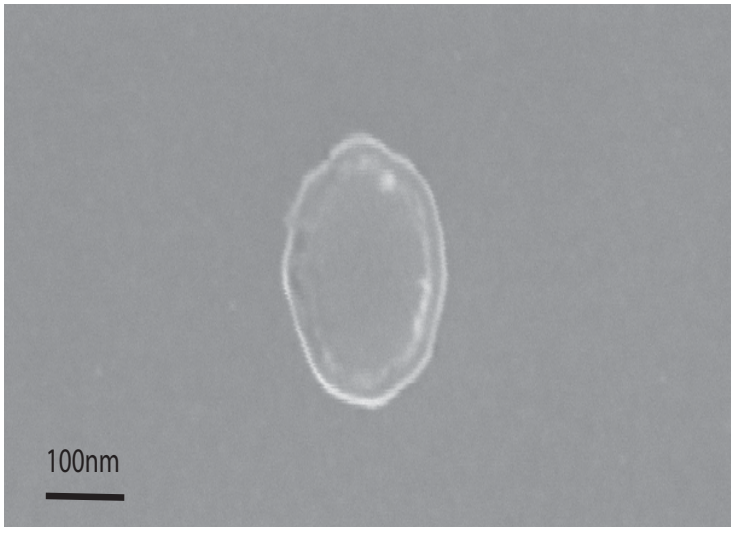

(b)

Figure 3.3: (a) Skew view of the etched samples with resist mask. (b) Top view of a pillar after the resist mask is removed.

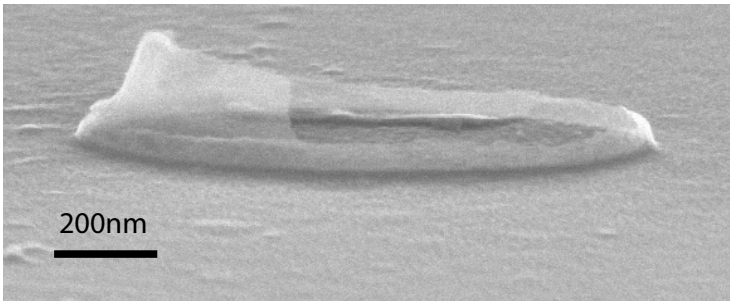

(a)

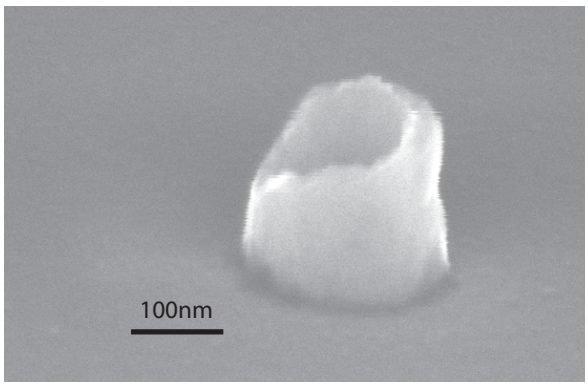

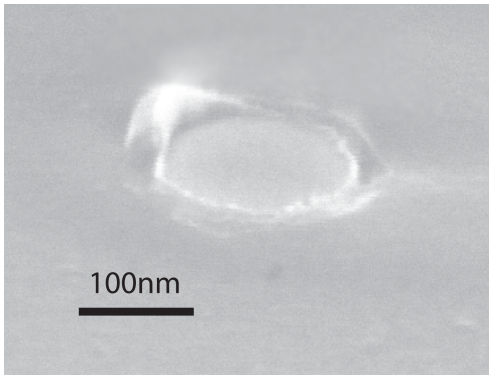

(b) (c)

Figure 3.4: (a) (b) SEM pictures of the samples show the side walls around the pillar. (c) The side walls can tear off the etched pillar.

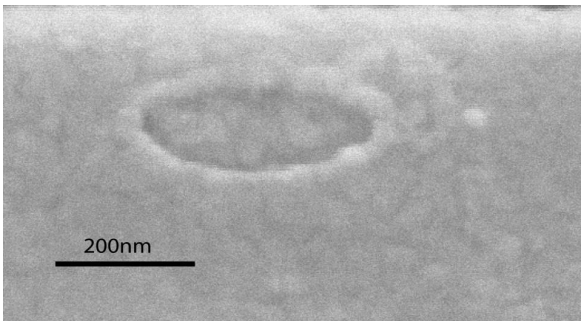

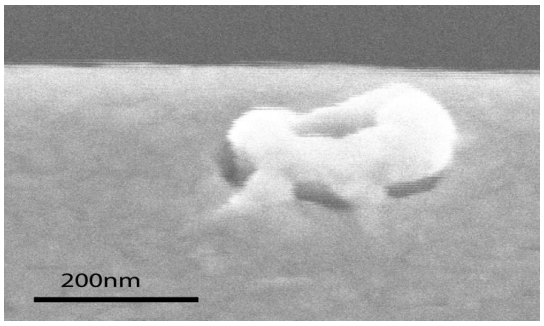

(a) (b)

Figure 3.5: (a) The resist mask is removed successfully. (b) The side wall causes a bad contact to the pillar.

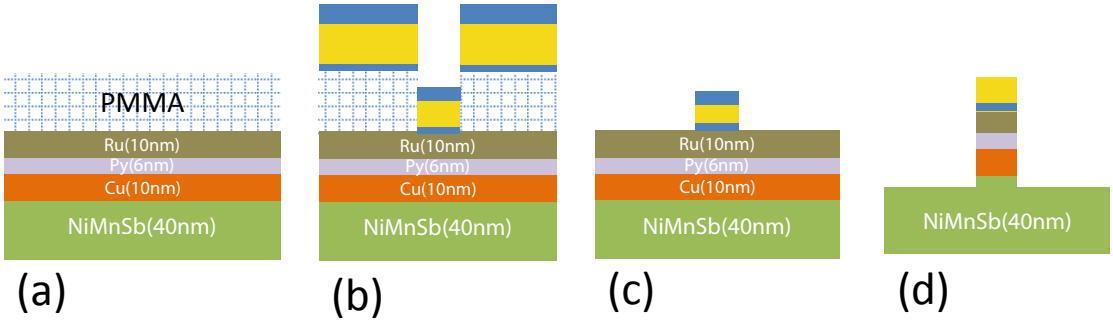

Figure 3.6: Schematic positive procedure of fabrication of the pillar with the metal mask. (a) PMMA resist spin-coated on the sample. (b) the sample is metalized (Ti/Au/Ti) after e-beam exposure and development. (c) Lift-off is done and the metal mask is made. (d) The sample is etched and the pillar is patterned under mask(Au/Ti).

erates thin standing walls around the pillar. These standing walls (side walls) are formed because the insulator (SiN) deposition is a conformable coverage which means the SiN layer cover all of the surfaces and lateral walls of the resist mask and the pillar. Figures 3.4 shows some examples of these standing walls around the pillars. Later these standing walls will cause bad contact to the pillar (figure 3.5). Moreover, these walls can be torn off from the side walls of etched pillars (figure 3.4(c)) and opened the pillar sides for contacting metal. Also, as we found that ultrasonic agitation which is used for lift-off often damages the SiN layer and generates pin-holes and micro-cracks in it. Therefore, during electrical measurements, current can penetrate through the SiN layer around the naked side walls, and the pillar is shorted. Because of all these problems, we decided to change the fabrication process. In the new method the pillar is fabricated with a metal mask.

3.4 Fabrication of the pillar using a metal mask

In this section a new method of the nanopillar fabrication is explained. The first step in this method is the fabrication of a metallic mask for the pillar. Two PMMA layers, PMMA 600 K (4 %) and PMMA 950 K (3 %) are used for patterning the mask. The first PMMA (600 K, 4 %) spin-coated on the layer stack at 5000 rpm and baked at 180 ℃ for 1 hour. Subsequently, the second PMMA layer (950 k, 3 %) spin-coated at 7500 rpm and baked at 200 ℃ for 1 hour. The metal mask with various dimensions of 700 nm×350 nm, 500 × 250 nm and 300 nm × 150 nm are patterned in a positive resist mode as shown in figure 3.6. After e-beam exposure and development, the sample is metalized in the evaporation machine. The metal layers are Ti (5 nm), Au (95 nm) and Ti (13-24 nm), from bottom to top (figure 3.6(b)). The thickness of the top Ti layer has to be chosen in a way that the Ti layer is completely removed during the ion milling time. This is

because Ti will oxidize very fast and TiO_2 is not conductive. By lifting-off unexposed resist in the acetone, the metal mask is made (figure 3.6(c)). Ti/Au/Ti are used as a mask for Ar^+ ion milling to define the nanopillar structure. The sample is etched by Ar^+ IBE at an angle of 70° for 85 seconds. The milling is timed to stop after 10 nm removal of a 40 nm thick NiMnSb layer (30 nm of the layer stays unpatterned). The Ti layer (top layer of the mask) is etched away after the Ar^+ IBE and the Au layer is on top of the structure. This Au layer later is used to contact the pillar. Also, by using the metal mask for etching we avoid the side walls which are generated by redeposition of sputtered material onto the lateral walls of the pillar during ion beam milling. In the case of the thick resist mask (first method), redeposition material can remain after the mask removal and cause a problematic contact on top of the pillar [Gloe 75] and [Deng 13]. The 70° tilt during IBE produces only a very thin redeposited layer from the etched material which makes shorting at the layers in the stack unlikely. To be completely sure that shorting does not take place, we often do 15 seconds of Ar^+ IBE at 10° sample position in the CAIBE machine [Peng 09].

Figure 3.6(d) shows a schematic picture of an etched pillar. And figure 3.7(a) shows a SEM image of the pillar after the beam etching with CAIBE. In Figure 3.7(a) thin dark layer near the bottom of the pillar is 5 nm thin Ti layer. Above the Ti layer is 90 nm of gold and bellow it there are patterned layers (Ru/Py/Cu/NiMnSb) which are not well distinguished. The top Ti layer is completely etched away during the milling time.

3.4.1 Cross-linked PMMA

Insulation of the pillar from lead on top is second step after making the pillar. Therefore, the pillar must be covered with an insulator and access to the top of the pillar has to be organized via the openings in this insulating layer. There are two ways to insulate the pillar, one is the sample covered with SiN (an insulator) after Ar^+ etching and the other is using two insulators one cross-linked PMMA and SiN which we used in our method. At the beginning when we started the new method of fabrication, we used SiN deposition after Ar^+ etching and we tried to open a hole on top of the pillar. The problem was, any small misalignment during EBL could shift this hole and open the lateral walls of the pillar. Subsequently deposited Ti/Au contact will not be connected straitly to the top of the pillar (figure 3.8). Also, chemicals used in the PECVD machine for SiN deposition can attack the lateral area of the pillar causing loss of quality of the grown layers. Therefore, we needed to protect the pillar before the SiN deposition. This brought us to the idea to use an additional insulator around the pillar before the SiN deposition. The PMMA resist, Poly (methyl methacrylate), used in its negative mode (cross-linked PMMA) is well suited for this purpose. The cross-linked PMMA is created at high dose resulting in a shield around the pillar. Also, the cross-linked PMMA can be patterned by EBL at the correct position. It has a perfect adhesion to the pillar walls, and it is compatible with other process steps and the materials. The cross-linked PMMA can not be dissolved in

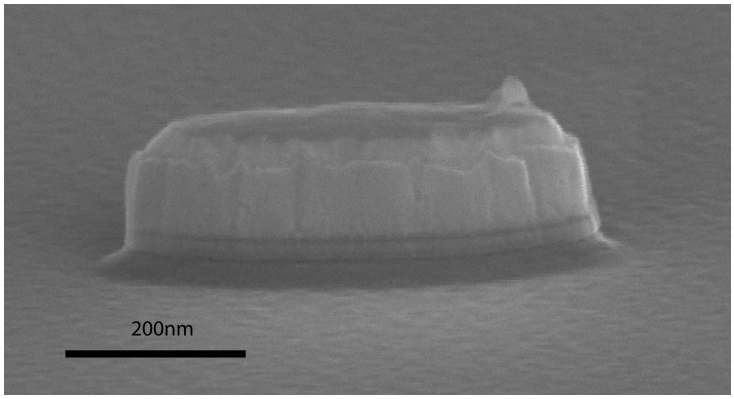

(a)

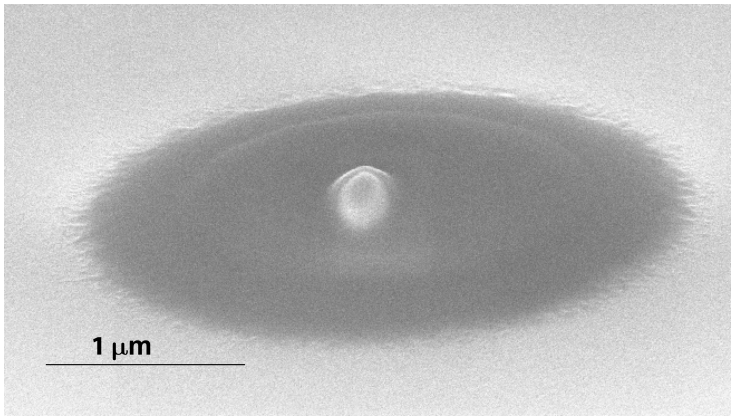

(b)

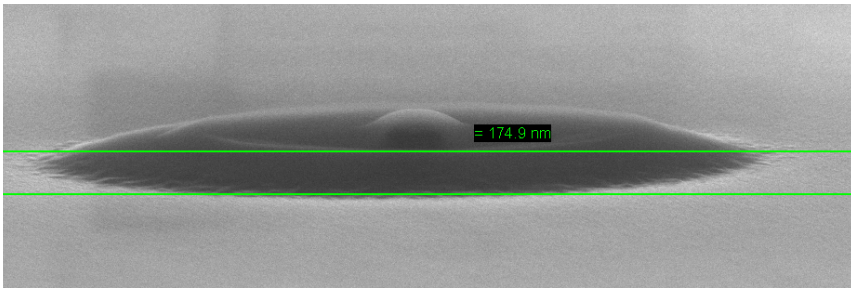

(c)

Figure 3.7: SEM pictures of the device. (a) The pillar after Ar^+ etching, thin dark layer near the bottom of the pillar is 5 nm thin Ti layer, above the Ti layer is $\sim$ 90 nm gold and bellow it there are patterned layers (Ru/Py/Cu/NiMnSb). (b, c) Skew view of the pillar covered with cross-linked PMMA and SiN.

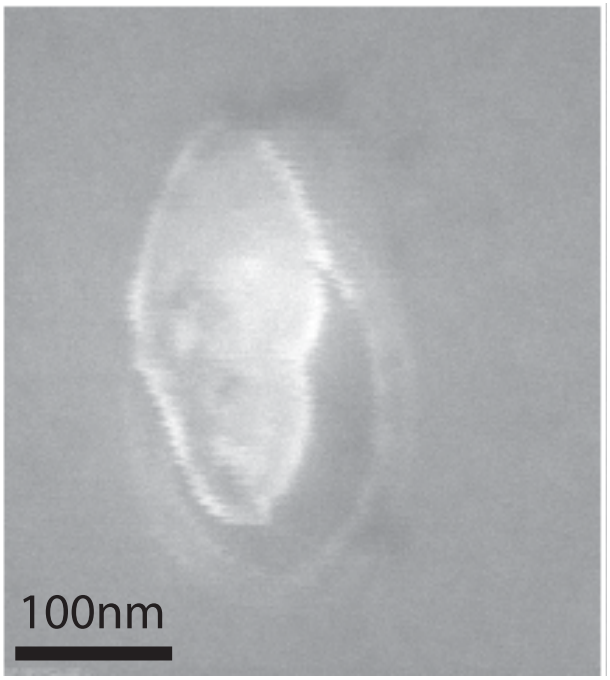

Figure 3.8: Hole on top of the pillar is shifted.

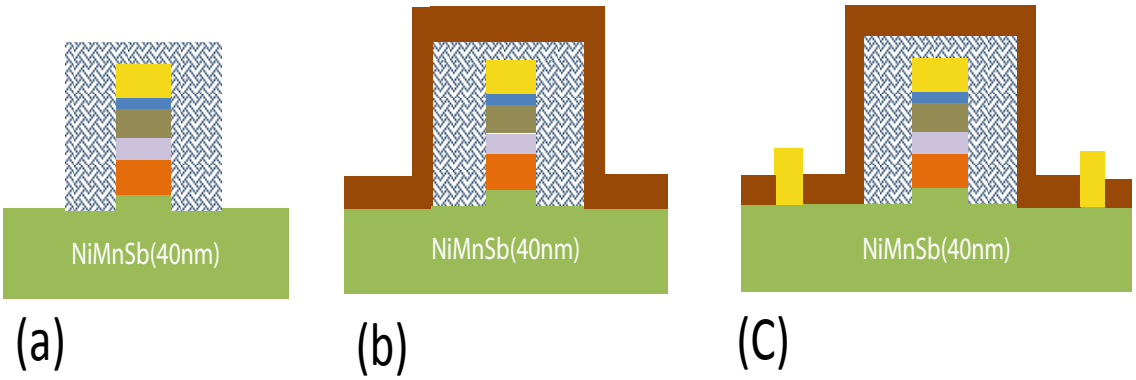

Figure 3.9: Schematic procedure of (a) cross-linking, (b) SiN deposition and (c) access to bottom contacts.

solvents but it is easily etched by low power oxygen reactive ion etching (RIE) [Zail 96] and [Hatz 69]. This means that it can be completely removed or its thickness can be adjusted by oxygen RIE. The resist which is used for cross-linking is PMMA 600 K (4 ٪) spin-coated at 5000 rpm. After that, the sample is baked at 180 ℃ for 30 minutes. The PMMA layer is exposed by high dose electron. After development in acetone for 10 minutes, the pillar on the surface is buried in the cross-linked resist. The schematic picture of the cross-linked PMMA around the pillar is shown in figure 3.9(a). As a preliminary to the next step (which is SiN deposition), we refresh the surface with a brief Ar^+ IBE

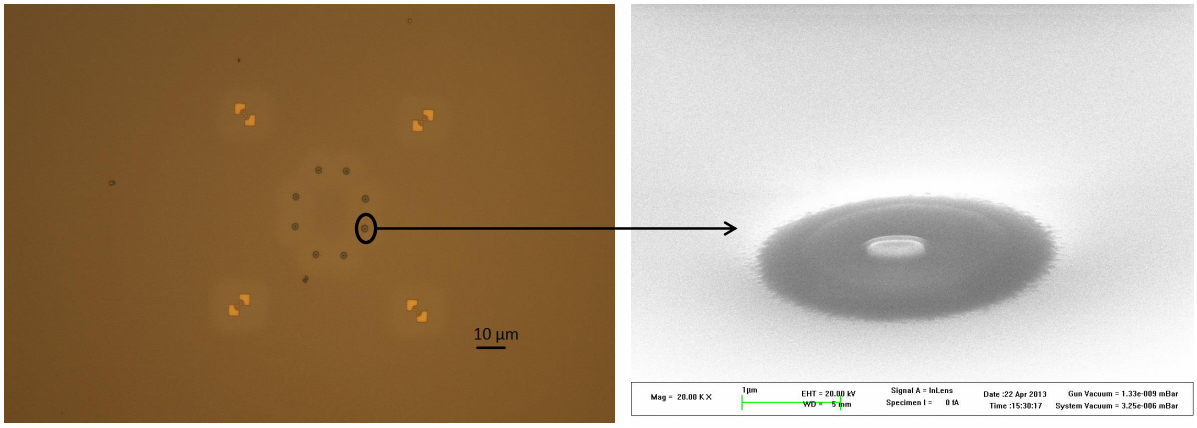

Figure 3.10: Left picture shows an optical picture of a sample which eight pillars are patterned and right picture shows a pillar covered with cross-linked PMMA and SiN.

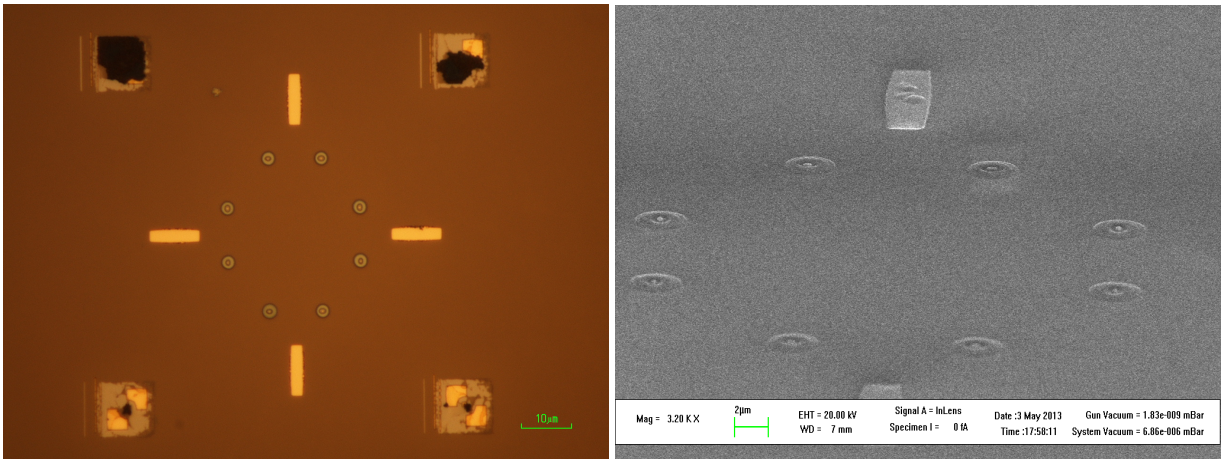

Figure 3.11: Optical (left) and SEM (right) pictures of the device with eight pillars and four bottom contacts.

and then SiN (50 nm) is deposited immediately after this. The figure 3.7(b) shows actual SEM picture of the device after SiN deposition. Figure 3.9(b) shows that SiN uniformly covers the surface of the sample. Figure 3.10 shows optical picture (left) of a patterned sample and SEM picture (right) of a pillar after cross-linking and SiN deposition.

3.4.2 Opening bottom contacts

The bottom contacts are defined by electron beam lithography (EBL) using the PMMA resist. Two layers PMMA 950 K (5 %) spin-coated at 5500 rpm are used. The total thickness of the resist is $\sim$1 μm. Four rectangulars with dimensions of 2μm $\times$12μm are written by EBL (dose 750 μC/cm^2) to be used for patterning the back side contacts. After development, the SiN layer is etched by combination of CHF_3 and O_2^+ gases in a reactive ion etching (RIE) machine. We use several cycles of RIE in order to avoid teflon-like skin layers formation during RIE. Before the metalization, the sample is cleaned by Ar^+

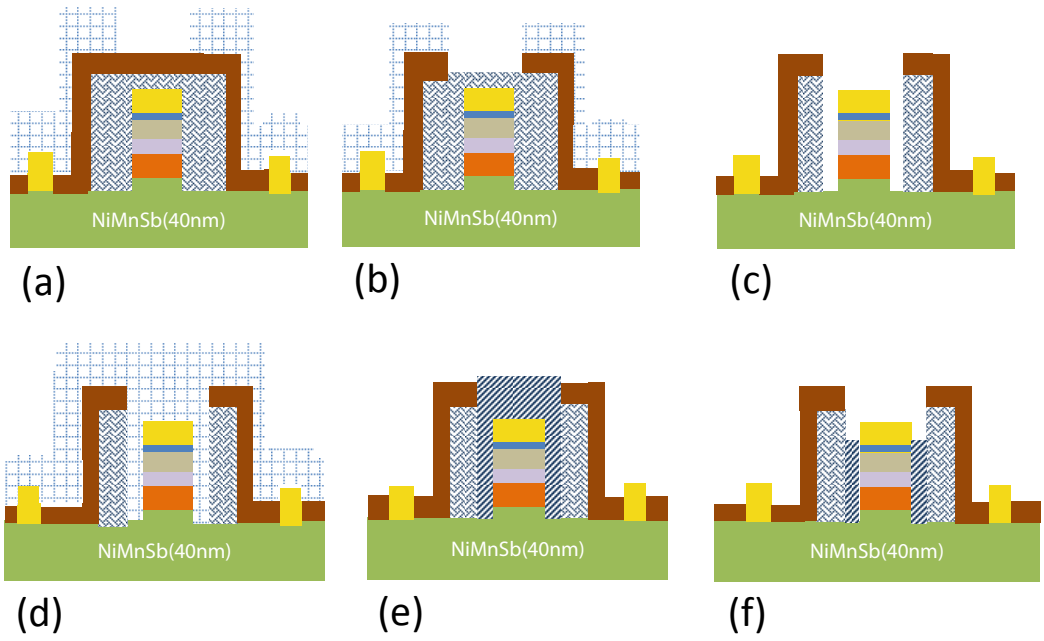

Figure 3.12: Schematic procedure of opening top contacts and second cross-linked PMMA. (a) The sample is exposed by EBL to open top of the pillar. (b) SiN layer is etched with RIE. (c) The rest of cross-linked is removed by O_2^+ plasma. (d) PMMA is spin-coated on the sample for second cross-linking. (e) The second cross-linking is done. (f) The top of the pillar is opened by O_2^+ plasma.

(for 6 seconds) IBE. Then Ti (2 nm)/Au (30 nm) layers are deposited in an evaporation machine. The resist thickness is still sufficient to perform lift-off of the evaporated metals. After lift-off open Heusler areas (bottom contacts) are covered with Ti/Au (figure 3.9(c)). Figure 3.11 shows four golden contacts of a rectangular shape which are fabricated for contacting the Heusler layer.

3.4.3 Opening top contacts of the pillar

At this stage top of the pillar is still covered with the insulators (SiN and cross-linked PMMA). Opening top contacts of the pillar is the most critical step in this process and we should monitor the device by scan electron microscopy after every etching step. We do not do simultaneous opening of bottom and top contacts both because of different dimensions and subsequent treatment.

We use the same resist which is used for opening the bottom contacts and expose an ellipse around the pillar. This ellipse is bigger than the pillar and smaller than the cross-linked PMMA. Figure 3.12(a) shows schematic picture of the pillar after electron exposure and development. After development, the RIE machine is used to etch. Similar to previous etching, etching is started by flash O_2^+ plasma. Then, SiN is etched using CHF_3 for 35 seconds. Afterwards, 30 seconds O_2^+ plasma is used to prevent the formation of teflon-layer like. This cycle is repeated three times. The rest of resist is removed in

acetone. Figure 3.12(b) shows schematic picture of the pillar after RIE. The cross-linked PMMA layer which is partly etched with CHF_3 can not be controllably etched to open a uniform contact. Often it produces non-uniform hair-like pattern which is the rest of the cross-linked PMMA (figure 3.13(a)). Therefore, the rest of the cross-linked PMMA in the opened area is renewed. The cleaning O_2^+ plasma for 10 minutes is used to etch rest of the cross-linked PMMA around the pillar. Then, one more step of the cross linking around the pillar is done similar to the previous process (figure 3.13(b)). Figures 3.12(c) and

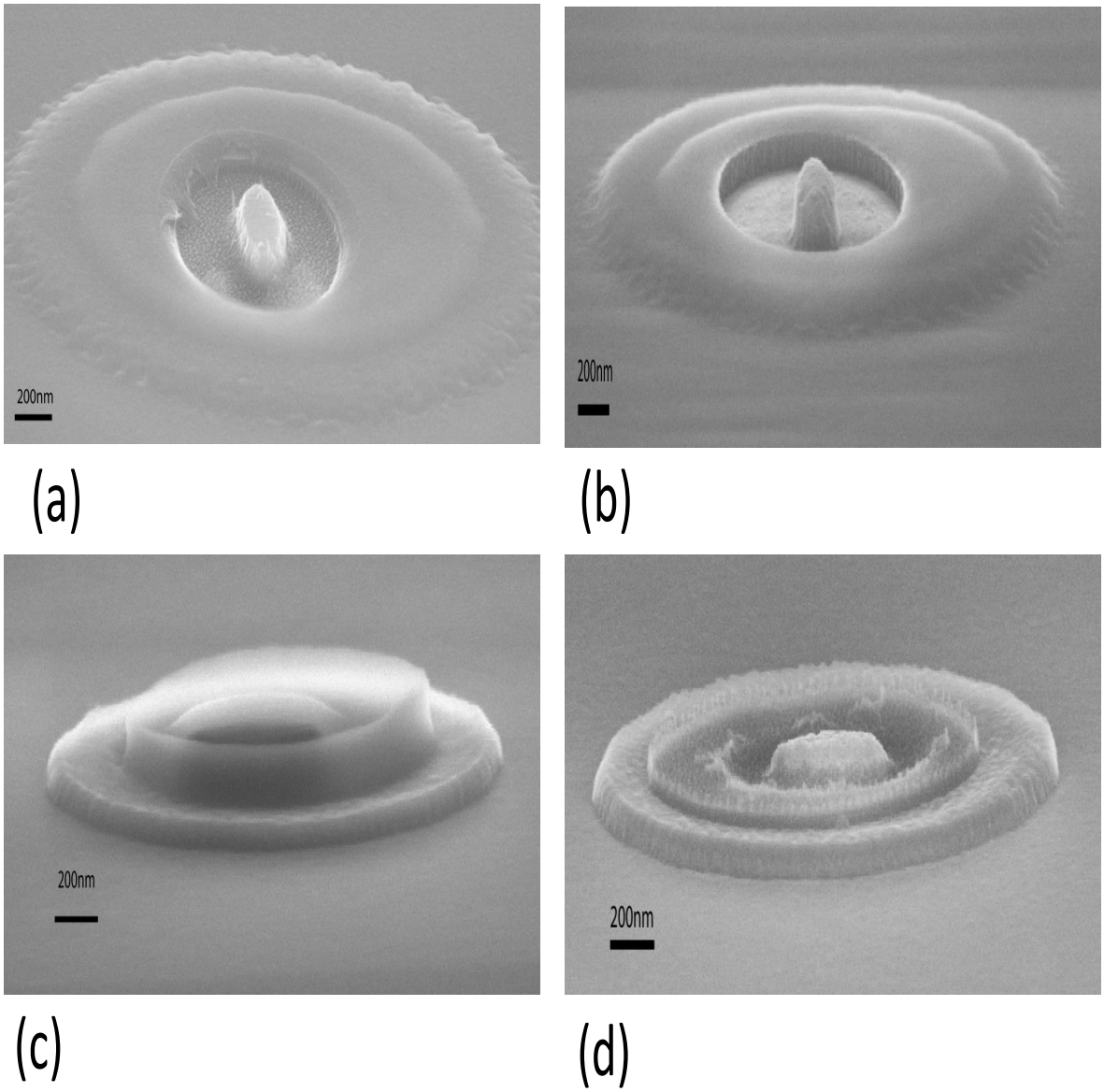

Figure 3.13: SEM pictures of actual devices. (a) SiN is etched by RIE. (b) The cross-linked PMMA around the pillar is etched away. (c) Second cross-linked PMMA is covered the pillar. (d) The second cross-linked PMMA after 20 seconds etching with O_2^+ plasma.

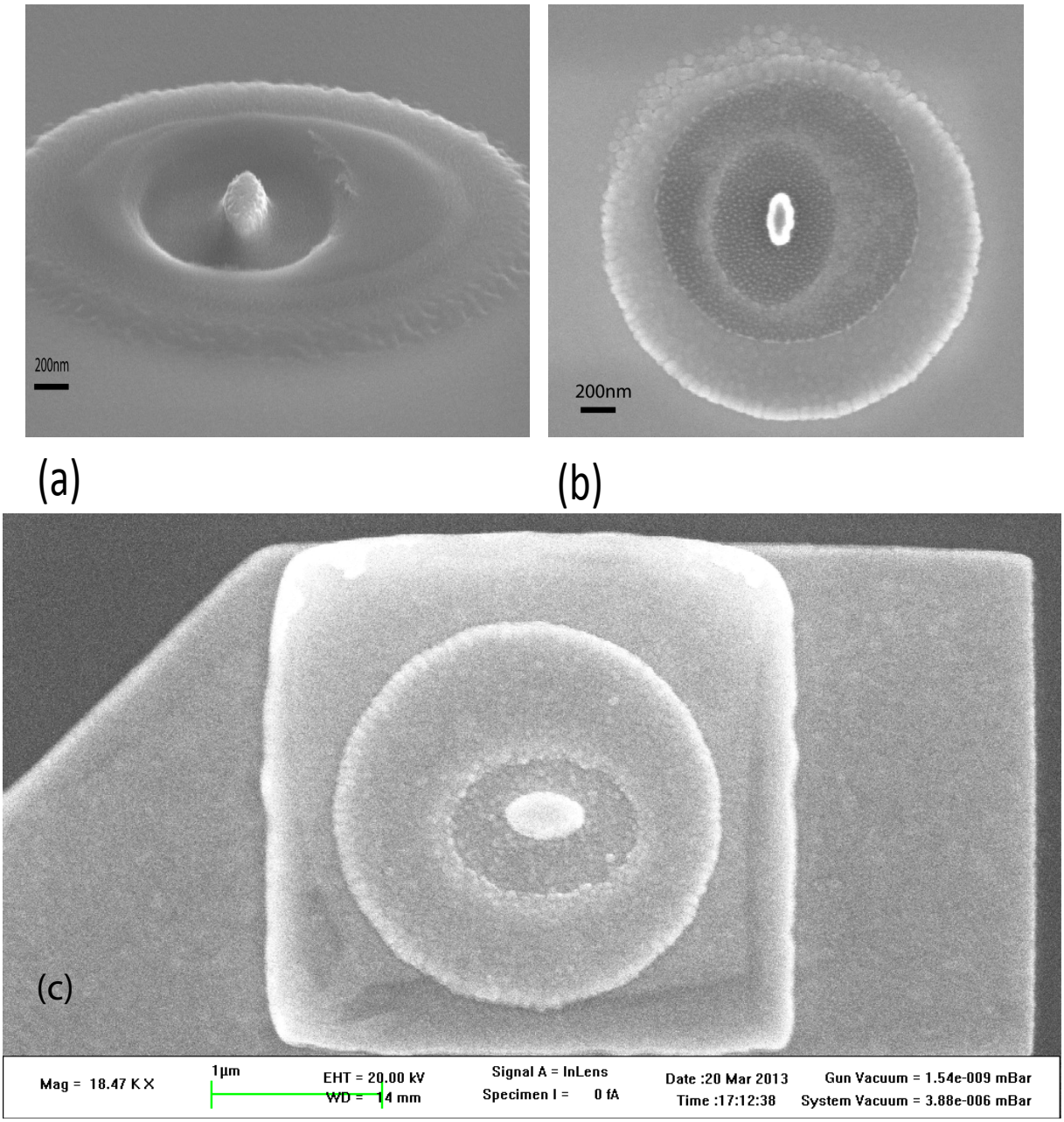

Figure 3.14: SEM picture of the pillar (a) side view, (b) top view of a fabricated pillar, (c) top view of a pillar with the gold contact on top of that.

3.13(b) show the schematic and SEM pictures of the pillar after 10 minutes O_2^+ plasma.

Figure 3.13(b) shows the pillar with the open hole. We used the second cross-linked PMMA to insulate lateral areas of the pillar. The resist which is used for this step is the same as the resist of first cross-linking. Figure 3.12(d,e) shows schematic pictures of the second cross-linked PMMA. After that, the pillar is buried under the cross-linked PMMA (figure 3.13(c)). For opening the top of the pillar, etching of the cross-linked PMMA is

started by 20 seconds O_2^+ plasma, then we monitored the opening of top Au contact with SEM. If top of the pillar is visible, this etching time is enough and top of the pillar is open. Otherwise, the etching steps are continued for 5-10 seconds until the top of the pillar is visible (figure 3.12(f)). For example, figure 3.13(d) shows one pillar after 20 seconds O_2^+ plasma. In this case the pillar is still under the cross-linked PMMA and it must etch more. Another example is shown in figure 3.14(a) this time 20 seconds O_2^+ plasma was enough and Au top of the pillar is open.

Top view of the open pillar is shown in figure 3.14(b). In this figure, the big circle around the pillar is the first cross-linked PMMA and the second one with smaller diameter is the second cross-linking. Also a third and smaller circle is visible which is due to etching of the SiN layer.

3.4.4 Connecting top and bottom of the pillars to big contact pads

For preparing the sample for measuring, top and bottom of the pillar is connected to big contacts pads via two steps of electron beam lithography. First step is the fabrication of small contact leads. The process starts by spin-coating the sample with PMMA layers. The first layer is PMMA 600 K (7 %) deposited at 5000 rpm and baked at 200 ℃ for 30 minutes. The second layer is PMMA 950 K (3 %) spin-coated at 7500 rpm and baked at 180 ℃ for 30 minutes. After performing EBL and development, a flash of O_2^+ plasma and 6 seconds Ar^+ etching are done to clean the top of the pillar, subsequently. Deposition of Ti (3 nm) and Au (70 nm) in evaporation machine and lift-off is done. Figure 3.15(a) shows small contact leads which connect eight pillars at different orientations and also four bottom contacts near the pillars. The pillars are patterned in two different orientations.

The last EBL step is done for the fabrication of big contact pads and the leads. Here also two layers of PMMA are used for the fabrication. The first and second layers are PMMA 600 K (7 %) (5000 rpm, 200 ℃ for 30 minutes) and PMMA 950 K (3 %) (6500 rpm, 150 ℃ for 30 minutes), respectively. As figure 3.15(b) shows, the small and big contact leads overlap each other. After developing and depositing Ti (5 nm) and Au (100 nm), lift-off is done and the sample is ready for bonding (figure 3.15(b)). More detailed recipe of all fabrication steps are presented in Appendix B.

Bonding of this sample is also a critical step. The process which we call glue bonding is especially invented to such sensitive samples by Philip Hartmann (Wuerzburg university). The main feature is the application of a special conducting epoxy-glue to contact wires to the big pads located on the SiN/Heusler surface. Figure 3.16 shows a glue-bonded sample.

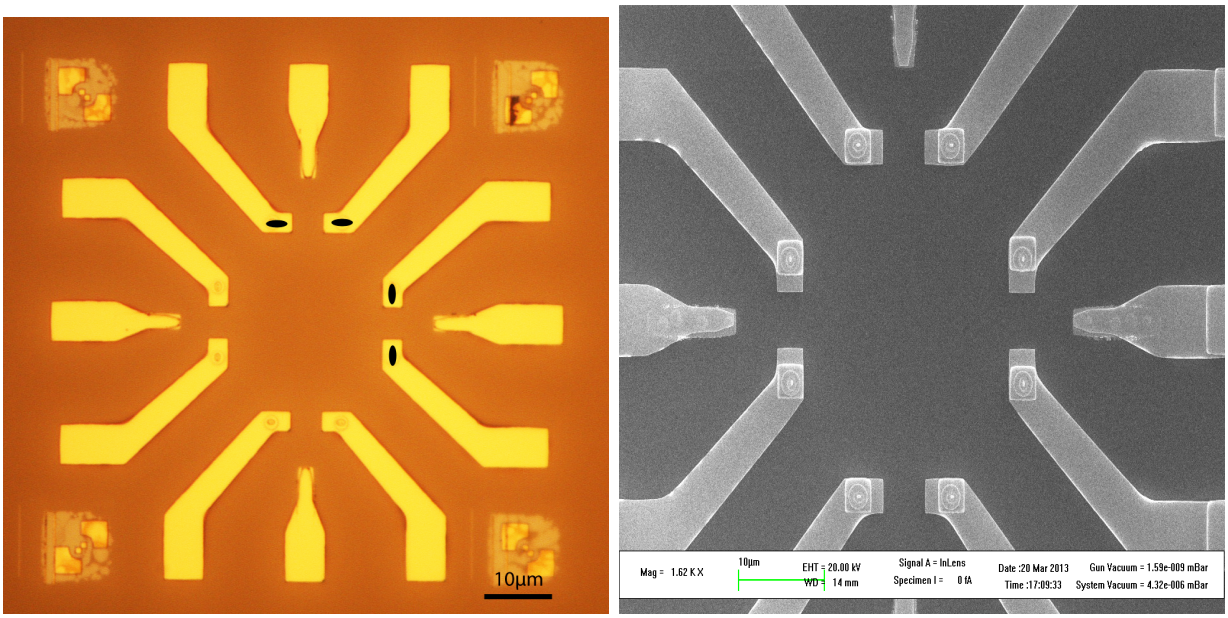

(a)

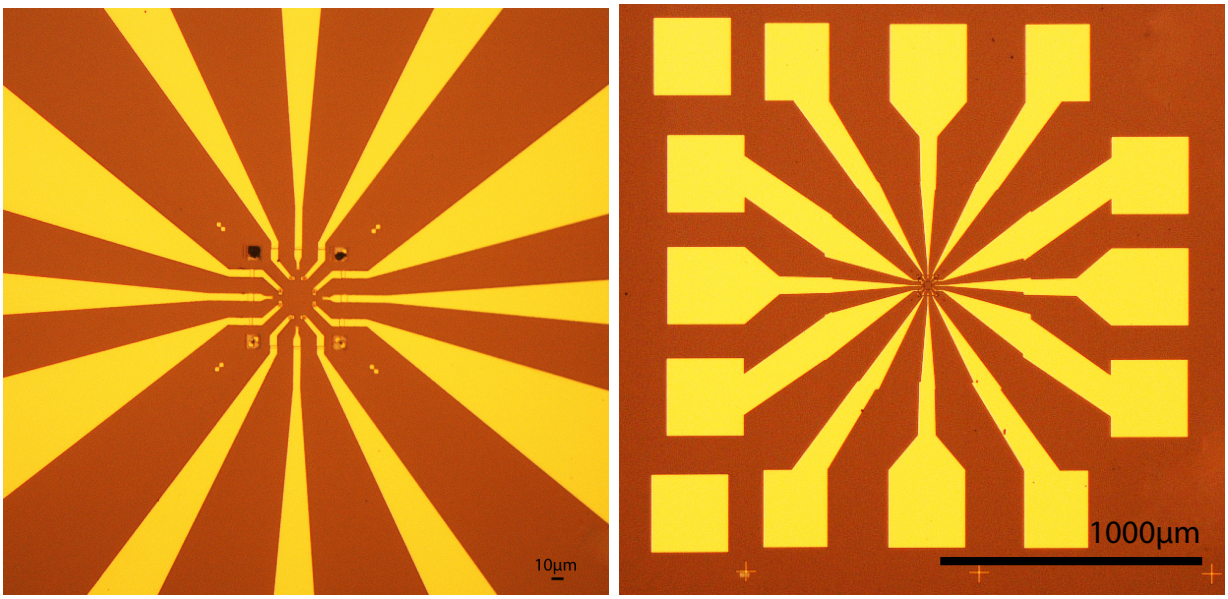

(b)

Figure 3.15: Pictures of device are taken by optical microscope. (a) The small contacts leads. (b) The big leads which overlap with small leads (left picture), and the big contact pads and final device (right).

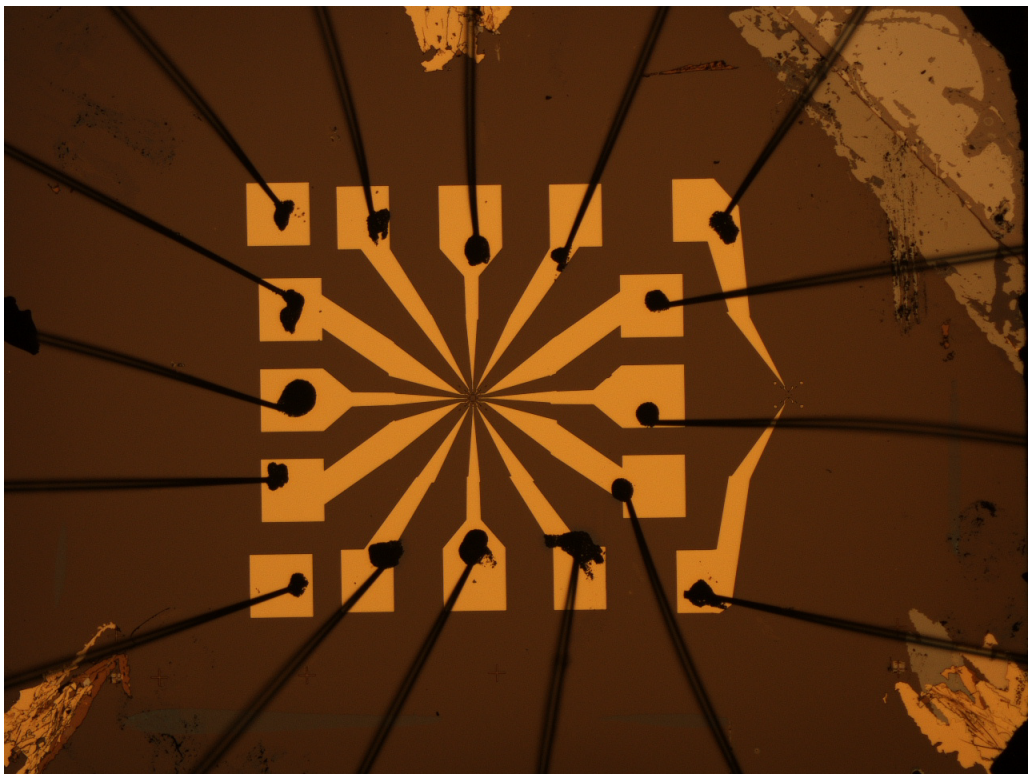

Figure 3.16: A picture of finall sample, the sample is glue-bonded to chip career.

Chapter 4

Magnetoresistance and CPP-GMR

4.1 Introduction

As discussed in chapter 1, the current-perpendicular-to-plane giant magnetoresistance (CPP-GMR) of pseudo spin-valves devices have become a key component of modern information storage technologies [Kati 08]. In this chapter the CPP magnetoresistance of a Py/Cu/NiMnSb nanopillar at various temperatures and bias currents are examined. Also, the resistivity of the NiMnSb and the (In,Ga)As layers by four probe method are measured. Finally, the effect of the shape anisotropy on the device is examined.

4.2 Electrical resistivity

In order to study the CPP-GMR devices, knowing the resistivity of the layers helps us to understand about the physics involved and to achieve a higher MR ratio for practical application [Zhi 14]. Therefore, the electrical resistivity of the NiMnSb layer and the (In,Ga)As layer are measured in this section.

4.2.1 Microfabrication of Hall-bar

The layer stack which is used for measuring the resistivity of NiMnSb and (In,Ga)As contains Ru(10 nm)/NiMnSb(40 nm)/(In,Ga)As(200 nm)/InP:Fe(360 μm). In this layer stack the substrate (InP:Fe) is an insulated layer while in the layer stack which is used for the nanopillar device the substrate layer is a semiconductor (InP:S). This substrate was chosen to be able to measure the resistivity of the NiMnSb and the (In,Ga)As layers. For measuring the resistivity of the NiMnSb and the (In,Ga)As layers, we fabricated Hall-bars by using photo lithography.

To fabricate the sample for measuring the resistivity of the NiMnSb layer, the sample is etched by Ar^+ ion beam etching at the angle of 70° to etch away the Ru layer. The milling is timed to stop after 10 nm removal of the Ru layer. Immediately after etching,

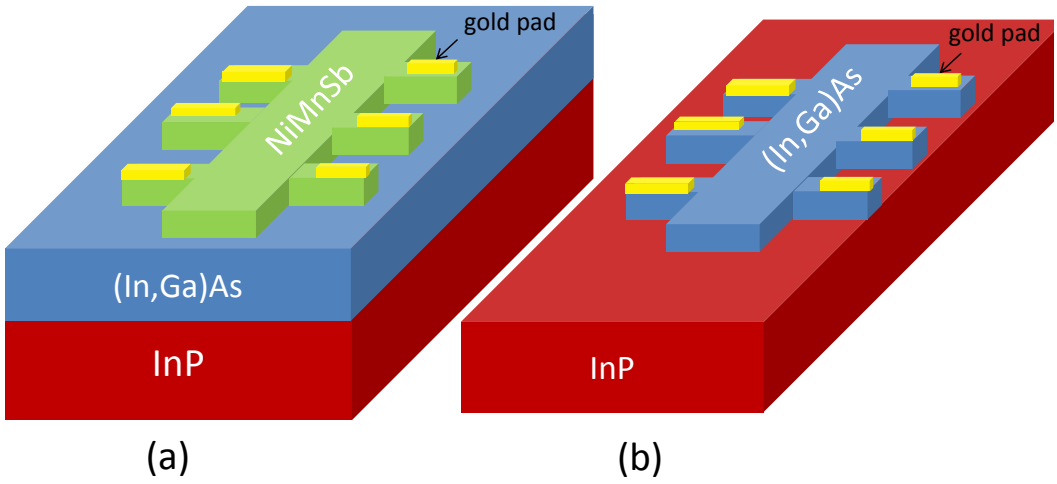

Figure 4.1: Schematic pictures of the Hall-bars. (a) The sample is prepared for measuring the resistivity of the NiMnSb layer. This layer is patterned in the Hall-bar. (b) The (In,Ga)As layer is patterned in the Hall-bar for measuring the resistivity of this layer.

the sample is covered by an optical resist to pattern the Hall-bar by optical lithography. The 40 nm NiMnSb layer is completely patterned in the Hall-bar and gold contact pads are made on top of the Hall-bar for bonding the sample. As figure 4.1(a) schematically shows, the NiMnSb layer is patterned in the Hall-bar and the (In,Ga)As layer stays unpatterned.

We measured the resistivity of the (In,Ga)As layer for better estimate of the resistivity of NiMnSb. A Hall-bar is fabricated to measure the resistance of the (In,Ga)As. The same layer stack is used to measure the resistivity of the (In,Ga)As layer. First, the Ru and the NiMnSb layers are etched away by Ar^+ iron beam etching. The Hall-bar is created out of the (In,Ga)As layer by optical lithography. Figure 4.1(b) shows schematic picture of the Hall-bar that InP:Fe is substrate of this Hall-bar.

4.2.2 Measurement of the electrical resistivity

The resistivity (electrical resistivity) of NiMnSb and (In,Ga)As are measured by four probe measurement method. Figure 4.2(a) shows an optical picture of a fabricated Hall-bar and figure 4.2(b) represents the four probe measurement setup. In this measurement, a dc current is applied between two contacts along the long axis of the Hall-bar and the voltage is measured between two next contacts.

The resistivity of a layer is defined by the following equation.

$$\rho = R\frac{\omega t}{L} \tag{4.1}$$

Where R is the electrical resistance of the thin layer. ω is width of a patterned layer (ω = 40 μm), t is thickness of the Layer (40 nm for NiMnSb and 200 nm for (In,Ga)As,

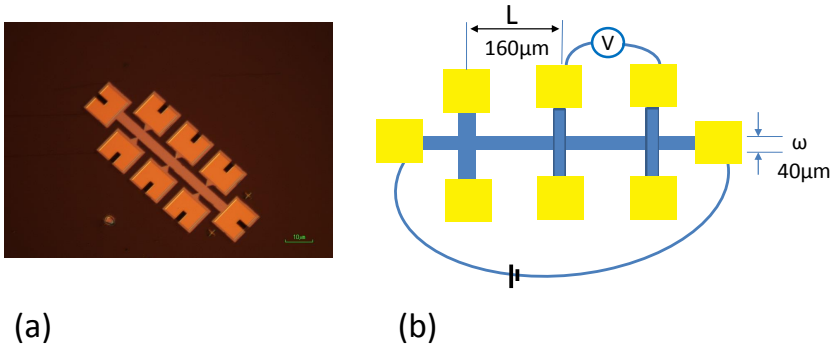

Figure 4.2: (a) A picture of a hall-bar which is fabricated by optical lithography. (b) The schematics setup of the four terminal longitudinal measurement.

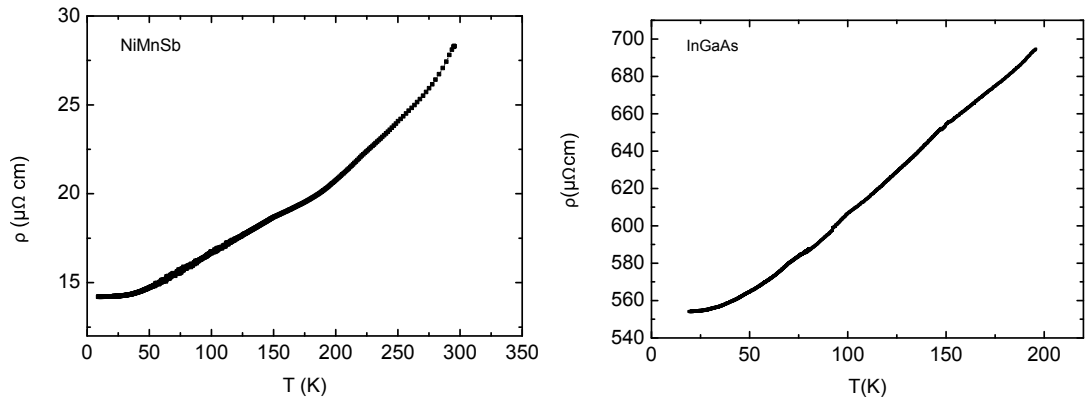

Figure 4.3: (a) The resistivity of the NiMnSb layer versus temperature. (b) The resistivity of the (In,Ga)As layer versus temperature.

respectively), then ωt is the cross-sectional areas of patterned layer. L is the length of the sample in which the voltage is measured (L = 160 μm).

Figure 4.3(a) shows the resistivity of the NiMnSb layer versus temperature. The resistivity of the NiMnSb layer is 14.2 $\mu\Omega$cm and 28.5 $\mu\Omega$cm at 4 K and 300 K, respectively. The quality of a crystal may be inferred from the residual resistivity ration (RRR)

[Raph 02] which could be calculated by ρ_{300K}/ρ_{0K}. Since, the minimum temperature that we could measure the resistivity of the sample is 4 K, then the RRR here (ρ_{300K}/ρ_{4K}) is 2. This value is bigger than the RRR for NiMnSb which is already reported (RRR = 1.65) [Ritc 03]. Generally, the bigger RRR is attributed to low degree of order [Blum 09]. In this case, we should take it into account that the NiMnSb layer is grown on the (In,Ga)As/InP layers and part of the current will flow through the substrate during the measurement (in next paragraph is explained the resistivity of the (In,Ga)As). Therefore, it is not possible to measure the resistivity of the NiMnSb layer with good accuracies due to complex current distribution in multilayer. But we can roughly estimate that actual resistivity of the NiMnSb layer must be lower than shown data. The RRR values for other half-metallic components are Co_2MnSi (RRR = 2.8) [Blum 09] and Co_2FeSi (RRR = 5.2) [Blum 09]. Furthermore, in figure 4.3(a) second derivation of ρ(T) curve is positive for high and low temperatures, but it is negative for the temperatures between 50 K and 160 K. A similar behavior is observed in other reports on the resistivity of NiMnSb [Borc 01, Ritc 03].

Figure 4.3(b) shows the resistivity of the (In,Ga)As layer versus temperature. The measured resistivity is 700 $\mu\Omega$ at 200 K. As it was expected for the CPP-GMR layer stack, this layer is conductive. It's well-known that if the CPP-GMR device doesn't have a proper underlayer with low resistivity which acts as a lead electrode, the electric current inhomogeneously flows in the pillar and it may not show any ΔR values in the CPP-GMR device.

4.3 Spin-valve

Spin-valve devices are composed of two ferromagnetic layers (FM) separated by a non-magnetic layer (NM). Some of the applications of spin-valves are in magnetic read heads, hard disk read head and magnetic random access memories (chapter 1). There are two types of spin-valves, exchange-biased spin valves and pseudo spin-valves. In the exchange-biased spin valve one of the ferromagnetic layer is pinned by an antiferromagnetic layer and the pseudo spin-valves devices have a hard and soft magnetic layer [Prof 02].

4.3.1 CPP-GMR measurement of pseudo spin-valves

The main purpose of this thesis is to study the pseudo spin-valve (PSV) devices composed of Py/Cu/NiMnSb trilayers. This section describes the CPP-GMR properties of the trilayers and chapter 5 will describe the spin torque properties of the sample.

The basic measurement scheme is shown in figure 4.4(a). We do three terminal DC measurements by applying the positive dc voltage from top of the pillar to one of the bottom contact, and the bias voltage is measured between top of the pillar and a different bottom contact. Figure 4.4(b) shows SEM image of the sample with three leads which connect the top and the bottoms of the pillar to the big contact pads. In this measurement,

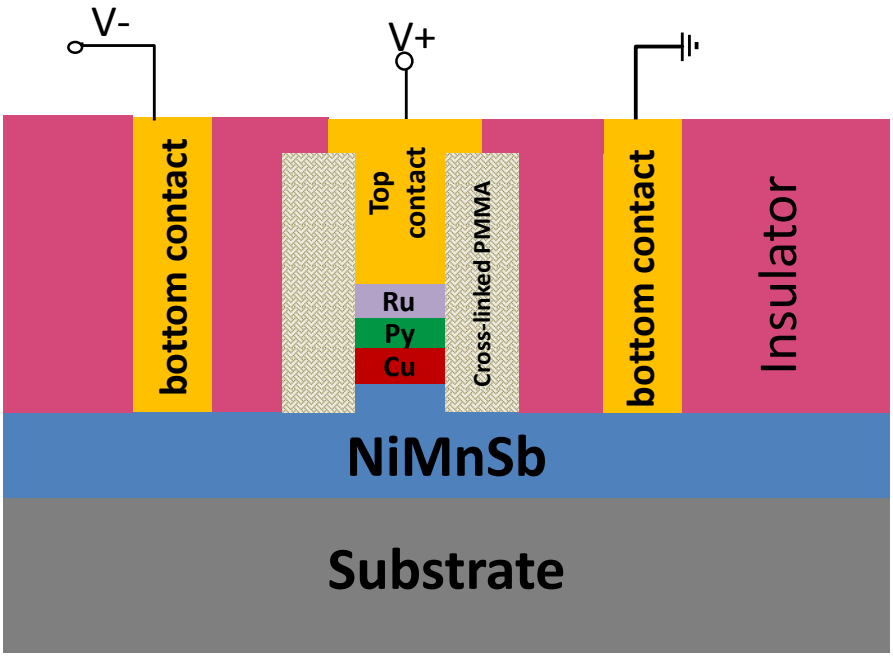

(a)

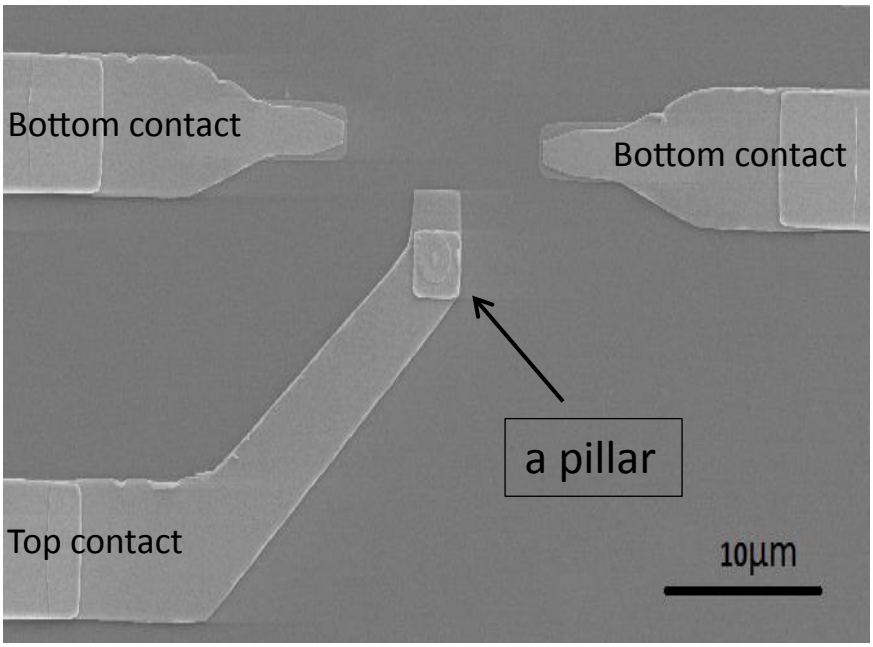

(b)

Figure 4.4: (a) Cross-sectional schematic diagram of three terminal DC measurement. The positive dc voltage is applied applied from top of the pillar to one of the bottom contact and the bias voltage is measured between top of the pillar and a different bottom contact. The electron current of the positive bias is from Py to NiMnSb and the electron flow is in the opposite direction.(b) SEM image of the sample shows the leads which connect the top and bottoms of the pillar to the big contact pads.

the electric current of the positive bias is from Py to NiMnSb and the electron flow is in the opposite direction.

4.3.2 In-plane magnetic field along the long axis of the pillar

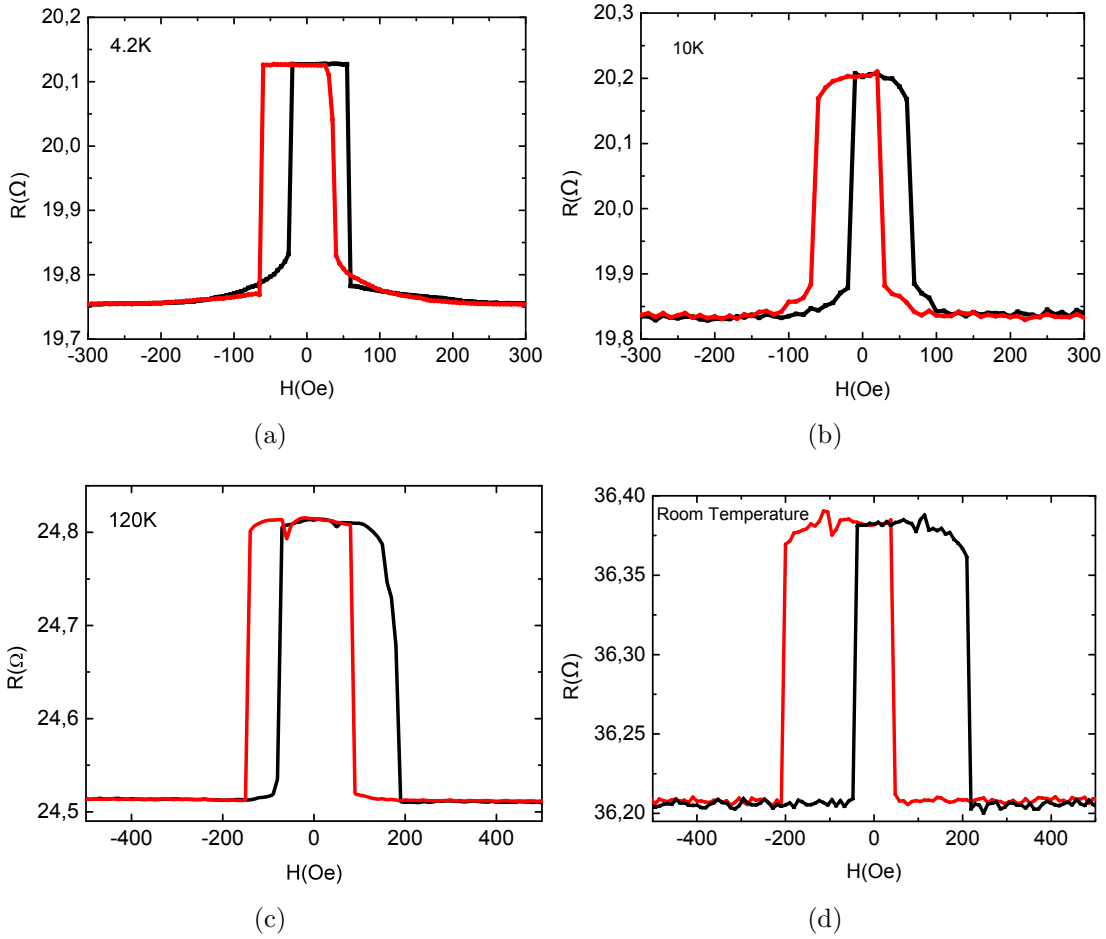

Figure 4.5: The CPP-GMR curves of the pseudo spin-valve pillar (500 nm×250 nm) measured at (a) 4.2 K, (b) 10 K, (c) 120 K and (d) room temperature. The measured resistance (R) also includes the lead resistance. In the red curves the magnetic fields swept from -500 Oe to +500 Oe and for the black curve vise versa.

Figure 4.5 shows the magnetoresistance (MR) curves of the nanopillar with dimensions of 500 nm× 250 nm versus the external in-plane applied magnetic field (H) along the long axis of the pillar for low temperatures (4.2 K and 10 K) and higher temperatures (120 K and room temperature). The resistance of the nanopillar jumps abruptly to a higher value at low field, which is the antiparallel (AP) state and then back to the parallel state at high field. As temperature increases, the resistance of the AP and P states increase and the GMR ratio decreases. By increasing the temperature the spin scattering increases and the spin scattering destroys the spin accumulation [Brat 06]. As discussed in chapter 2, the

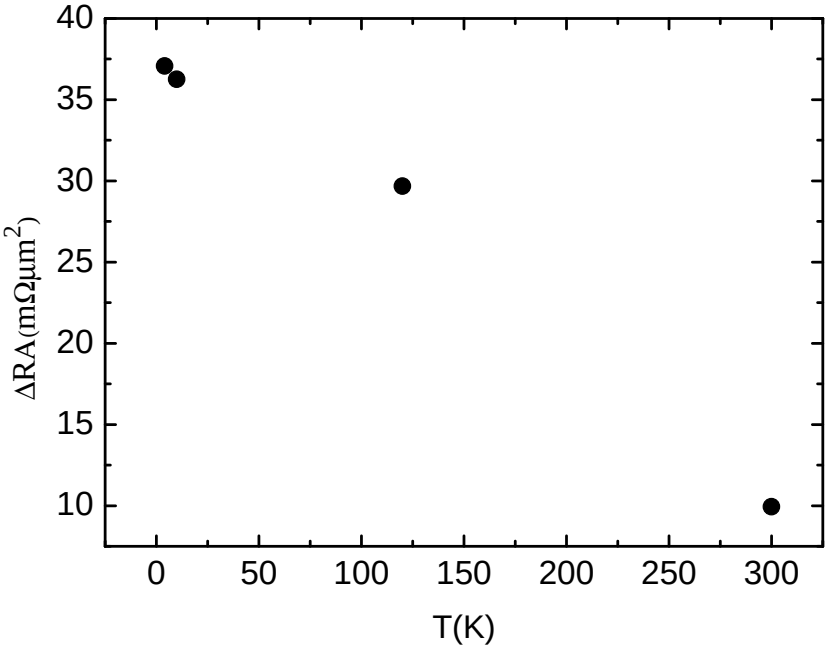

Figure 4.6: Temperature dependence of the △RA of the device.

origin of the CPP-GMR is the spin accumulation. By reduction of the spin accumulation at higher temperatures the electrochemical potential (ECP) of spin-up and spin-down electrons decreases, therefore the CPP-GMR ratio and △R decrease. Furthermore, the field in which the magnetization of the one ferromagnetic layer switches depends on the temperature, the GMR values are observed in lower magnetic field at low temperatures.

The raw data shows the difference in resistance △R of 0.30 Ω (1.3 %) and 0.17 Ω (0.5 %) at 120 K and room temperature, respectively and at low temperatures △R is ∼ 0.37 Ω (1.87 %). Note that because the three terminal measurement includes one lead resistance, the actual MR ratios are higher than the numbers given above.

The dependence of △RA on the temperature is shown on figure 4.6. The △R decreases with increasing the temperature. The spin-flip scattering is one of factors that effects the temperature dependence of the GMR. It means that the interface spin fluctuations increases the temperature dependence of the GMR. For example in Fe/Cr superlattices, rough interfaces enhance fluctuations and a strong temperature dependence is observed [Baib 88] [Pate 11], whereas for Co/Cu multilayer a weaker variation of the GMR with temperature is reported, because it has smoother interface structures [Park 91]. "The weaker temperature dependence for Co/Cu compared to Fe/Cr is consistent with smaller spin-flip scattering in Cu than in Cr layers"[Park 91]. Therefore, Cu as spacer is a good candidate for spin-valve devices.

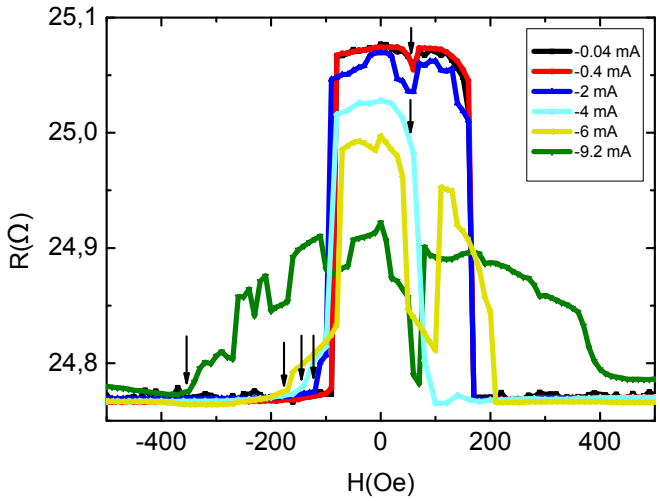

(a)

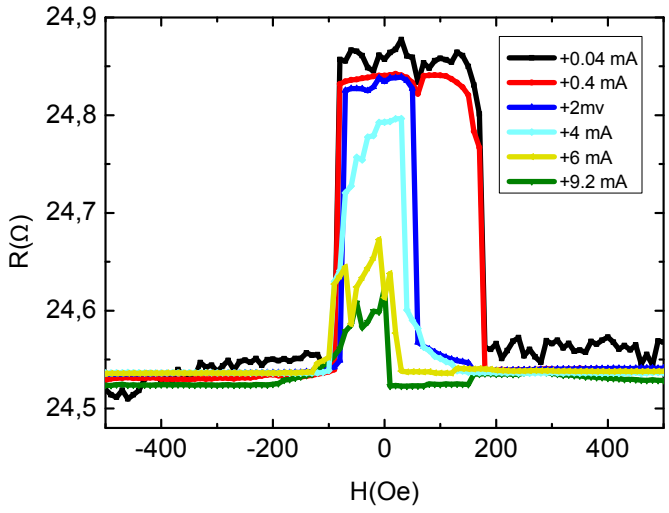

(b)

Figure 4.7: The MR curves with various bias currents of the pillar. The device area is A=0.098 μm^2. (a) The electron flow direction is from Py (free layer) to NiMnSb (pin layer). The arrows indicate the switching from P state to AP state. (b) The electron flow is from NiMnSb to Py.

4.4 Current dependence of CPP-GMR

Most of the data presented in the rest of this thesis are taken at 120 K because this allows us to provide much quieter noise environment and access to a superconducting vector-field magnet, allowing for much more accurate measurements. Also, although the amplitude of the magnetoresistance difference ($\triangle$R) at room temperature is smaller than at 120 K (figure 4.5) the phenomenology of the sample is similar at room temperature and 120 K.

In this part of thesis, effect of the current on the CPP-GMR is measured to explore role of the spin-transfer torque on the sample. In the multilayers the electron flow from one ferromagnetic layer applies a spin torque on the other ferromagnetic layer (chapter 2). This spin torque can oppose the intrinsic damping of the magnetic layer, exciting spin waves and for a sufficient current strength reverses the direction of the magnetization [Myer 99] and [Mang 06]. By applying the various bias currents to the CPP-GMR device, we can not exactly investigate the spin-transfer torque induce reversal but we can estimate role of the spin torque by destabilizing of the ferromagnetic layers by the bias current. Also, the spin-transfer torque reduces the CPP-GMR output ($\triangle$R) and causes a deterioration of the spin-valves signal [Covi 04][Zhu 04].

The electron flow through the pillar not only generates the spin torque but also induces an Oersted field (induced magnetic field) and Joule heating. The Oersted field is vortex-like induced magnetic field which is generated by the current flow perpendicular to the pillar. The Oersted field in the pillar increases with increase in distance from center of the pillar, and it is the strongest at the edge of the pillar and zero at the center. At our current density (10^6 A/cm^2), the Oersted field has a maximum value of 10 Oe [Acre 06, Megu 08]. The Oersted field decreases $\triangle$R by degrading the magnetization configuration at the edge of the pillar [Tomo 11].

With the purpose of analyze the effects of these three phenomenon, different MR curves are measured for two current directions and also for different current strengths. The actual dimension of the pillar is 500 nm $\times$ 250 nm (A = 0.098 μm^2). Figure 4.7 shows the MR curves of the pillar with various bias currents. In this figure the external field swept from negative to positive. In figure 4.7, the shape of the MR curves change for the various values of the electron currents and the different signs. Moreover, the effect of the Oersted field should not depend on the current polarity. Thus, the change of the MR curve in figure 4.7 may not be due to the induced field [Naka 12].

Next concern is whether the reduction of $\triangle$R is due to the Joule heating or not. By increasing the current, the Joule heating increases the temperature of the pillar ($\sim$ 10 K). Therefore, the $\triangle$R decreases and the resistance of the device increases by increasing the temperature. However, the increase of temperature should decrease the coercivity of the magnetic layers and increase the spin-dependence of the scattering, which induce a change of the switching field of the free and pinned layers and a reduction of $\triangle$R, but it is unlike that the irregular change of the resistance by the sense currents which is shown in figure 4.7 is attributed to the Joule heating. Consequently, the changing in the MR

curve by applying different magnitudes and sign of currents (figure 4.7) can be explained by the spin torque.

In figure 4.7(a) the bias current is negative which means the electron flow is from Py to NiMnSb (figure 4.4(a)). In the low bias currents (from 0.04 mA to 0.4 mA), the MR curve does not show any changes, because the spin-transfer torque is not strong enough to change the MR. By increasing the bias current from 0.4 mA to 9.2 mA, the parallel state (lower resistance) is destabilized which is shown by black arrows in figure 4.7(a). This is due to the spin torque of the reflected electrons from the fix layer (NiMnSb). The role of the spin torque is more obvious in higher bias currents. Also, the switching fields from the parallel (P) to the antiparallel (AP) states become larger in the negative fields with increasing the bias current from -2 mA. At -4 mA, the MR curve shows an extra dropping to the lower resistance at 70 Oe and again it increases to the higher resistance at around 80 Oe. This means that the pillar is in intermediate state and both antiparallel and parallel states are stable in these magnetic fields. The same behavior at $\sim$ 70 Oe is observed in the lower bias current which is pointed by arrows, but no switching to the lower resistance is observed. Because of the low bias current, the spin torque can not succeed to the external magnetic field. For better understanding of the spin torque, we investigate the spin-transfer torque induces switching in next chapter (chapter 5).

In figure 4.7(b) the MR curve is plotted for the various positive bias currents. For the positive current the electron flow is from the NiMnSb layer (fix/pin layer) to Py layer (free layer) (figure 4.4(a)). In this current direction, the spin torque tends to align the magnetization of two layers parallel. Therefore, parallel state is stable configuration of the pillar. As we see in the figure 4.7(b) increasing the bias current destabilize the antiparallel state (higher resistance). At the low currents the pillar show a plateau from -90 Oe to 180 Oe in which the sample is in the antiparallel state. When the current increases this plateau collapses. When +2 mA is applied to the sample a change in the resistance of the sample in the antiparallel state is observed. This again proves that the spin torque destabilizes the antiparallel state by flowing electrons from the PL to FL.

4.5 Shape anisotropy of CPP-GMR spin-valves

To investigate other magnetic properties on the same multilayer, the magnetoresistance of the pillar as a function of the in-plane magnetic field at different angles is examined. Figure 4.8 shows the MR curves of the nanopillar versus the in-plane magnetic field for three angles of $\Phi = 0°$, $45°$, $90°$ at 120 K. Φ means the angle of the external in-plain magnetic field relative to the long axis of the pillar. In figure 4.8 the external magnetic field is swept from -1000 Oe to 1000 Oe. Green curve shows $\Phi = 90°$ which is along the short axis of the pillar and black curve ($\Phi = 0°$) is along the long axis of the pillar. A large difference in shape of the MR curves for two different angles of $\Phi = 0°$ and $\Phi = 90°$ is observed, which with respect to the device dimension is “shape anisotropy”.

Due to demagnetizing field in patterned thin film, the magnetization has the easy axis along the long diameter of the pillar and the hard axis along the short diameter. "Bell-shaped" MR curve is observed at $\Phi = 90°$ (green curve). In the green curve the resistance of the pillar gradually increases with increasing H towards zero. The reason is that the magnetic configuration of both layers rotate in the opposite directions towards the long axis of the pillar. When H is zero, the two ferromagnetic layers relax in the opposite directions towards the easy axis of the pillar and the resistance is maximum at this point. By increasing H the magnetoresistance decreases symmetrically and the magnetization of both layers are parallel along the short axis of the pillar at the saturated field. A schematic picture of the magnetization configurations of both ferromagnet layers when H is parallel with the short axis of the pillar is shown with dot and solid green arrows in

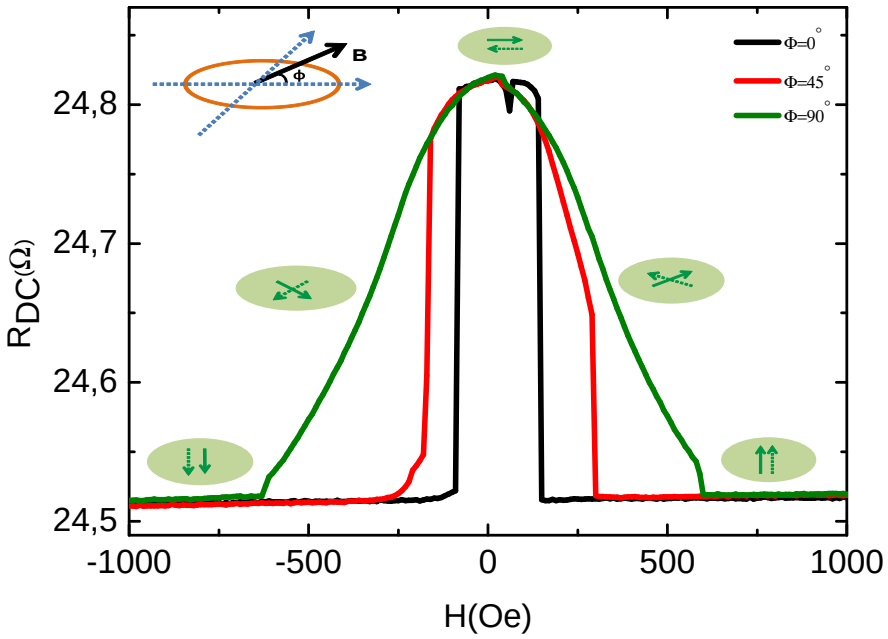

Figure 4.8: The MR curve of the nanopillar versus in-plane magnetic field for three different angles (Φ=0°,45°,90°) relative to long axis of the pillar at 120 K (the bias current is 0.4 mA). The dot and solid green arrows in small green ellipses show the magnetic configurations of both ferromagnetic layers. With increasing H form -1000 Oe towards zero, the magnetic configurations of both layers rotate in the opposite directions towards the long axis of the pillar and the resistance of the pillar gradually increases. When H is zero, the two ferromagnetic layers relax in the opposite directions towards the easy axis of the pillar and the resistance is maximum at this point. By increasing H towards 1000 Oe the magnetoresistance decreases symmetrically and the magnetization of both layers are parallel along the short axis of the pillar at the saturated field. The red curve ($\Phi = 45°$) clearly shows an intermediate state.

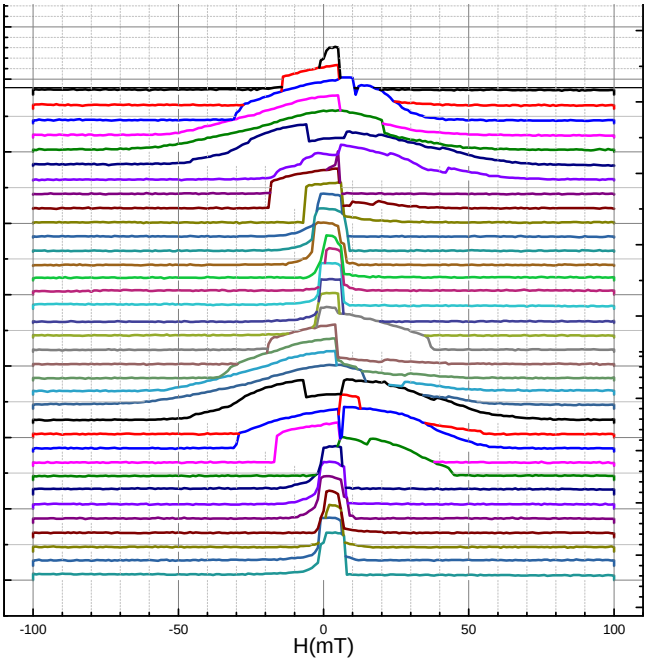

Figure 4.9: The 2D waterfall of on complete period of measurement from $\Phi = 0°$ to $360°$ an interval of $10°$. The measurement is reproducible and sharp switching is observed when the magnetic is along the lone axis of the pillar.

the small ellipses. Figure 4.8 also shows the MR curve of the pillar when the angle of the magnetic field with long axis of the pillar is $\Phi = 45°$ (red curve). This curve clearly shows an intermediate state between $\Phi = 0°$ and $90°$.

Two dimensions (2D) waterfall graph of the resistance of the pillar versus the external magnetic field for every $\delta\Phi = 10°$ is plotted. Figure 4.9 is this 2D waterfall of on complete period of the measurement ($\Phi = [0\ ,\ 360]$, $\delta\Phi = 10°$) which clearly shows that the measurements are reproducible.

Chapter 5

Spin-transfer torque switching

5.1 Introduction

Since several years, devices allowing for spin manipulation in ferromagnetic layers are the subject of intensive research [Ralp 08]. A pillar with sub-micrometer dimensions fabricated from a stack of various materials containing two or more ferromagnetic layers separated with a spacer very often serves as a core of devices suitable for investigation of spin torque phenomena [Sami 14]. As explained in chapter 2, the spin-transfer torque is more effective in devices with small cross sections such as nano-pillars.

Spin polarized current can induce a hysteretic switching or precession of magnetization on the free layer (chapter 2). The spin torque induced switching can be monitored by voltage measurement [Bass 99]. In this type of the measurement, the external magnetic field is applied along the easy axis of the free layer (long axis of the pillar) and the voltage drop along the pillar is measured as a function of the applied current density (J). It has been shown that for different values of the external magnetic field, the magnetization of the free layer exhibits different types of stable precession as a function of J [Ripp 04, Kise 03, Covi 04, Kriv 04]. This conclusion is based on the experimental observation of narrow band microwave emission combined with calculations based on generalized LLG equations which predict precession of the free layer. Other observed dynamic behavior is the telegraph noise which can be interpreted as the rapid switching between two distinct states of magnetization [Pufa 04a, Myer 02, Kriv 04].

As discussed in chapter 2, the spin torque devices work with high current densities (between 10^6 A/cm^2 and 10^8 A/cm^2). These are at the same order of magnitude as the currents in which spin-torque induced magnetic excitations are observed [Deac 06]. Such effects can generate noise and influence the biasing of the magnetic heads, therefore it is important to study them in order to control their influence [Deac 06]. The main purpose of this chapter is to investigate the stability of our device and measure the current induced switching. Most of the data presented in this chapter are taken at 120 K because this allows us to provide a much quieter noise environment, and access to a superconducting

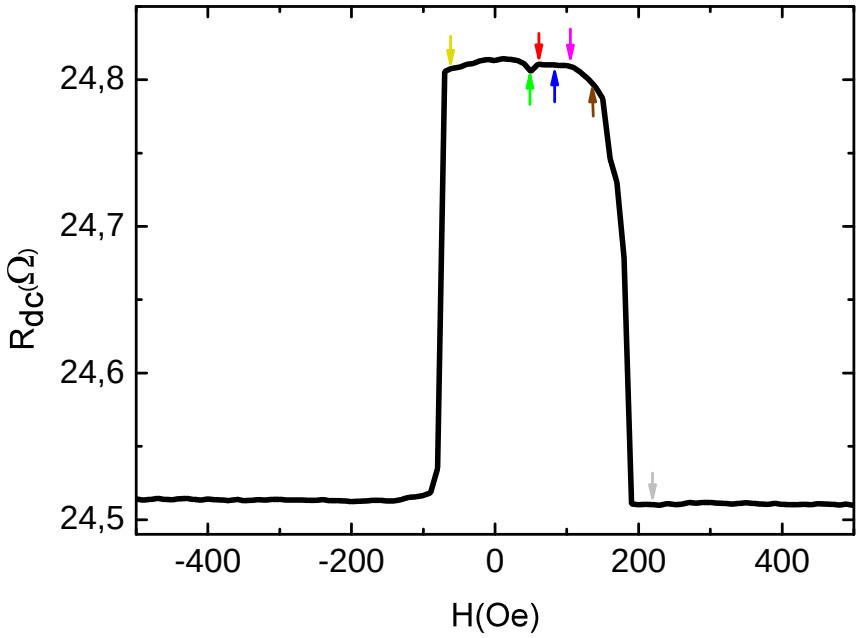

Figure 5.1: The magnetoresistance of the pillar versus the external in-plane magnetic field at 120K. The colored arrows show the different magnetic values in which the current induced spin-transfer torque measurements are done.

vector-field magnet, allowing for much more accurate measurements. In addition to that, the phenomenology as well as the switching currents are similar at room temperature and 120 K. The same device as in chapter 4 is used to investigate the magnetic stability of the system by measuring the resistance of the pillar versus the bias current in different in-plane applied magnetic fields. In these measurements four regions can be identified: one regimes where both states (P and AP) are stable, one region where only the P state is stable, one regime where only the AP state is stable and one regime where neither state is stable.

5.2 Stable P and AP states

5.2.1 Measurements at 120 K

A schematic picture of three terminal DC measurement is shown in figure 4.4. As mentioned in chapter 4, the positive dc current means that the electron flow is from NiMnSb to Py. For the first measurement, the external magnetic field (H) is ramped to -500 Oe to saturate the pillar and then swept slowly to 50 Oe where the pillar is in AP state

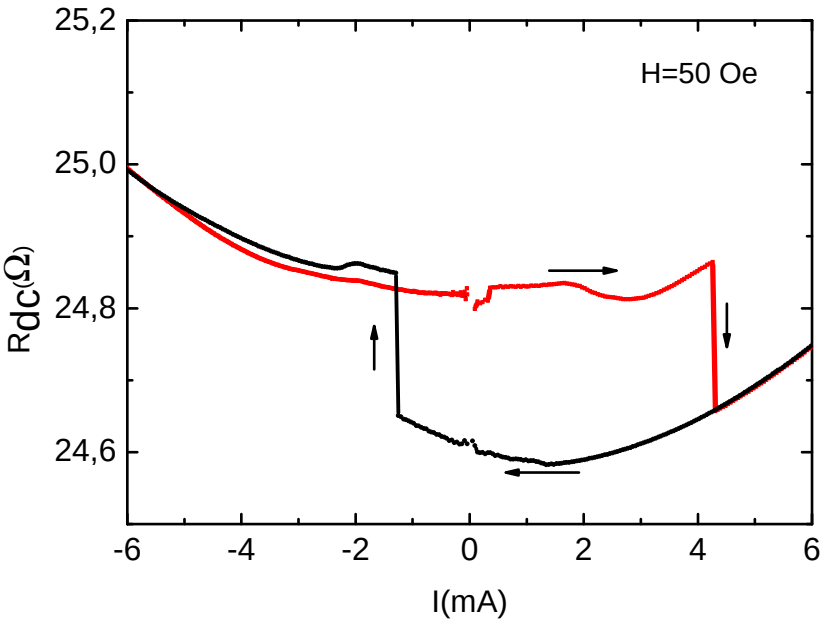

Figure 5.2: The resistance of the pillar versus the bias current while the in-plane magnetic field is kept at 50 Oe at 120 K. The data points around I = 0 mA are deleted.

(green arrow in figure 5.1). The H is kept unchanged through out the measurement. In this magnetic field (50 Oe), the measurement is carried out by sweeping the dc current in one complete cycle (0 → +10 mA → -10 mA→ 0) and monitoring the resistance of the pillar. Figure 5.2 shows the resistance of the pillar versus the injected dc current. In this measurement some data points around zero are deleted since these arise from offset of the setup. When the current increases to the positive values, the electrons become spin polarized by transmission through the NiMnSb layer and mostly maintain their polarization as they pass through the non-magnetic spacer (Cu layer). There is a transfer of the angular momentum from the polarized electrons to the magnetization of the free-layer (Py) which can be described as an effective torque. This spin torque can oppose the intrinsic damping of the magnetic layer, excite spin waves and for sufficient current strengths can reverse the direction of the magnetization [Mang 06][Brat 12] (chapter 2). In this magnetic field (50 Oe), the magnetization of the free layer (Py) is reversed by the spin momentum transfer to the parallel configuration (lower resistance) at $I_{AP\rightarrow P}$ = 4.25 mA ($J_{AP\rightarrow P}$ = 4.35×10^6A/cm^2). By increasing the current further, heat is generated by the current causing a parabolic increase in the resistance. But the pillar stays in the parallel state until the current is positive. In the negative current the electron flow is from the free layer (Py) to the NiMnSb layer. The polarized electrons reflected from the NiMnSb layer cause the pillar to switch to the antiparallel configuration [Heid 01].

Abrupt switching to a higher resistance is observed in figure 5.2 at $I_{P\rightarrow AP}$ = -1.26 mA ($J_{P\rightarrow AP}$ = -1.29×10^6 A/cm^2). Two critical currents with the opposite sign prove that AP and P states are stable at 50 Oe. The fact that ΔR ($\sim$ 0.3 Ω) measured in this measurement is comparable to the ΔR from GMR measurement (figure 4.5(c)) implies that the magnetization is fully reversed by spin-polarized current. The asymmetry observed between two critical currents, is the "signature"of the spin-transfer torque [Wain 00] and is in agreement with Slonczewski and Berger's spin transfer model [Slon 96] [Berg 96]. Furthermore, the resistance versus the current is hysteretic, and this device can function as a non-volatile spin-transfer torque magnetic random access memory (STT-MRAM).

Figure 5.3 shows the result of the similar measurements which are done at 60 Oe and 80 Oe. Here also prior to the measurements, the pillar is saturated at -500 Oe. These magnetic fields are shown with the red arrow (60 Oe) and the blue arrow (80 Oe) in figure 5.1. In figure 5.3(a) the magnetization reversal to the parallel configuration is observed at $I_{AP\rightarrow P}$ = 4.26 mA with ΔR $\sim$ 0.3 Ω. The switching from the P to AP states is at $I_{P\rightarrow AP}$ = -1.47 mA. As yet, the ΔR measured at 50 Oe and 60 Oe are the same.

In figure 5.3(b), the critical current of AP to P is $I_{AP\rightarrow P}$ = 4.32 mA. Comparing this value to the last two measurement values it is clear that the $I_{AP\rightarrow P}$ gradually decreases by increasing the magnetic field. In the negative current, switching from parallel to antiparallel is observed in two steps. A first one is at -1.75 mA and the second one is at -2.60 mA. This behavior shows the possibility of an intermediate state. The similar behavior is observed in the current dependence of CPP-GMR (figure 4.7(a)). The ΔR is 0.23 Ω which is lower than ΔR in 50 Oe and 60 Oe which means that at this magnetic field (80 Oe), the spin torque is not able to switch the magnetization of the free layer completely.

Figure 5.4(a) shows the resistance of the pillar versus the bias current at 100 Oe magnetic field (pink arrow in figure 5.1). The critical current from AP to P is $I_{AP\rightarrow P}$ = 3.70 mA and △R = 0.22 Ω. The pillar switches to antiparallel state at $I_{P\rightarrow AP}$ = -3.79 mA which is shown by black arrow in figure 5.4(a). The difference in the resistance from P to AP is △R = 4 mΩ which is much lower than △R from AP to P. This difference in resistance for P shows that the pillar tends to stay in the parallel state and the spin torque effect in reversing the magnetization of the free layer is decreasing with the increase in external magnetic field.

Figure 5.4(b) shows the resistance of the pillar versus the bias current while the magnetic field is kept at 140 Oe. As shows in figure 5.1 (brown arrow) the pillar is still in antiparallel state in this magnetic field. The $I_{AP\rightarrow P}$ = 2.68 mA and 3.11 mA which are lower than $I_{AP\rightarrow P}$ at H = 100 Oe. The $I_{P\rightarrow AP}$ = -5.76 mA and the different in resistance (△R) is very small. According to figurers 5.4(a)(b) by increasing the magnetic field, the effect of the spin-transfer torque on the reversal of the magnetization from P to AP decreases and the antiparallel state is getting destabilized.

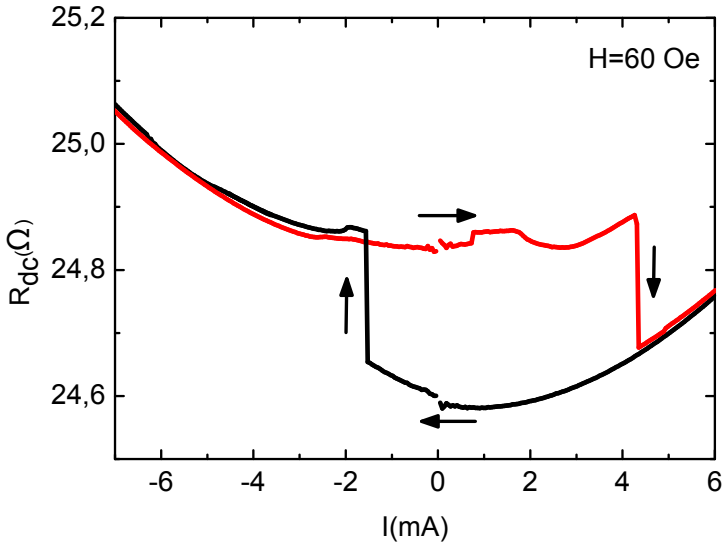

(a)

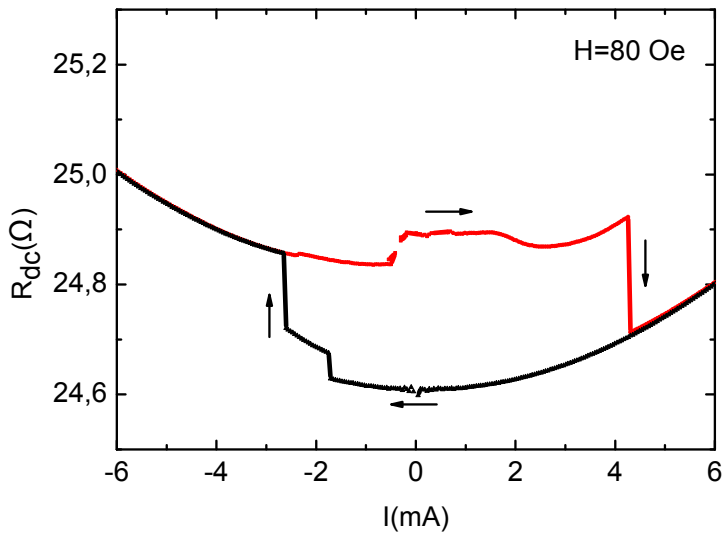

(b)

Figure 5.3: The resistance of the pillar versus the bias current at 120K. (a) The magnetic field is at 60 Oe. (b) The magnetic field is at 80 Oe. The data points around I = 0 mA are deleted

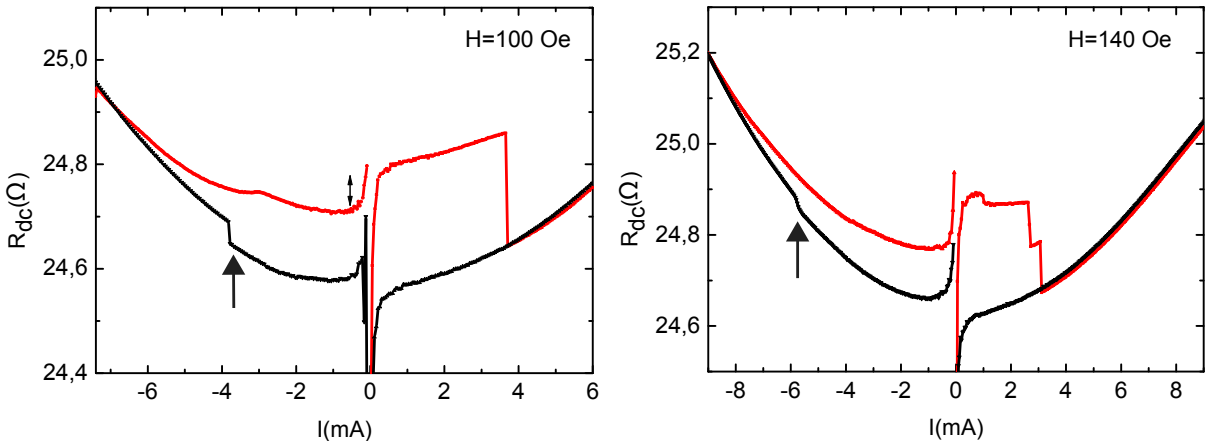

(a) (b)

Figure 5.4: The resistance of the pillar versus the bias current at 120K. (a) 100 Oe. (b) 140 Oe.

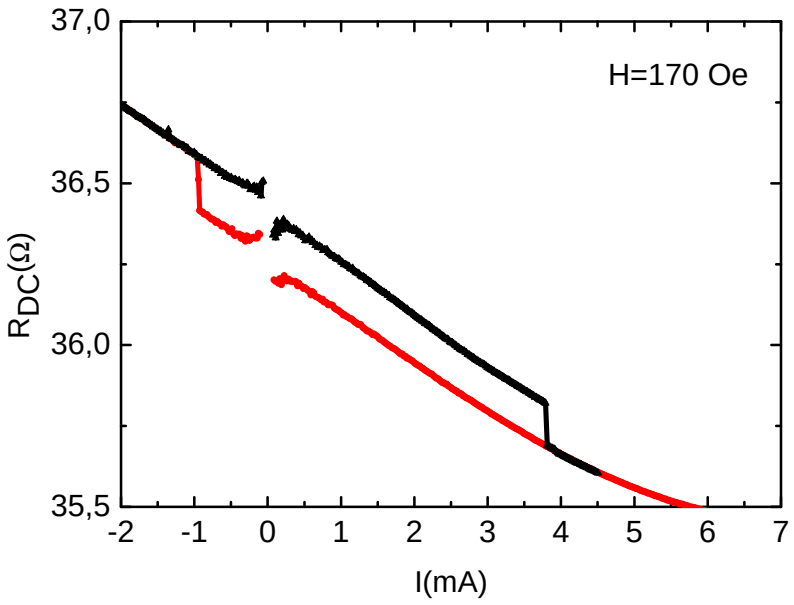

Figure 5.5: The resistance of the pillar versus the bias current at room temperature while the external magnetic field is kept at 170 Oe. The data points around I = 0 mA are deleted.

5.2.2 Measurement at room temperature

The same sample is measured at room temperature to show that the phenomenology as well as the switching currents are similar at 120 K and room temperature. Figure 5.5 shows the magnetoresistance of the same sample versus the bias current while the pillar

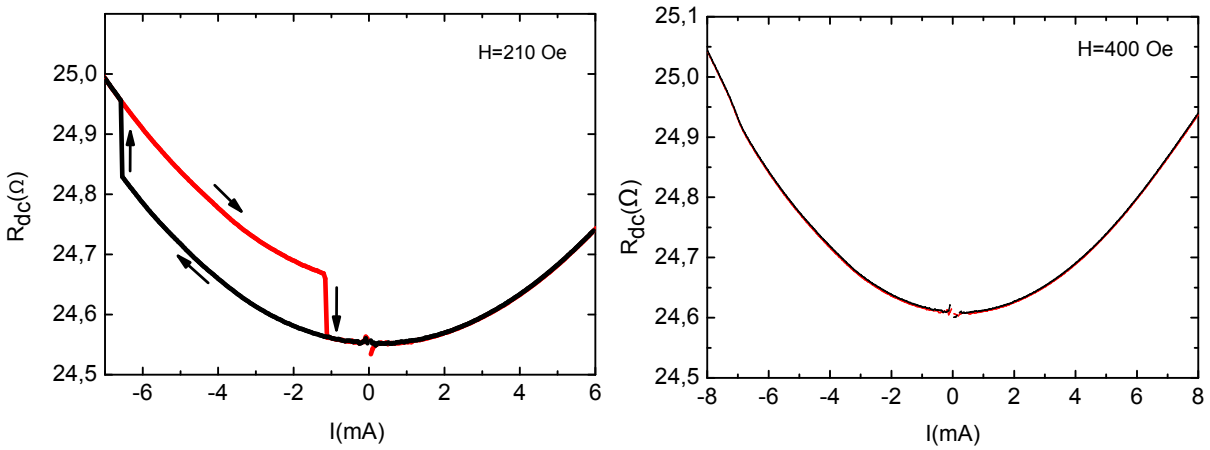

(a) (b)

Figure 5.6: The resistance of the pillar versus the bias current at 120 K. (a) The magnetic field is at 210 Oe. (b) The H is at 140 Oe, the curve is asymmetric with applied current because of the combination of the Joule heating and The Peltier effect. The data points around I = 0 mA are deleted.

is saturated at -500 Oe and swept to 170 Oe. According to figure 4.5(d) the pillar is in antiparallel state in this magnetic field. The $I_{AP\rightarrow P}$ = 3.81 mA ($J_{AP\rightarrow P}$ = 3.88×10^6 A/cm^2) and $I_{P\rightarrow AP}$ = -0.94 ($J_{P\rightarrow AP}$ = -9.6×10^7 A/cm^2) which are in the same order of the critical currents at 120 K (figure 5.2). In figure 5.5 the $\triangle$R = 0.14 Ω which is also comparable to the $\triangle$R from GMR at room temperature (figure 4.5(d)). Higher spin-dependent scattering at room temperature causes higher resistance and lower $\triangle$R as compared to 120 K.

So at this magnetic field, the parallel and antiparallel states are stable and two clear current switchings are observed. One of the reasons for such law critical current densities is the high spin polarization of NiMnSb and low Gilbert damping of Py and NiMnSb. The damping of Py is 6×10^{-3} [Koba 09] and the damping of NiMnSb is in order of 4.7×10^{-3} [Rieg 11]. Another reason comes from the new method of fabrication. As compared to the current densities observed at room temperature in the same multilayer fabricated with old fabrication method [Rieg 11], this current density is 10 times lower which shows the effect of fabrication method on the performance of the pillar (chapter 3).

5.3 Stable parallel state

Figure 5.6(a) shows the resistance versus the applied current at 120 K while the in-plain magnetic field is kept at 210 Oe (the gray arrow in figure 5.1). As mentioned before, in the positive current the electron flow is from fixed layer to free layer and the spin-transfer torque stabilizes the parallel state. In this magnetic field (210 Oe) the sample is already in the parallel state, therefore, no switching is observed in the positive current. When

the current decreases to the negative values, the spin-transfer torque tends to reverse the magnetic configuration of the free layer and the current switching from P to AP is seen at I_c = -6.5 mA. The pillar stays at the antiparallel state at higher values of the current. When the amplitude of the current decreases, the effect of the external magnetic field on the magnetization of the free layer becomes stronger than the spin-transfer torque and then the system relaxes back to the parallel state. This current switching to a lower resistance can be seen at I_c = -1.3 mA. Consequently, at this magnetic field, the parallel state is a stable magnetic configuration. The $\triangle$R is small ($\triangle$R = 0.12 Ω) which means the spin torque does not have enough strength to fully reverse the magnetization of the free layer. Also, two current switchings with negative signs show that at this value of the magnetic field, the parallel state is stable.

Figure 5.6(b) shows the resistance of the pillar versus the bias current at 400 Oe. The sample is in the stable parallel state at this magnetic field and no current switching is observed. An asymmetric with applied current is observed in this figure in which the resistance of the pillar increases by 1.4 ٪ on the positive current and for the negative current by 1.8 ٪. The reason is the different compositions of the top (Au/Ti/Py/Cu) and bottom (Cu/NiMnSb) electrodes which is known as the Peltier effect. When a voltage is applied on the junction between two metals, it induces a temperature gradient between the two leads. The sign of the temperature gradient depends on the sign of the voltage [Deac 06]. In this sample, for a positive voltage, the hot electrode is the NiMnSb lead and for negative voltage the hot electrode is Au/Ti/Py. The measured resistance variation is due to the combination of the Joule heating ($\sim I^2$) and the Peltier heating/cooling ($\sim$ I). For positive current the Peltier cooling and the Joule heating tend to increase the resistance of the pillar by 1.4 ٪ and for the negative current the Peltier heating and the Joule heating increase the resistance by 1.8 ٪ . Therefore the resistance versus the bias current is not symmetric in figure 5.6(b). Note, because of the three terminal measurement, more heat is generated over the device.

5.4 Stable antiparallel state

Figure 5.7 shows the dc resistance of the pillar versus the applied current while the magnetic field is kept at -60 Oe. As shown by the yellow arrow in figure 5.1, the sample is in the antiparallel state in this magnetic field. For the positive current, the device switches to a lower resistance at $I_{AP\rightarrow P}$ = 5.01 mA. The pillar switches to the antiparallel state as soon as the current decreases to $I_{P\rightarrow AP}$ = 3.01 mA. Two positive critical currents ($I_{AP\rightarrow P}$ and $I_{P\rightarrow AP}$) shows that the antiparallel state is stable in this magnetic field.

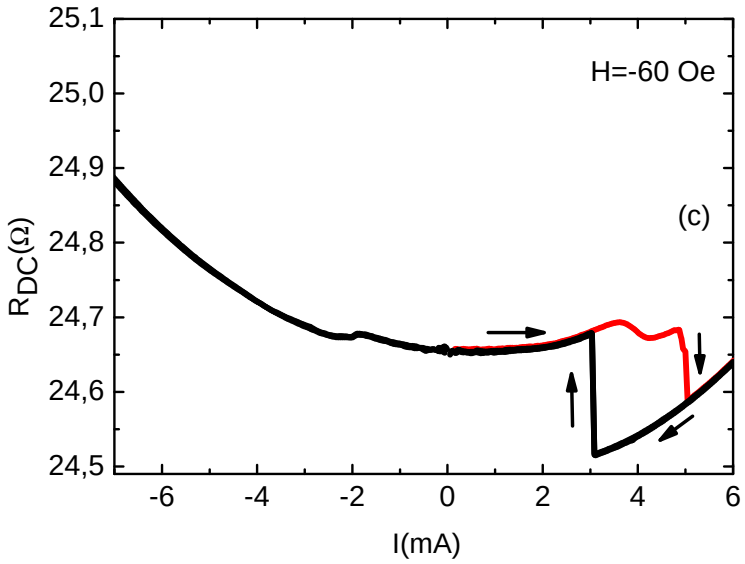

Figure 5.7: The resistance of the pillar versus the applied bias current while the magnetic field is kept at -60 Oe. Both critical currents are in the positive value of the current because the sample is in the antiparallel state. The data points around I = 0 mA are deleted.

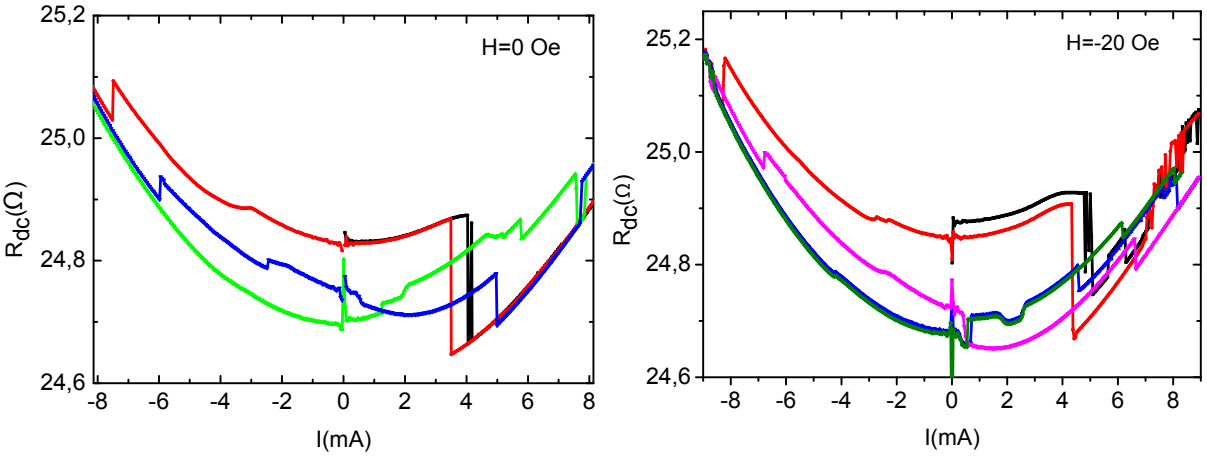

(a) (b)

Figure 5.8: The resistance of the pillar versus the bias current at different external in-plane magnetic fields while they are applied along the long axis of the pillar at 120 K. (a) 0 Oe. (b) -20 Oe.

5.5 Unstable antiparallel and parallel states

Figure 5.8 shows the MR curves of the pillar at 0 Oe (figure 5.8(a)) and -20 Oe (figure 5.8(b)) in which the sample is in the antiparallel state (figure 5.1). The behavior of the sample is unusual and a strong telegraph noise is observed mostly in the range of positive current where the sample is expected to be in the P state. It is probably because the spin torque induces magnetic precession in the free layer [Deac 06] [Fino 06]. In addition to that, the relative effect of the Oersted field is higher in the low magnetic fields and it generates a non-uniform magnetization which increase the noise [Stil 96]. In this magnetic field the spin torque induces random telegraph noises [Pufa 04a]. The system approaches a dynamical regime in which the switching rate approaches the intrinsic damping rate of M, and the dynamics of M have both processional and thermal characteristics. Furthermore, the fluctuation amplitude no longer corresponds to 180 degree reversal of the magnetization. The spin torque induces an unstable configuration of the magnetization.

5.6 Diagram of the critical current and the critical current density

The diagram of the critical current and the critical current density of AP $\rightarrow$ P and P $\rightarrow$ AP states versus an external in-plane magnetic field is shown in figure 5.9. We divide this diagram to four regimes. The antiparallel state is the stable configuration when the magnetic field is less than -50 Oe. In this state both critical currents are positive. The sample does not show any clear switching from -50 Oe to 20 Oe which suggest that there is not any stable state in this interval. It may be because the spin torque induces random telegraph switching [Pufa 04a]. Between 20 Oe and 150 Oe the sample has two stable states (AP and P). In this regime positive $I_{AP\rightarrow P}$ gradually decreases with increasing magnetic field, and negative $I_{P\rightarrow AP}$ decreases linearly. The P state is stable in magnetic field above 150 Oe. In this regime, $I_{AP\rightarrow P}$ changes abruptly to the negative values while the $I_{P\rightarrow AP}$ stays almost constant.

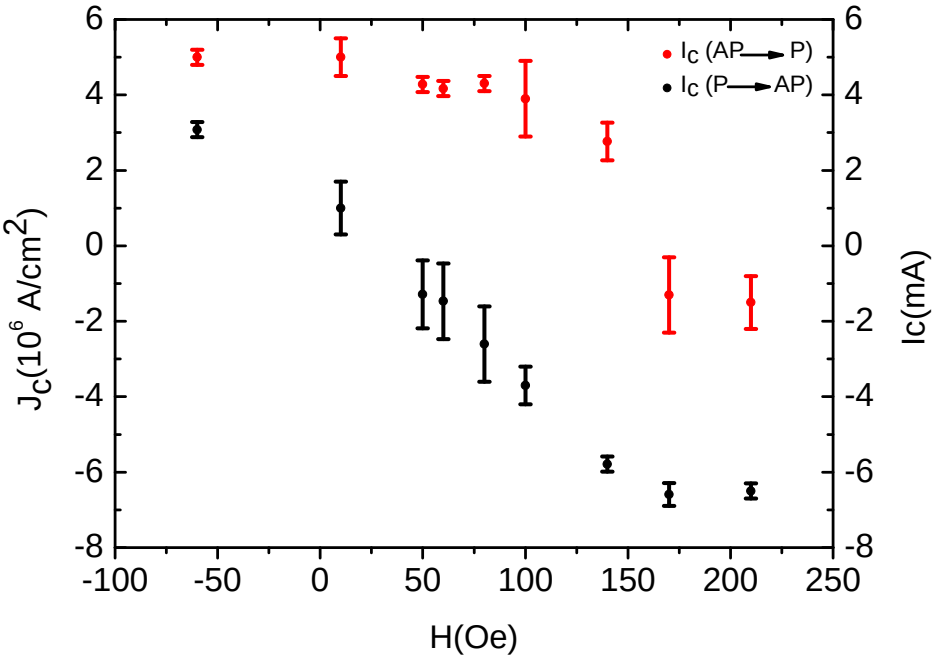

Figure 5.9: The critical current (I_c) and the critical current density (J_c) from AP→P state and P→AP state versus different in-plane magnetic field at 120 K.

Chapter 6

Conclusion and outlook

The research presented in this thesis is focused on the fabrication and characterization of spintronics devices. The characterization is mainly focused on measuring giant magnetoresistance and spin-transfer torque induced magnetic switching. In the fabrication part the main focus is to invent and develop a new method of pillar fabrication which is reproducible and controllable. First, we started to fabricate our samples by following the previous fabrication method used in our group (using a resist mask). The devices which were fabricated with the negative resist mask gave quite a low yield of working samples, and very often the resistance of the pillar was either very high or much too low. The low yield of these samples can be attributed to the formation of standing wall (side walls) after lift-off of resist mask and generation of pin-holes during the ultrasonic agitation. So it becomes inevitable that we should develop a new fabrication process which can solve the mentioned problems.

In the new fabrication process we use PMMA cross linking under high dose of electron irradiation, to protect the pillar from side walls. Also, to make the process as reliable as possible we used metal mask for ion beam etching (IBE) of the pillar. This new method is used for fabrication of our final samples which contain two ferromagnetic layers (Py and NiMnSb) separated by a Cu layer.

We measure the CPP-GMR properties of our trilayer pillar by applying a constant dc bias current and sweeping an external in-plane magnetic field. In three terminal measurements, the raw data shows the difference in resistance $\triangle$R of 0.17 Ω (0.5 %) and $\sim$ 0.37 Ω (1.87 %) at room temperature and 4.2 K, respectively. Moreover, we examined the magnetoresistance of the pillar as a function of the in-plane magnetic field at different angles. A large difference in shape of the MR curves for two different angles of $\Phi = 0^{\circ}$ and $\Phi = 90^{\circ}$ is observed.

In addition to CPP-GMR, we studied the spin-transfer torque induced magnetic reversal by current. The critical current densities which we measured are the order of 10^6 A/cm^2 which is one order of magnitude smaller than current industry standards. Also, our measurements shows that the stability of the magnetic state in the pillar is connected to the applied magnetic field. Finally, we have found that the sample has four different

configurations (P stable, AP stable, both A and AP stable and both A and AP unstable) which are depended to value of applied magnetic field.

While our fabrication processes has high yield of working samples, there is still room for optimizing the fabrication process. Also, improving the uniformity and homogeneity of the layer stack and producing smoother interfaces are very important to increase the output of future devices.

Other attractive projects for future researchers could be replacing the Cu layer by a tunnel barrier in the layer stack. Tunnel magneto resistance devices are used in MRAM industry and have the intense interest at the moment.

Appendix A

Fabrication of the pillar using a resist mask

1. Resist mask pillar:

- **Resist deposition**
  - AR4060 → [5000 rpm, 40″], [baking 90℃, 15 min]
- **Electron beam exposure**
  - Exposure dose → 3600μC/cm^2 (at 30 kv)
- **Baking**
  - baking → 105℃, 10 min.
- **Post UV exposure**
  - UV exposure → 20 seconds.
- **Development**
  - AR300.26(1:4 water) for 2 min, rinsing water (2 min)
- **Dry etching**
  - Ar^+ 80″ (CAIBE, angle 70, 400V)
- **SiN deposition**
  - Immediately deposition of SiN by PECVD after etching (50 nm)
- **Removing the resist column on pillar**
  - NEP at 80℃ with ultrasonic agitation

3. **Bottom contacts:**

- **Resist deposition**
  - 950K, 5%→ [550 rpm, 40″], [baking 200℃, 1 min]
  - 950K, 5%→ [5500 rpm, 40″], [baking 200℃, 30 min]
- **Electron beam exposure and development**
  - Exposure dose → 750μC/cm^2 (at 30 kv)
  - AR600.56:IPA (1:1) for 1 min
- **RIE to etch SiN (opening bottom contacts)**
  - Flash miniclean
  - { CHF_3 40″ → O_2 plasma 40″ (miniclean) }
  - Ar^+ 6″ (CAIBE, angle 70, 400V) to refresh the surface of Heusler
- **Metal deposition**
  - Ti(2nm)/Au(30nm)

6. **Central part of the Au contacts:**

- **Resist deposition**
  - 600K, 4%→ [5000 rpm, 40″], [baking 200℃, 1 hour]
  - 950K, 3%→ [7500 rpm, 40″], [baking 180℃, 1 hour]
- **Electron beam exposure**
  - Exposure dose → 650μC/cm^2 (field to 81.92 μm)
- **Development**
  - AR600.56:IPA (1:1) for 1 min
- **Metal deposition**
  - Ti(3nm)/Au(70nm)
  - Lift-off, Miniclean for 1 min

7. **Big optical contacts:**

- **Resist deposition**

- AR4040 → [6000 rpm, 40″], [baking 92℃, 2 min]

- **Mask aligner**
  - Exposure for 12 seconds

- **Development**
  - AR300.26:IPA (1:4 water) for 30 seconds

- **Metal deposition**
  - Ti(2nm)/Au(120nm)
  - Lift-off in acetone

8. Bonding

Appendix B

Fabrication of the pillar using a metal mask (new method)

1. Metallic pillars:

- **Resist deposition**
  - 600K, 4٪→ [5000 rpm, 40″], [baking 200℃, 1 hour]
  - 950K, 3٪→ [7500 rpm, 40″], [baking 180℃, 1 hour]
- **Electron beam exposure**
  - Exposure dose → 1500-1800μC/cm^2 (at 30 kv)
- **Development**
  - AR600.56:IPA (1:1) for 1 min
  - US (frequency 80 : Power 50) for 3 sec at 45th sec, Rinse in IPA.
  - Miniclean FLASH
- **Metal deposition**
  - Ti(5nm)/Au(95nm)/Ti(12 nm)
  - Lift-off, Miniclean for 1 min.
- **Dry etching**
  - Ar^+ 85″ (CAIBE, angle 70, 400V)

2. First cross-linking:

- **Resist deposition**

- 600K, 4%→ [5000 rpm, 40″ (accelerating value 9)], [baking 180℃, 30 min]

- **Electron beam exposure**
  - Exposure dose → 250 loops ×100 μC/cm^2 [Step = 8 pixels,area settling time 1 sec]

- **Development**
  - 10 min in 50℃acetone → 1-2 min ultrasonic agitation (80/40). Rinse in IPA

- **SiN deposition**
  - Ar^+ 6″ (CAIBE, angle 70, 400V) to refresh the surface of Heusler to be conducting
  - Immediately deposition of SiN PECVD (50 nm)

3. Bottom contacts:

- **Resist deposition**
  - 950K, 5%→ [550 rpm, 40″], [baking 200℃, 1 min]
  - 950K, 5%→ [5500 rpm, 40″], [baking 200℃, 30 min]

- **Electron beam exposure and development**
  - Exposure dose → 750μC/cm^2 (at 30 kv)
  - AR600.56:IPA (1:1) for 1 min

- **RIE to etch SiN (opening bottom contacts)**
  - Flash miniclean
  - 2 cycles { CHF_3 50″ → O_2 plasma 30″ (miniclean) }
  - Ar^+ 6″ (CAIBE, angle 70, 400V) to refresh the surface of Heusler

- **Metal deposition**
  - Ti(2nm)/Au(30nm)

4. Opening top of the pillar:

- **Resist deposition**
  - 950K, 5%→ [550 rpm, 40″], [baking 200℃, 1 min]
  - 950K, 5%→ [5500 rpm, 40″], [baking 200℃, 30 min]

- **RIE to etch SiN and cross-linked PMMA (opening top contacts)**
  - Flash miniclean
  - 3 cycles { CHF_3 35″ → O_2 plasma 30″ (miniclean) }
  - Rest of PMMA removal → acetone 10 min, Rinse in IPA.
  - RIE 10 minutes O_2 plasma (remove the open cross-linked PMMA)

5. **Second cross-linking:**

- **Resist deposition and electron beam exposure are as same as the first cross-linking**

- **Etching cross-linked PMMA to open top of the pillar**
  - O_2 plasma 15″ - 30″ (Control in SEM)

6. **Central part of the Au contacts:**

- **Resist deposition**
  - 600K, 7%→ [5000 rpm, 40″], [baking 200℃, 30 min]
  - 950K, 3%→ [7500 rpm, 40″], [baking 180℃, 30 min]

- **Electron beam exposure**
  - Exposure dose → 600μC/cm^2 (field to 163.84 μm)

- **Development**
  - AR600.56:IPA (1:1) for 1 min

- **Metal deposition**
  - Ti(3nm)/Au(70nm)
  - Lift-off, Miniclean for 1 min

7. **Big Au contacts:**

- **Resist deposition**
  - 600K, 7%→ [5000 rpm, 40″], [baking 200℃, 30 min]
  - 950K, 3%→ [6500 rpm, 40″], [baking 180℃, 30 min]

- **Electron beam exposure**

- Exposure dose → 675μC/cm^2, Aperture 120μm

- **Development**
  - AR600.56:IPA (1:1) for 1 min

- **Metal deposition**
  - Ti(5nm)/Au(100nm)
  - Lift-off, Miniclean for 1 min

8. Bonding

Appendix C

Picture Gallery

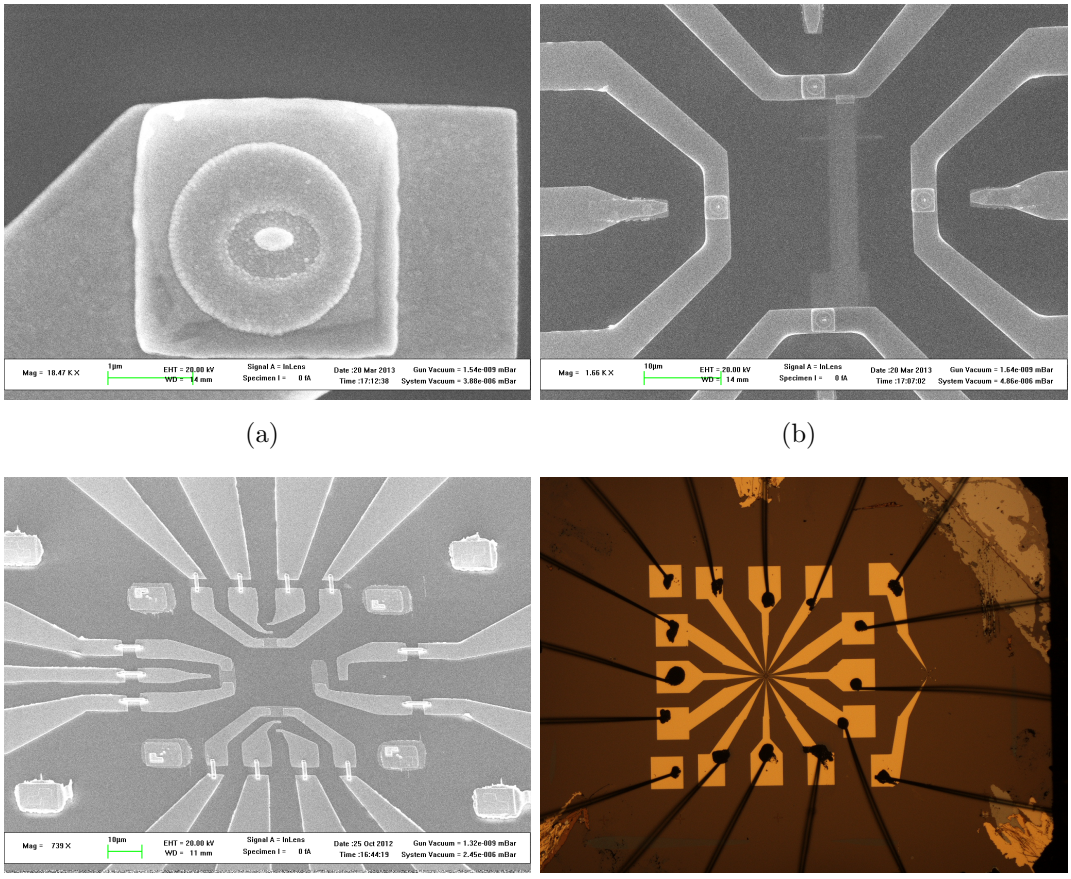

(a) (b)

(c) (d)

Figure C.1: Top views of final samples. (a) A pillar. (b) Small contacts lead. (c) SEM image of a sample in which small contact leads and big contact leads are connected by gold bridge. (d) A glue-bonded sample, in this bonding wires are are stuck to the big contact pads by conductive glue.

Bibliography

[Acre 06] Y. Acremann, J. P. Strachan, V. Chembrolu, S. D. Andrews, T. Tyliszczak, J. A. Katine, M. J. Carey, B. M. Clemens, H. C. Siegmann, and J. Stöhr. *Phys. Rev. Lett.*, Vol. 96, p. 217202, 2006.

[Apal 13] D. Apalkov, A. Khvalkovskiy, S. Watts, V. Nikitin, X. Tang, D. Lottis, K. Moon, X. Luo, E. Chen, A. Ong, A. Driskill-Smith, and M. Krounbi. *J. Emerg. Technol. Comput. Syst.*, Vol. 9, No. 2, pp. 1–35, 2013.

[Arel 08] A. D. Arelaro. *Sintese e caracterizacao de nanoparticulas Magnetica de ferritas*. PhD thesis, Universidade de Sao Paulo Instituto de Fisica, 2008.

[Bach 03] P. Bach, A. S. Bader, C. Ruster, C. Gould, C. R. Becker, G. Schmidt, L. W. Molenkamp, W. Weigand, C. Kumpf, E. Umbach, R. Urban, G. Woltersdorf, and B. Heinrich. *Appl. Phys. Lett.*, Vol. 83, No. 3, pp. 521–523, 2003.

[Baib 88] M. N. Baibich, J. M. Broto, A. Fert, F. N. Van Dau, F. Petroff, P. Etienne, G. Creuzet, A. Friederich, and J. Chazelas. *Phys. Rev. Lett.*, Vol. 61, pp. 2472–2475, 1988.

[Bass 99] J. Bass and W. Pratt Jr. *Journal of Magnetism and Magnetic Materials*, Vol. 200, No. 13, pp. 274–289, 1999.

[Berg 96] L. Berger. *Phys. Rev. B*, Vol. 54, No. 13, pp. 9353–9358, 1996.

[Bina 89] G. Binasch, P. Grnberg, F. Saurenbach, and W. Zinn. *Phys. Rev. B*, Vol. 39, No. 7, pp. 4828–4830, 1989.

[Blum 09] C. G. F. Blum, C. A. Jenkins, J. Barth, C. Felser, S. Wurmehl, G. Friemel, C. Hess, G. Behr, B. Bchner, A. Reller, S. Riegg, S. G. Ebbinghaus, T. Ellis, P. J. Jacobs, J. T. Kohlhepp, and H. J. M. Swagten. *Applied Physics Letters*, Vol. 95, No. 16, p. 161903, 2009.

[Borc 01] C. N. Borca, T. Komesu, H.-K. Jeong, P. A. Dowben, D. Ristoiu, C. Hordequin, J. P. Nozires, J. Pierre, S. Stadler, and Y. U. Idzerda. *Phys. Rev. B*, Vol. 64, No. 5, p. 052409, 2001.

[Brag 05] P. M. Braganca, I. N. Krivorotov, O. Ozatay, A. G. F. Garcia, N. C. Emley, J. C. Sankey, D. C. Ralph, and R. A. Buhrman. *Applied Physics Letters*, Vol. 87, No. 11, p. 112507, 2005.

[Brat 06] A. Brataas, G. E. Bauer, and P. J. Kelly. *Physics Reports*, Vol. 427, No. 4, pp. 157–255, 2006.

[Brat 12] A. Brataas, A. D. Kent, and H. Ohno. *Nat Mater*, Vol. 11, No. 5, pp. 372–381, 2012.

[Burk 01] K. O. Burkard Hillebrands. *Spin Dynamics in Confined Magnetic Structures I.* Springer, 06.11.2001.

[Chal 04] A. Chalastaras. *Giant Magnetoresistance in Magnetic Multilayers Using a New Embossed Surface.* Master's thesis, University of New Orleans, 2004.

[Chap 07] C. Chappert, A. Fert, and F. N. Van Dau. *Nat Mater*, Vol. 6, No. 11, pp. 813–823, 2007.

[Chen 12] W. Chen. *Characterization of spin transfer torque and magnetization manipulation in magnetic nanistructures.* PhD thesis, Cornell University, 2012.

[Covi 04] M. Covington, M. AlHajDarwish, Y. Ding, N. J. Gokemeijer, and M. A. Seigler. *Phys. Rev. B*, Vol. 69, No. 18, p. 184406, 2004.

[Cui 12] Y. Cui. *Characterization of magnetic dynamics excited by spin transfer torque in anomagnet.* PhD thesis, Cornell University, 2012.

[Deac 06] A. Deac, K. J. Lee, Y. Liu, O. Redon, M. Li, P. Wang, J. P. Nozires, and B. Dieny. *Phys. Rev. B*, Vol. 73, No. 6, p. 064414, 2006.

[Deac 08] A. M. Deac, A. Fukushima, H. Kubota, H. Maehara, Y. Suzuki, S. Yuasa, Y. Nagamine, K. Tsunekawa, D. D. Djayaprawira, and N. Watanabe. *Nat Phys*, Vol. 4, No. 10, pp. 803–809, 2008.

[Deng 13] R.-G. Dengel. *Fabrication of magnetic artification atoms.* PhD thesis, Experimental physics 3, Department of Physics, University of Wuerzburg, 2013.

[Dien 91] B. Dieny, V. S. Speriosu, S. S. P. Parkin, B. A. Gurney, D. R. Wilhoit, and D. Mauri. *Phys. Rev. B*, Vol. 43, No. 1, pp. 1297–1300, 1991.

[Eid 03] K. Eid, J. W. P. Pratt, and J. Bass. *Journal of Applied Physics*, Vol. 93, No. 6, pp. 3445–3449, 2003.

[Fert 02] A. Fert, J.-M. George, H. Jaffres, and G. Faini. *Journal of Physics D: Applied Physics*, Vol. 35, No. 19, p. 2443, 2002.

[Fert 69] A. Fert. *Journal of Physics C: Solid State Physics*, Vol. 2, No. 10, p. 1784, 1969.

[Fino 06] G. Finocchio, M. Carpentieri, B. Azzerboni, L. Torres, E. Martinez, and L. Lopez-Diaz. *Journal of Applied Physics*, Vol. 99, No. 8, pp. 08G522–08G522–3, 2006.

[Fuji 95] T. Fujimoto, M. Patel, E. Gu, C. Daboo, and J. Bland. *Journal of Magnetism and Magnetic Materials*, Vol. 148, No. 12, pp. 323–324, 1995.

[Gilb 04] T. Gilbert. *Magnetics, IEEE Transactions on*, Vol. 40, No. 6, pp. 3443–3449, 2004.

[Gloe 75] P. G. Gloersen. *Journal of Vacuum Science and Technology*, Vol. 12, No. 1, pp. 28–35, 1975.

[Groo 83] R. A. de Groot, F. M. Mueller, P. G. v. Engen, and K. H. J. Buschow. *Phys. Rev. Lett.*, Vol. 50, No. 25, pp. 2024–2027, 1983.

[Hase 93] H. Hasegawa. *Phys. Rev. B*, Vol. 47, No. 22, pp. 15080–15085, 1993.

[Hatz 69] M. Hatzakis. *Journal of Electrochemical Society*, Vol. 116, p. 1033, 1969.

[Heid 01] C. Heide, P. E. Zilberman, and R. J. Elliott. *Phys. Rev. B*, Vol. 63, p. 064424, 2001.

[Hous 07] D. Houssameddine, U. Ebels, B. Delaet, B. Rodmacq, I. Firastrau, F. Ponthenier, M. Brunet, C. Thirion, J.-P. Michel, L. Prejbeanu-Buda, M.-C. Cyrille, O. Redon, and B. Dieny. *Nat Mater*, Vol. 6, No. 6, pp. 447–453, 2007.

[Hous 08] D. Houssameddine, S. Florez, J. Katine, J.-P. Michel, U. Ebels, D. Mauri, O. Ozatay, B. Delaet, B. Viala, L. Folks, B. Terris, and M.-C. Cyrille. *Applied Physics Letters*, Vol. 93, No. 2, p. 022505, 2008.

[IACa 82] A. F. I.A.Campbell. *Ferromagnetic Materials:chapter9*. North-Holland, Amsterdam, 1982.

[Jans 96] H. Jansen, H. Gardeniers, M. de Boer, M. Elwenspoek, and J. Fluitman. *Journal of Micromechanics and Microengineering*, Vol. 6, No. 1, p. 1428, 1996.

[Jede 01] F. J. Jedema, A. T. Filip, and B. J. van Wees. *Nature*, Vol. 410, No. 6826, pp. 345–348, 2001.

[John 13] R. L. John Gantz, David Reinsel. *IDC analyze the future*, pp. 1–7, 2013.

[Kaka 05] S. Kaka, M. R. Pufall, W. H. Rippard, T. J. Silva, S. E. Russek, and J. A. Katine. *Nature*, Vol. 437, No. 7057, pp. 389–392, 2005.

[Kati 00] J. A. Katine, F. J. Albert, R. A. Buhrman, E. B. Myers, and D. C. Ralph. *Phys. Rev. Lett.*, Vol. 84, No. 14, pp. 3149–3152, 2000.

[Kati 08] J. Katine and E. E. Fullerton. *Journal of Magnetism and Magnetic Materials*, Vol. 320, No. 7, pp. 1217–1226, 2008.

[Kent 04] A. D. Kent, B. zyilmaz, and E. del Barco. *Applied Physics Letters*, Vol. 84, No. 19, pp. 3897–3899, 2004.

[Kise 03] S. I. Kiselev, J. C. Sankey, I. N. Krivorotov, N. C. Emley, R. J. Schoelkopf, R. A. Buhrman, and D. C. Ralph. *Nature*, Vol. 425, No. 6956, pp. 380–383, 2003.

[Koba 09] K. Kobayashi, N. Inaba, N. Fujita, Y. Sudo, T. Tanaka, M. Ohtake, M. Futamoto, and F. Kirino. *Magnetics, IEEE Transactions on*, Vol. 45, No. 6, pp. 2541–2544, 2009.

[Koom 08] J. G. Koomey. *Environmental Research Letters*, Vol. 3, No. 3, p. 034008, 2008.

[Kriv 04] I. N. Krivorotov, N. C. Emley, A. G. F. Garcia, J. C. Sankey, S. I. Kiselev, D. C. Ralph, and R. A. Buhrman. *Phys. Rev. Lett.*, Vol. 93, No. 16, p. 166603, 2004.

[Kriv 05] I. N. Krivorotov, N. C. Emley, J. C. Sankey, S. I. Kiselev, D. C. Ralph, and R. A. Buhrman. *Science*, Vol. 307, No. 5707, pp. 228–231, 2005.

[Kriv 08] I. N. Krivorotov, N. C. Emley, R. A. Buhrman, and D. C. Ralph. *Phys. Rev. B*, Vol. 77, No. 5, p. 054440, 2008.

[Laks 11] M. Lakshmanan. *Phil. Trans. R. Soc. A.*, Vol. 369, p. 1939, 2011.

[Lee 04] K.-J. Lee, A. Deac, O. Redon, J.-P. Nozieres, and B. Dieny. *Nat Mater*, Vol. 3, No. 12, pp. 877–881, 2004.

[Lee 09] O. J. Lee, V. S. Pribiag, P. M. Braganca, P. G. Gowtham, D. C. Ralph, and R. A. Buhrman. *Applied Physics Letters*, Vol. 95, No. 1, p. 012506, 2009.

[Leem 10] L. Leem. *Magnetiic coupled spin-torque device: spin-based non-volatile logic device and applications.* PhD thesis, Stanford university, 2010.

[Liu 09] L. Liu, T. Moriyama, D. C. Ralph, and R. A. Buhrman. *Applied Physics Letters*, Vol. 94, No. 12, p. 122508, 2009.

[Loch 12] F. Lochner. *Epitaxial growth and characterization of NiMnSb layers for novel spintronic devices.* PhD thesis, Department of Physics, University of Wuerzburg, 2012.

[Manc 05] F. B. Mancoff, N. D. Rizzo, B. N. Engel, and S. Tehrani. *Nature*, Vol. 437, No. 7057, pp. 393–395, 2005.

[Mang 06] S. Mangin, D. Ravelosona, J. A. Katine, M. J. Carey, B. D. Terris, and E. E. Fullerton. *Nat Mater*, Vol. 5, No. 3, pp. 210–215, 2006.

[Megu 08] K. Meguro, H. Hoshiya, and K. Nakamoto. *Journal-magnetics society of Japan*, Vol. 32, No. 3, p. 234, 2008.

[Mood 95] J. S. Moodera, L. R. Kinder, T. M. Wong, and R. Meservey. *Phys. Rev. Lett.*, Vol. 74, No. 16, pp. 3273–3276, 1995.

[Myer 02] E. B. Myers, F. J. Albert, J. C. Sankey, E. Bonet, R. A. Buhrman, and D. C. Ralph. *Phys. Rev. Lett.*, Vol. 89, No. 19, p. 196801, 2002.

[Myer 99] E. B. Myers, D. C. Ralph, J. A. Katine, R. N. Louie, and R. A. Buhrman. *Science*, Vol. 285, No. 5429, pp. 867–870, 1999.

[Naka 12] T. Nakatani, N. Hase, H. Goripati, Y. Takahashi, T. Furubayashi, and K. Hono. *Magnetics, IEEE Transactions on*, Vol. 48, No. 5, pp. 1751–1757, 2012.

[Nala 02] H. singh Nalawa. *Handbook of thin film materials*. Academic press, 2002.

[Park 91] S. S. P. Parkin, Z. G. Li, and D. J. Smith. *Applied Physics Letters*, Vol. 58, No. 23, pp. 2710–2712, 1991.

[Pate 11] R. Patel and A. Majumdar. *Journal of Magnetism and Magnetic Materials*, Vol. 323, No. 5, pp. 646–649, 2011.

[Pavl 95] J. Pavlinec and M. Lazar. *Journal of Applied Polymer Science*, Vol. 55, No. 1, pp. 39–45, 1995.

[Peng 09] X. Peng, S. Wakeham, A. Morrone, S. Axdal, M. Feldbaum, J. Hwu, T. Boonstra, Y. Chen, and J. Ding. *Vacuum*, Vol. 83, No. 6, pp. 1007 – 1013, 2009.

[Peti 07] S. Petit, C. Baraduc, C. Thirion, U. Ebels, Y. Liu, M. Li, P. Wang, and B. Dieny. *Phys. Rev. Lett.*, Vol. 98, No. 7, p. 077203, 2007.

[Prof 02] P. D. K. I. Professor Dr. Eiichi Hirota, Professor Dr. Hirosi Sakakima. *Giant Magnetoresistance Devices*. Springer, 2002.

[Pufa 04a] M. R. Pufall, W. H. Rippard, S. Kaka, S. E. Russek, T. J. Silva, J. Katine, and M. Carey. *Phys. Rev. B*, Vol. 69, No. 21, p. 214409, 2004.

[Pufa 04b] M. R. Pufall, W. H. Rippard, S. Kaka, S. E. Russek, T. J. Silva, J. Katine, and M. Carey. *Phys. Rev. B*, Vol. 69, No. 21, p. 214409, 2004.

[Ralp 08] D. Ralph and M. Stiles. *Journal of Magnetism and Magnetic Materials*, Vol. 320, No. 7, pp. 1190–1216, 2008.

[Raph 02] M. P. Raphael, B. Ravel, Q. Huang, M. A. Willard, S. F. Cheng, B. N. Das, R. M. Stroud, K. M. Bussmann, J. H. Claassen, and V. G. Harris. *Phys. Rev. B*, Vol. 66, No. 10, p. 104429, 2002.

[Rieg 11] A. Riegler. *Ferromagnetic resonance study of the Half-Heusler alloy NiMnSb:The benefit of using NiMnSb as a ferromagnetic layer in pseudo-spin-valve based spin-torque oscillators*. PhD thesis, Experimental physics 3, Department of Physics, University of Wuerzburg, 2011.

[Ripp 04] W. H. Rippard, M. R. Pufall, S. Kaka, S. E. Russek, and T. J. Silva. *Phys. Rev. Lett.*, Vol. 92, No. 2, p. 027201, 2004.

[Ritc 03] L. Ritchie, G. Xiao, Y. Ji, T. Y. Chen, C. L. Chien, M. Zhang, J. Chen, Z. Liu, G. Wu, and X. X. Zhang. *Phys. Rev. B*, Vol. 68, No. 10, p. 104430, 2003.

[Rose 08] A. K. F. Rosei. *Nanoelectronics and Photonics: From Atoms to Materials, Devices, and Architectures (Google eBook)*. Springer, September 23, 2008.

[Sami 14] M. Samiepour, F. Gerhard, T. Borzenko, C. Gould, and L. Molenkamp. *Microelectronic Engineering*, Vol. 119, No. 0, pp. 20–23, 2014.

[Satt 10] K. D. Sattler. *Handbook of Nanophysics: Nanoparticles and Quantum Dots*. CRC Press, 2010.

[Sche 95] K. M. Schep, P. J. Kelly, and G. E. W. Bauer. *Phys. Rev. Lett.*, Vol. 74, No. 4, pp. 586–589, 1995.

[Slon 02] J. Slonczewski. *Journal of Magnetism and Magnetic Materials*, Vol. 247, No. 3, pp. 324–338, 2002.

[Slon 88] J. Slonczewski, B. Petek, and B. Argyle. *Magnetics, IEEE Transactions on*, Vol. 24, No. 3, pp. 2045–2054, 1988.

[Slon 96] J. Slonczewski. *Journal of Magnetism and Magnetic Materials*, Vol. 159, No. 12, pp. L1–L7, 1996.

[Some 76] S. Somekh. *Journal of Vacuum Science and Technology*, Vol. 13, No. 5, pp. 1003–1007, 1976.

[Soul 98] R. J. Soulen, J. M. Byers, M. S. Osofsky, B. Nadgorny, T. Ambrose, S. F. Cheng, P. R. Broussard, C. T. Tanaka, J. Nowak, J. S. Moodera, A. Barry, and J. M. D. Coey. *Science*, Vol. 282, No. 5386, pp. 85–88, 1998.

[Stil 06] M. D. Stiles and J. Miltat. *Springer Berlin / Heidelberg, Heidelberg, DE*, No. 21, pp. 225 – 308, November 01, 2006.

[Stil 96] M. D. Stiles. *Journal of Applied Physics*, Vol. 79, No. 8, pp. 5805–5810, 1996.

[Tehr 03] S. Tehrani, J. M. Slaughter, M. DeHerrera, B. Engel, N. Rizzo, J. Salter, M. Durlam, R. Dave, J. Janesky, B. Butcher, K. Smith, and G. Grynkewich. *Proceedings of the IEEE*, Vol. 91, No. 5, pp. 703–714, 2003.

[Tomo 11] N. Tomoya. *Spin-dependent scattering inCPP-GMR using Heusler alloy and the selection of the spacer material*. PhD thesis, University of Tsukuba, 2011.

[Tsan 94] C. Tsang, R. Fontana, T. Lin, D. Heim, V. S. Speriosu, B. Gurney, and M. Williams. *Magnetics, IEEE Transactions on*, Vol. 30, No. 6, pp. 3801–3806, 1994.

[Tsoi 98] M. Tsoi, A. G. M. Jansen, J. Bass, W.-C. Chiang, M. Seck, V. Tsoi, and P. Wyder. *Phys. Rev. Lett.*, Vol. 80, No. 19, pp. 4281–4284, 1998.

[Vale 93] T. Valet and A. Fert. *Phys. Rev. B*, Vol. 48, No. 10, pp. 7099–7113, 1993.

[Wain 00] X. Waintal, E. B. Myers, P. W. Brouwer, and D. C. Ralph. *Phys. Rev. B*, Vol. 62, No. 18, pp. 12317–12327, 2000.

[Wolf 01] S. A. Wolf, D. D. Awschalom, R. A. Buhrman, J. M. Daughton, S. von Molnr, M. L. Roukes, A. Y. Chtchelkanova, and D. M. Treger. *Science*, Vol. 294, No. 5546, pp. 1488–1495, 2001.

[Yaku 06] K. Yakushiji, K. Saito, S. Mitani, K. Takanashi, Y. K. Takahashi, and K. Hono. *Applied Physics Letters*, Vol. 88, No. 22, pp. 222504–222507, 2006.

[Zahn 95] P. Zahn, I. Mertig, M. Richter, and H. Eschrig. *Phys. Rev. Lett.*, Vol. 75, No. 16, pp. 2996–2999, 1995.

[Zail 96] I. Zailer, J. E. F. Frost, V. Chabasseur-Molyneux, C. J. B. Ford, and M. Pepper. *Semiconductor Science and Technology*, Vol. 11, No. 8, p. 1235, 1996.

[Zhan 02] S. Zhang, P. M. Levy, and A. Fert. *Phys. Rev. Lett.*, Vol. 88, No. 23, p. 236601, 2002.

[Zhi 14] W. L. H. Z. X.-H. X. Zhi-Yong Quan, Li Zhang. *Nanoscale Research Letters*, Vol. 9, p. 6, 2014.

[ZHOU 09] Y. ZHOU. *Spin momentum transfer effects for spintronic device applications*. PhD thesis, Stockholm-Kista, Sweden, 2009.

[Zhu 03] J.-G. J. Zhu. *Materials Today*, Vol. 6, No. 78, pp. 22–31, 2003.

[Zhu 04] J.-G. Zhu, N. Kim, Y. Zhou, Y. Zheng, J. Chang, K. Ju, X. Zhu, and R. M. White. *Magnetics, IEEE Transactions on*, Vol. 40, No. 4, pp. 2323–2325, 2004.

Acknowledgements

The researches described in this dissertation would not be possible without the enormous amount of help from many people. I would like to take this opportunity to thank all of them!!!

- First of all I would like to express my thankfulness to Prof. Laurens W. Molenkamp the head of the EP3 chair and the spintronics group for giving me the opportunity to work in his group.

  I also want to especially thank the following groups of people:

- PD Dr. Charles Gould as my advisor for my PhD with his knowledge, experience and rigorous attitude on research. I also want to thank him for his patience and help in improving my writing and presentation skills.

- Dr. Tanja Borzenko as my supervisor on fabrication of samples. I have been fortune to have this chance to receive tremendous guidance, experience and knowledge from her during these past years. I have learned a great deal about how to work precisely and professionally in clean room. On top of all these she is an extremely nice person, working so hard and demanding so little from others, almost too nice of a boss and nearly spoiled me.

- Shijin Babu Pakayl for being next to me in a strange land with patience, kindness and happiness, and for introducing me to different ways of seeing the world. Also, thanks for the helpful corrections and suggestions for this thesis.

- Philip Hartmann for teaching me glue bonding, working with Gilgamesh and helping me during measurements. And more important for his rich personality.

- The C113 people: Dr. Fanny Greullet, Tsvetelina Naydenova, Kia Tavakkoli, Jennifer Constantino and Thomas Wagner thank you very much for the good memories and the enormous help during experiments and filling the cryostat.

- The C114a people: Dr. Stefan Mark, Philip Hartmann, Dr. Michael Rüth and Gabriel Dengel thank you very much for your kindness and support during experiments. Also for your warm welcome to me in a cold land.

- To Volkmar Hock for his introduction about clean room and optical lithography. Moreover for keeping all of the systems in good order which requires a lot of time and efforts and bringing such a pleasant atmosphere to the clean room.

- Felicitas Gerhard for growing the layer stack and for preparing the layer stack whenever I needed. And to everybody else in EP3.

- I also would like to gratefully acknowledge financial support from European Commissions Fantomas and MaCalo.

- To my advisor Prof Dr. Hamid Reza Moshfegh during my Bachelor studies at Tehran University. He took me to the world of scientific research with impressive vision and always lent me and all his students his strongest support. Also I thank all of my professors and teachers during my education periods.

- To all my university friends and high school friends in Iran. Thank you very much for sharing wonderful memories in Iran. And special thanks to Aida Delfan for encouraging and supporting me to go abroad for doing my PhD and to Ali Masihi for always being there as a "friend in need".

- To all my Iranian friends in Würzburg (Kourosh Yazdani, Nima Adib, Ghazaleh Setare, Maryam Mahdiani, Iman Ahmadi, Yalda Kouhi, Farough Roustaie, Amir Daryani, Iman Kinafar, Rayan Khodayari and ...) for truly making life a joy and for all parties and dances which helped me to release stress of this thesis. Also, sincere gratitude to them all for standing by me such as a real family during my sickness and my difficulties.

- To my parents, Fatemeh and Fazlolah, for believing in me, supporting me and loving me unconditionally. I would not have the opportunity to pursue an academic career and would not have the luxury to focus on my research without the moral support from my parents. I also want to express my deepest gratitude to my lovely sister and my handsome brother, Mitra and Mohammad, who are two of my greatest supporters. I love you.